General Disclaimer

One or more of the Following Statements may affect this Document

- This document has been reproduced from the best copy furnished by the organizational source. It is being released in the interest of making available as much information as possible.

- This document may contain data, which exceeds the sheet parameters. It was furnished in this condition by the organizational source and is the best copy available.

- This document may contain tone-on-tone or color graphs, charts and/or pictures, which have been reproduced in black and white.

- This document is paginated as submitted by the original source.

- Portions of this document are not fully legible due to the historical nature of some of the material. However, it is the best reproduction available from the original submission.

Produced by the NASA Center for Aerospace Information (CASI)

COM-75-11334

NIMBUS-5 SOUNDER DATA PROCESSING SYSTEM. PART II. RESULTS

W. L. Smith, et al

National Environmental Satellite Service

Prepared for:

National Aeronautics and Space Administration

July 1975

DISTRIBUTED BY:

NTIS

National Technical Information Service
U. S. DEPARTMENT OF COMMERCE

75082801 COM-75-11334

NOAA Technical Memorandum NESS 71

NIMBUS-5 SOUNDER DATA PROCESSING SYSTEM

PART II. RESULTS

W. L. Smith
H. M. Woolf
C. M. Hayden
W. C. Shen

Washington, D.C.
July 1975

Reproduced by
NATIONAL TECHNICAL
INFORMATION SERVICE
US Department of Commerce
Springfield, VA. 22151

noaa NATIONAL OCEANIC AND ATMOSPHERIC ADMINISTRATION / National Environmental Satellite Service

NESS Technical Memorandums

National Environmental Satellite Service Series

The National Environmental Satellite Service (NESS) is responsible for the maintenance and operation of the meteorological satellite systems of NOAA.

NESS Technical Memorandums facilitate rapid distribution of material that may be preliminary in nature and/or of a nature usually unknown at a later date. Publications 1 through 10 and 17 through 33 are in the series NOAA National Environmental Satellite Center Technical Memorandum (NESCTM) series. The regular NESS Technical Memorandum (NESS) series includes 34, 36, and subsequent issues.

Publications listed below are available from the National Technical Information Service, U.S. Department of Commerce, Sills Bldg., 5285 Port Royal Road, Springfield, Va. 22151. Prices on request. Order by accession number (shown in parentheses). Information on memorandums not listed below can be obtained from Environmental Data Service (EDS), 1320 Dolphin St., NW, Washington, D.C. 20235.

NESS Technical Memorandums

NESS 18 On Reference Levels for Determining Height Profiles From Satellite-Measured Temperature Profiles. Christopher M. Hayden, December 1972, 15 pp. (COM-72-50353)

NESS 33 Use of Satellite Data in East Coast Snowstorm Forecasting. Francis C. Fernandez, February 1972, 21 pp. (COM-72-10462)

NESS 34 Chromium Dioxide Recording--Its Characteristics and Potential for Telemetry. Florence Nash, March 1972, 10 pp. (COM-72-10644)

NESS 35 Modified Version of the Improved TIROS Operational Satellite (ITOS D-G). A. Schwalb, April 1972, 48 pp. (COM-72-10547)

NESS 36 A Technique for the Analysis and Forecasting of Tropical Cyclone Intensities From Satellite Pictures. Vernon F. Dvorak, June 1972, 15 pp. (COM-72-10840)

NESS 37 Some Preliminary Results of 1971 Aircraft Microwave Measurements of Ice in the Beaufort Sea. Richard J. DeRyke and Alan E. Strong, June 1972, 8 pp. (COM-72-10848)

NESS 38 Publications and Final Reports on Contracts and Grants, 1971. NESS, June 1972, 7 pp. (COM-73-11116)

NESS 39 Operational Procedures for Estimating Wind Vectors From Geostationary Satellite Data. Michael T. Young, Russell C. Doolittle, and Lee M. Hace, July 1972, 19 pp. (COM-72-10910)

NESS 40 Convective Clouds as Tracers of Air Motion. Lester F. Hubert and Andrew Timchalk, August 1972, 12 pp. (COM-72-11421)

NESS 41 Effect of Orbital Inclination and Spin Axis Attitude on Wind Estimates From Photographs by Geosynchronous Satellites. Linwood F. Whitney, Jr., September 1972, 32 pp. (COM-72-11498)

NESS 42 Evaluation of a Technique for the Analysis and Forecasting of Tropical Cyclone Intensities From Satellite Pictures. Carl O. Erickson, September 1972, 25 pp. (COM-72-11473)

NESS 43 Cloud Motions in Baroclinic Zones. Linwood F. Whitney, Jr., October 1972, 6 pp. (COM-73-10929)

NESS 44 Estimation of Average Daily Rainfall From Satellite Cloud Photographs. Nelson A. Pollmanbee, January 1973, 30 pp. (COM-73-10539)

NESS 45 A Technique for the Analysis and Forecasting of Tropical Cyclone Intensities From Satellite Pictures (Revision of NESS 36). Vernon F. Dvorak, February 1973, 19 pp. (COM-73-10878)

NESS 46 Publications and Final Reports on Contracts and Grants, 1972. NESS, April 1973, 10 pp. (COM-73-11035)

NESS 47 Stratospheric Photochemistry of Ozone and NOx Pollution: An Introduction and Survey of Selected Developments Since 1969. Marvin D. Longmire, March 1973, 29 pp. (COM-73-10779)

NESS 48 Review of Satellite Measurements of Albedo and Outgoing Long-Wave Radiation. Arnold Gruber, July 1973, 12 pp. (COM-73-11443)

(Continued on inside back cover)

NOAA FORM 25-13 (2-73)

BIBLIOGRAPHIC DATA SHEET

U. S. DEPARTMENT OF COMMERCE
NATIONAL OCEANIC AND ATMOSPHERIC ADMINISTRATION

COM-75-11334

1. NOAA ACCESSION NUMBER
NOAA-75082801

2.

4. TITLE AND SUBTITLE
Nimbus-5 Sounder Data Processing System
Part II. Results

5. REPORT DATE
July 1975

6.

7. AUTHOR(S)
W.L. Smith, H.M. Woolf, C.M. Hayden, & W.C. Shen

8. REPORT NO.
NESS 71

9. PERFORMING ORGANIZATION NAME AND ADDRESS
National Environmental Satellite Service, NOAA
Washington, DC

10. PROJECT/TASK NO.

11. CONTRACT/GRANT NO.
Contract #S-70249-AG

12. SPONSORING ORGANIZATION NAME AND ADDRESS
GARP Project Office
National Aeronautics and Space Administration
Goddard Space Flight Center
Greenbelt, MD

13. TYPE OF REPORT AND PERIOD COVERED
NOAA Technical Memo.

14.

15. PUBLICATION REFERENCE
Nimbus-5 Sounder Data Processing System Part II. Results - July 1975, NOAA Technic
Memorandum NESS 71, Contract No. S-70249-AG

16. ABSTRACT

The Nimbus-5 spacecraft carries infrared and microwave radiometers for sensing the temperature distribution of the atmosphere. Methods have been developed for obtain temperature profiles from the combined set of infrared and microwave radiation measure ments. This data processing system was developed to provide global meteorological data sets to support the Global Atmospheric Research Program (GARP) and other research programs. Part I of this report described algorithms used to determine (a) vertical temperature and water vapor profiles, (b) cloud height, fractional coverage, and liquid water content, (c) surface temperature, and (d) total outgoing longwave radiation flux. This second part of the report presents the various meteorological results obtained from the application of the Nimbus-5 sounding data processing system during 1973 and 1974. (Author extracted)

17. KEY WORDS AND DOCUMENT ANALYSIS

17A. DESCRIPTORS

*Spacecraft, *Artificial satellites, *Meteorological satellites, *Spaceborne photography, *Radiometers, Communication satellites, Temperature distribution, Radiation measuring instruments, Algorithms, Water vapor, Clouds (meteorology), Surface temperature, Infrared equipment, Infrared radiation, Atmospheric physics, Temperature

17B. IDENTIFIERS/OPEN-ENDED TERMS

*Nimbus-5 spacecraft, *Nimbus-5 Sounder Data Processing System, Temperature profiles, Radiation measurements, Microwave radiation, Vertical temperature, Cloud height, Cloud distribution, Longwave radiation flux, Infrared radiometers, Atmospheric temperature

17C. COSATI FIELD/GROUP

4A, 4B

PRICES SUBJECT TO CHANGE

18. AVAILABILITY STATEMENT
Released for distribution: Robert R. Freeman

19. SECURITY CLASS (This report)
UNCLASSIFIED

20. SECURITY CLASS (This report)
UNCLASSIFIED

21. NO. OF PAGES
110

22. PRICE
5.25

NOAA FORM 25-13 (2-73) SUPERSEDES ALL PREVIOUS EDITIONS.

NOAA Technical Memorandum NESS 71

NIMBUS-5 SOUNDER DATA PROCESSING SYSTEM

PART II. RESULTS

W. L. Smith
H. M. Woolf
C. M. Hayden
W. C. Shen

Washington, D.C.
July 1975

UNITED STATES
DEPARTMENT OF COMMERCE
Rogers C. B. Morton, Secretary

NATIONAL OCEANIC AND
ATMOSPHERIC ADMINISTRATION
Robert M. White, Administrator

National Environmental
Satellite Service
David S. Johnson, Director

This memorandum was originally prepared for the GARP Project Office, National Aeronautics and Space Administration, Goddard Space Flight Center, under Contract No. S-70249-AG.

Mention of a commercial company or product does not constitute an endorsement by the NOAA National Environmental Satellite Service. Use for publicity or advertising purposes of information from this publication concerning proprietary products or the tests of such products is not authorized.

CONTENTS

Acknowledgments iv

Abstract 1

1.0 Introduction 1

2.0 Measurement characteristics of the Nimbus-5 sounders 2

2.1 The ITPR experiment 3

2.2 The NEMS experiment 6

2.3 The SCR experiment 7

3.0 Characteristics of the amalgamated Nimbus-5 sounding data . . 8

4.0 An intercomparison of the meteorological parameters derived from Nimbus-5 and those from radiosonde and NOAA-2 VTPR vertical temperature cross sections 10

5.0 An intercomparison of results obtained with the Nimbus-5 retrieval algorithm vs. real-time regression 14

6.0 Application of the Nimbus-5 sounding data to the study of tropical circulation 16

7.0 Application of the Nimbus-5 sounding system to Southern Hemisphere data 21

8.0 An intercomparison of radiosonde and Nimbus-5-derived cross-sections during the AMTEX 24

9.0 Evaluation of the Nimbus-5 sounding system during the May (1974) GARP Data Systems Test (DST) 28

10.0 Future developments 33

References 34

ACKNOWLEDGMENTS

The processing system described in this report was developed with the close cooperation of the NEMS and SCR experimenters. We wish to express our appreciation to Drs. D. Staelin and J. T. Houghton and their colleagues at the M.I.T. and Oxford Universities, respectively, for their continual support during the development of the Nimbus-5 data processing system. The assistance provided by the Meteorological Data Handling Center and the Technical Control Center of the Nimbus project is also greatly appreciated. Messrs. P. Gary, W. Holmes, and K. Iobst were responsible for converting the NESS-developed C.D.C. computer software required to implement the algorithms (described in part I of this report) to run on the NASA GISS IBM 360 for D.S.T. application. Finally, but most important, we thank all the members of the Radiation Branch, MSL and Computation Group of NESS Office of Research for their contributions to the development, debugging, and analysis of the results of this processing system. In particular we thank Messrs. H. Howell, P. G. Abel, N. Grody, M. C. Chalfant, L. Mannello, P. Pellegrino, R. Ryan, F. Nagle, G. Callan, W. Jacob and C. Jacobson for their invaluable assistance in these aspects of the system development. Out thanks also go to Mrs. M. Schwier for typing this technical manuscript.

NIMBUS-5 SOUNDER DATA PROCESSING SYSTEM
PART II: Results

W. L. Smith, H. M. Woolf, C. M. Hayden, W. C. Shen

National Environmental Satellite Service
National Oceanic and Atmospheric Administration
Washington, D. C.

ABSTRACT. The Nimbus-5 spacecraft carries infrared and microwave radiometers for sensing the temperature distribution of the atmosphere. Methods have been developed for obtaining temperature profiles from the combined set of infrared and microwave radiation measurements. Part I of this report described the algorithms used to determine (a) vertical temperature and water vapor profiles, (b) cloud height, fractional coverage, and liquid water content, (c) surface temperature, and (d) total outgoing longwave radiation flux. This second part of the report presents the various meteorological results obtained from the application of the Nimbus-5 sounding data processing system during 1973 and 1974.

1.0 INTRODUCTION

The Nimbus-5 spacecraft (launched December 11, 1972) carries several radiometers for sensing the temperature, water vapor, and cloud distribution of the atmosphere. The Infrared Temperature Profile Radiometer (ITPR), a second generation scanning infrared radiometer, observes the temperature distribution of the earth's surface, the troposphere and lower stratosphere with a spatial resolution of 15 n.mi. The Selective Chopper Radiometer (SCR), developed in the United Kingdom, enables temperature profiles to be obtained up to the stratopause. The Nimbus-E Microwave Spectrometer (NEMS), observes the vertical temperature distribution through and below clouds.

Since the infrared and microwave radiometers on Nimbus-5 provide highly complementary observations, one would expect to obtain better temperature profile results using the combined set of infrared and microwave observations than with either set individually. The National Environmental Satellite Service (NESS), with the financial support

of the National Aeronautics and Space Administration (NASA) and with the technical cooperation of the NEMS and SCR experimenters at the Massachusettes Institute of Technology and Oxford University, respectively, has developed algorithms for obtaining temperature profiles on a global basis using infrared and microwave radiances individually and in combination as described in Part I of this report (Smith, et al., 1974). This data processing system was developed to provide global meteorological data sets to support the Global Atmospheric Research Program (GARP) and other research programs. The essential characteristics of this data processing system are reviewed and some of the significant meteorological results obtained during 1973 and 1974 are presented in this report.

2.0 MEASUREMENT CHARACTERISTICS OF THE NIMBUS-5 SOUNDERS

Figure 1 shows the ITPR, NEMS and SCR instruments aboard the Nimbus-5 spacecraft. The ITPR (Smith, et al., 1972) measures radiation in seven different spectral intervals. Two of the spectral intervals are in the window regions at 3.7 μm and 11 μm for the purpose of detecting clouds and for obtaining surface temperatures, even when a partial cloud cover exists in the instrument's field-of-view. There are four atmospheric temperature profiling channels in the 15-μm CO_2 band and a single water vapor channel at 20 μm in the rotational water vapor absorption band. The instrument has a linear spatial resolution of 15 n.mi. and spatially scans in order to circumvent clouds and to obtain uniform earth coverage.

The NEMS instrument (Staelin, et al., 1972) is composed of five channels, three of which are in the neighborhood of the 0.5-cm oxygen absorption band and whose measurements are therefore useful for obtaining atmospheric temperature profiles. The instrument has relatively low spatial resolution (100 n.mi.) and does not spatially scan. However, these limitations are offset by its most important characteristic: the radiances it senses are not attenuated significantly by clouds. Thus, this instrument's measurements will yield temperature profiles through and below clouds. Also because it is possible to achieve much higher spectral resolution at microwave frequencies, the weighting functions are relatively sharp. This characteristic is particularly helpful in resolving the tropospause region.

The SCR (Houghton and Smith, 1972) is composed of sixteen channels. Four of its channels are in the most strongly absorbing portion of the 15-μm CO_2 band and employ CO_2 gas cells to separate absorption line center emissions from contributions from the line wings. When combined, they provide unique measurements, with relatively narrow weighting functions, of the temperature of the middle and upper stratosphere.

Figure 2 illustrates the vertical weighting functions for various spectral channels of the Selective Chopper Radiometer (SCR), Infrared Temperature Profile Radiometer (ITPR), and the Nimbus-E Microwave Spectrometer (NEMS) instruments flown aboard the Nimbus-5 satellite. The weighting function curves depict the layers most vividly sensed by the particular spectral channels. The SCR weighting functions pertain to high spectral resolution measurements of radiation due to the strong absorption lines at the center of the 15-μm CO_2 band. The ITPR weighting functions are due to four spectral intervals of the 15-μm CO_2 band ranging from the center to the wing of the band. The NEMS weighting functions are due to a complex of oxygen absorption lines near 0.5 cm. Differences in the weighting function widths and peak values are due to differences in the effective spectral resolutions of the various instruments.

The earth fields of view for the ITPR, NEMS, and SCR are shown in figure 3. As shown, the ITPR cluster samples within three different grids, one to the right of the orbital track, one in the center, and one to the left. NEMS and SCR samples only along the orbital track. The instantaneous resolutions of the ITPR, NEMS and SCR are 35 km, 192 km, and 43 km, respectively.

2.1 The ITPR Experiment

For useful temperature profile determinations from infrared radiation data, it is necessary to detect the existence of any cloud contributions to the observed radiances and to correct for these contributions before attempting to calculate the atmospheric temperature profile. For this purpose, the ITPR experiment employs moderate spatial resolution (15 n.mi.), spatial scanning, and channels for obtaining simultaneous radiance observations in the 3.7-μm and 11-μm windows. Since clouds impose the major obstacle to sounding using infrared measurements, it is worthwhile to explain how the ITPR experiment attempts to alleviate this deficiency.

Since molecular absorption is small in the 3.7-μm and 11-μm window regions, these ITPR window channels sense only the radiation from the earth's surface and any clouds within the instrument's field of view. When sensing a uniform and opaque scene (e.g., the earth's surface) they observe the same brightness temperature. However, when sensing a non-uniform or non-opaque scene (e.g., broken clouds within the instrument's field of view) they observe different brightness temperatures. This is because of the vastly different radiance dependence upon scene temperature for the two different wavelengths, a phenomena described by Planck's law. At 11 μm the radiance is approximately proportional to the fifth power of temperature, whereas at 3.7 μm the radiance is approximately proportional to the fifteenth power of temperature. Consequently, when looking at a scene composed of targets of different temperature, the 3.7-μm radiance will have a much larger relative contribution from the higher temperature target than will the 11-μm radiance. As a consequence the 3.7-μm channel

senses a higher brightness temperature than the 11-μm channel when the instrument's field of view is composed of a non-uniform temperature scene.

Figure 4 shows black and white images created from the ITPR brightness temperature data obtained in two different scan grids. Each picture is generated from observations for the 140 fields of view within the instrument's 200 n.mi. x 300 n.mi. scan grid area. The first scan grid (figure 4a) was observed over the South Pacific Ocean. The images of both the 11-μm and 3.7-μm window channel data clearly reveal the clouds (colder light regions) within the scan grid. The cloud features, especially the highest cloud bands, are even more clearly depicted in the pictorial image of the brightness temperature difference for the two window channels. The light regions correspond to the large negative window channel differences observed in cloudy fields of view and the dark regions to observations of the opaque ocean surface where the window channel brightness temperature difference is near zero. The second grid (figure 4b) was observed just two minutes later over the Northeast coast of Australia. In this case both window channels sense the cold (light) land surface in contrast to the slightly warmer (dark) ocean surface. It is evident from the window channel difference image that this feature is a surface coastline and not a cloud edge since the window channel differences are small (indicated by the dark shade) and their image is uncorrelated with either of the window channel images. These examples illustrate how simultaneous measurements in the 3.7-μm and 11-μm window channels detect the existence of cloud within the instrument's field of view unambiguously from a temperature contrast caused by a change in surface characteristics.

The images shown in figure 4 reveal the sensitivity of the ITPR-observed radiances to mesoscale features of the surface and atmosphere. Channel 7 water vapor brightness temperature images reveal dry (wet) vertical columns when the temperatures are high (low). Channels 3, 4, 5 and 6 depict variations in the temperature of atmospheric layers centered near the 2-, 6-, 12- and 20-km levels. Of particular interest is the dry zone (dark shaded region) sensed by Channel 7 and shown in figure 4b. This is apparently due to strong downward vertical motion associated with an intense high pressure system centered near 24°S, 156°E. Temperature and water vapor determinations from this radiance data revealed that in the region of sharpest gradient the water vapor concentration tripled in magnitude in a distance of less than 50 miles.

Simultaneous 3.7-μm and 11-μm window observations by the ITPR are used to specify surface temperature even when partial cloudiness exists within the instrument's field of view. This is possible using a set of geographically independent observations in which the radiance variation from one element to another is due primarily to clouds rather than surface temperature. Variations in cloud cover produce linear variations of the radiance in one window channel with respect to the

other and this characteristic is utilized to extrapolate the observations to their corresponding values for the cloudless sky condition. Once the clear-column window radiance is defined, clear column radiance values for the sounding channels are defined from their linear radiance relations to the window channel radiances. This technique is demonstrated graphically in figure 5 which shows a plot of 3.7-μm, 11-μm and 13.4-μm radiance observations in two adjacent scan elements, both of which possess some broken clouds but of different amounts. Also shown is the Planck function which relates the 3.7-μm to the 11-μm radiances for an opaque surface (i.e., a curve of equal 3.7-μm and 11-μm brightness temperature). Linear extrapolations of the observed values to the zero cloud amount condition, which is the intersection of the observation line with the Planck function curve, yields the window radiances which would have been observed if no clouds had existed within the instrument's field of view. The brightness temperature corresponding to this radiance is the surface skin temperature (in this case 293.5°K). Once the clear column radiance for the window regions have been determined, the clear column radiance for any sounding channel (e.g., the 13.4-μm CO_2 channel shown) can be specified. In the ITPR data processing, observations from groups of 16 geographically independent and contiguous ITPR fields of view are used to define "clear-column" radiances. This enables temperature profiles down to the earth's surface to be obtained under most cloud conditions with a geographical resolution of about 75 n.mi.

The vertical temperature profiles are obtained from Nimbus-5 radiance data using the "Minimum Information" inverse solution of the radiative transfer equation. The bias vector (guess profile) used in this solution is obtained from a regression model whose coefficients were derived from a historical sample of twelve-hundred radiosonde-rocketsonde profiles and corresponding theoretically calculated radiances. Since the routine data processing does not use contemporary conventional data, determinations in remote areas of the world are of the same quality as determinations in conventional data rich areas. (The details of the processing system are presented in Part I of this report.)

Shown in figure 6 is a vertical cross section of the atmosphere's temperature distribution calculated from the ITPR radiance data taken along the orbital track of Nimbus-5. Also shown are the cloud heights and amounts, total water content, and outgoing longwave flux which are also deduced from the ITPR data . As demonstrated, the temperature distribution down to the earth's surface could be specified from infrared data even under relatively severe cloud conditions. The latitudinal temperature distribution obtained is typical for this time of the year. The tropical regions possess a relatively warm lower troposphere and cold lower stratosphere. The polar regions have a moderately cold lower troposphere with a nearly isothermal stratosphere. A region of relatively warm air in the lower stratosphere exists in the temperate latitudes of the southern hemisphere.

Figure 7 shows how the ITPR data can be used to improve the specification of the atmospheric temperature distribution in the vicinity of intense weather systems. Shown are the ITPR derived 500-mb temperatures as the Nimbus-5 passed over an intense low pressure system over the Northern Pacific. (The symbol M denotes missing data due to extensive cloudiness above the 500-mb level.) It is worthy to note that the spatially random error of the deduced 500-mb temperatures appears to be of the order of a few tenths of a degree. As shown, the adjustments required to fit the National Meteorological Center (NMC) operational objective analysis to the satellite data in the area where conventional data are sparse are substantial, especially between 35° and 50°N. These adjustments result in improvements in the specification of the wind field in this area which could lead to an improved weather forecast.

Figure 8 shows a similar example, but over Northern Japan where there are numerous radiosonde observations which verify the ITPR measurements. As can be seen, the ITPR-deduced temperatures as well as the radiosonde temperatures reveal a much more intense temperature gradient than the NMC objective analysis. In fact, the hand analysis of the ITPR and radiosonde data implies maximum thermal wind speeds (which are proportional to the horizontal temperature gradient) and hence jet core winds which are twice the magnitude indicated by the operational analysis. It is significant to note that these small-scale features were accurately diagnosed from the ITPR radiance data even though more than half the area was covered by cloud, most of which was above the 500-mb level.

2.2 The NEMS Experiment

The NEMS experiment was conducted to show that sounding through clouds can be accomplished using microwave sensors. The absorption by clouds and aerosols in the 0.5-cm oxygen band is known to be orders of magnitude less than that in the infrared. Theoretical calculations show that most ice clouds are completely transparent to 0.5-cm radiation and liquid water clouds are only partially absorbent, the opacity depending on the total liquid water content. Since liquid water clouds are usually confined to the lower atmosphere, the effects of clouds on the microwave soundings would be expected to be negligible, unlike the case with infrared soundings.

Figure 9 shows several comparisons of soundings obtained from the NEMS microwave radiances with those obtained from ITPR infrared observations and by conventional radiosondes. These cases were selected because the cloudiness observed (by the ITPR) was extensive, probably of the convective type, and penetrated to high levels, thereby being representative of somewhat complex cloud conditions. Examples are shown in figures 9a and 9b of the general case where the microwave and infrared soundings both show good correspondence with the conventional radiosonde observation even though extensive cloudiness penetrated into the upper troposphere. The discrepancies between the satellite soundings and the

conventional radiosonde near the earth's surface are probably due to the time differences between the two observations, the satellite observations being taken at midnight and the radiosonde observations being taken four hours earlier. Figures 9c and 9d show similar cloud situations but in these cases the infrared soundings are erroneous below cloud level whereas the microwave soundings showed good agreement with the conventional radiosonde observations. In fact, the errors incurred in the calculation of the clear-column infrared radiances for case (d) were drastic enough to cause a ridiculous result from the highly error sensitive algorithm for radiance to temperature inversion. In the data processing such results are usually diagnosed to be erroneous from objective and internal checks on temperature lapse rate and the disagreement of the observed and calculated radiances. This, however, is not the case for the more subtle but relatively large (about 3°C) bias error in the infrared sounding shown in figure 9c.

Figure 10 shows the effect clouds associated with a tropical storm have on the NEMS microwave radiances and the soundings obtained from them. Shown at the top of this figure are the brightness temperatures observed by the NEMS 0.5-cm (50 GHz) oxygen channels and ITPR 15-μm CO_2 channels as the Nimbus-5 satellite passed over an intense tropical storm in the South Pacific at 9°S and 154.5°W. The maximum attenuation due to the storm is only 2.5°C for the microwave oxygen radiances whereas it is as much as 55°C for the infrared carbon dioxide radiances. As a result reasonable temperature profiles could be obtained from microwave radiances through the clouds down to the earth's surface, even at the center of the storm. Shown in the bottom portion of figure 10 is the difference, at each level, between the atmospheric temperatures obtained within the storm and those obtained in the cloudless air at the storm's boundary. Assuming that no actual variation in free-air temperature exists, the largest error incurred by this worst case cloud condition is only 3.5°C. (In practice the liquid water content of the cloud is also estimated from the NEMS 22-and 31-GHz channel data so that the attenuations by the cloud at 53.7 GHz can be accounted for in the temperature profile solution.) This latter example indicates that microwave instruments have almost complete cloud penetration capability under less drastic cloud conditions.

2.3 The SCR Experiment

As stated earlier, the SCR experiment has four channels at the center of the 15-μm CO_2 band which employ gas cells in the optical systems, each cell containing a different amount of CO_2. The CO_2 in the gas cells absorbs the radiation from the atmosphere near absorption line centers, the degree of which depends upon the amount of CO_2 in the cell. The upper layers of the atmosphere are observed by extracting the radiation from near the line centers. This is done by differencing the incoming radiation through a cell containing considerable CO_2 with that coming through a cell containing a smaller amount of CO_2. By this means unique observations of the temperature of the middle and upper stratosphere are achieved.

Figure 11 shows an example of temperature profiles obtained (1) from SCR upper channel radiance data combined with ITPR radiance data, (2) using only ITPR radiance data and (3) by a conventional rocketsonde observation. As illustrated, the SCR upper channel radiance data greatly improve the temperature profile specification in the middle and upper stratosphere.

3.0 CHARACTERISTICS OF THE AMALGAMATED NIMBUS-5 SOUNDING DATA

The amalgamated sounding data processing technique is centered around the ITPR measurements, with the NEMS and SCR providing supplementary data. The NEMS data is used only where it overlaps with the ITPR data along the orbital track. The SCR data is interpolated horizontally using an objective analysis routine so it can be used with off-nadir ITPR data grids.

Each ITPR data grid is divided into twelve 4 x 4 data subgrids, with some overlapping. The processing method yields "clear-column" radiances and a temperature profile from the ITPR data for each of the subgrids which are spaced about 150 km apart. The twelve subgrid clear column radiances are averaged over the grid and combined with the NEMS and SCR data to yield mean temperature profiles from (1) ITPR + SCR data, (2) NEMS + SCR data, and (3) ITPR + NEMS + SCR data.

Table I shows the results of a statistical analysis of ITPR and NEMS brightness temperature data and radiosonde observations of free air temperature in the troposphere and lower stratosphere. As can be seen from the individual channel brightness temperature correlations with radiosonde free air temperature observations, the ITPR and NEMS radiance channels are very complementary. The standard errors shown in figure 12 indicate that significantly better profile results can be achieved from the combined set of infrared and microwave measurements than can be achieved by either set used individually. This appears to be most dramatically evident in the tropopause region (i.e., the 100- to 300-mb region). This characteristic is illustrated in figure 13 which shows an example comparison between soundings obtained from ITPR and NEMS independently, and in combination, with a conventional radiosonde observation.

Figure 14 shows an analysis of the Southern Hemisphere 500-mb temperature distribution obtained solely from the amalgamated Nimbus-5 radiance data over a 24-hour period on April 5, 1973. Available radiosonde observations are given to validate the Nimbus-5 data. The agreement between the satellite-derived temperature distribution and the radiosonde observations is generally within 2°C. The significance of this result (and those for other levels not shown) is that it indicates that the temperature distribution of the atmosphere can be diagnosed accurately from the proper satellite radiation data without the aid of conventional observations.

Table 1--Statistical relations between ITPR and NEMS brightness temperature measurements and radiosonde air temperature observations (all latitudes, March-April, 1973).

Channel / Pressure level (mb)	Individual correlation coefficients							Multiple correlations (r) and Standard error (Se)						Standard deviation of radiosonde (K)
								ITPR		NEMS		ITPR & NEMS		
	13.4 μm	53.7 GHz	14.0 μm	54.9 GHz	14.5 μm	58.8 GHz	15 μm	r	Se(K)	r	Se(K)	r	Se(K)	
1000	0.99	0.95	0.94	0.34	-0.47	-0.86	0.63	0.99	2.3	0.98	4.0	0.996	1.9	20.2
850	0.94	0.98	0.96	0.45	-0.55	-0.91	0.51	0.98	2.5	0.98	2.2	0.984	2.1	12.1
700	0.93	0.98	0.97	0.48	-0.54	-0.90	0.50	0.99	2.1	0.99	2.1	0.991	1.6	12.0
500	0.91	0.98	0.97	0.55	-0.52	-0.89	0.50	0.98	2.2	0.98	2.3	0.987	1.9	11.7
400	0.86	0.97	0.96	0.62	-0.50	-0.87	0.47	0.98	2.3	0.97	2.5	0.983	2.0	10.9
300	0.71	0.86	0.87	0.79	-0.36	-0.78	0.42	0.95	2.5	0.96	2.3	0.965	2.1	7.9
250	0.08	0.28	0.32	0.77	-0.02	-0.27	-0.02	0.81	3.8	0.88	3.1	0.908	2.7	6.4
200	-0.59	-0.46	-0.42	0.30	+0.39	+0.41	-0.31	0.83	3.3	0.85	3.1	0.903	2.6	6.0
150	-0.84	-0.85	-0.84	-0.22	+0.54	+0.85	-0.45	0.89	2.8	0.91	2.5	0.925	2.3	6.0
100	-0.83	-0.91	-0.90	-0.42	+0.57	+0.93	-0.43	0.95	2.8	0.94	3.0	0.967	2.3	8.9
70	-0.81	-0.90	-0.87	-0.44	+0.61	+0.93	-0.38	0.95	2.5	0.94	2.6	0.957	2.3	7.8
50	-0.78	-0.83	-0.79	-0.27	+0.74	+0.93	-0.26	0.93	2.0	0.93	2.0	0.940	1.9	5.5
30	-0.15	-0.10	-0.04	+0.26	+0.57	+0.30	+0.27	0.67	2.8	0.51	3.2	0.686	2.7	3.7

4.0 AN INTERCOMPARISON OF THE METEOROLOGICAL PARAMETERS DERIVED FROM NIMBUS-5 AND THOSE FROM RADIOSONDE AND NOAA-2 VTPR VERTICAL TEMPERATURE CROSS SECTIONS

Comparisons are made of vertical cross-sections of radiosonde, Nimbus-5, and NOAA-2 Vertical Temperature Profile Radiometer (VTPR) temperature profiles which were observed at nearly the same time about a line extending from 60°S to 50°N on April 6, 1973. Figure 15 shows the distribution of the radiosonde, Nimbus-5, and NOAA-VTPR profile data analyzed. The satellite profile observations selected were those which were geographically closest to the radiosonde stations. Since the VTPR was spatially scanning, better space coincidence with the radiosonde observations was achieved than with the suborbital track-restricted Nimbus-5 data.[1] However, the more uniform north-south distribution of the Nimbus-5 data makes it more amenable to vertical cross-section analysis than the radiosonde or VTPR data.

Figure 16 shows the north-south distributions of cloudiness in percentages reaching various pressure levels, total precipitable water as derived from both the NEMS-microwave and the ITPR-infrared data, the total outgoing longwave flux (langleys/day) as derived from the Nimbus-5 radiance observations. Also shown is a pictorial image of the cloud distribution obtained from the 4 n.mi. resolution scanning Temperature Humidity Infrared Radiometer (THIR) instrument aboard Nimbus-5. Note in the THIR cloud photograph that apparently there are two jet streams (indicated by the cirrus streaks) crossing the Nimbus orbital track, a sub-tropical jet near 25°N, and a merging polar front jet near 35°N. As will be shown, the existence of these jet streams is verified by the thermal winds derived from both the satellite and radiosonde data.

Before proceeding with a discussion of the results, it is important to point out certain differences between the NOAA-2 and Nimbus-5 satellite temperature profile retrieval methods (for details of the NOAA-2 algorithms see McMillin et al., 1973).

(1) The NOAA-2 VTPR retrieval method uses the 12-hour forecast as an initial guess. The temperature profile obtained using the "Minimum Information Solution" (Fleming and Smith, 1972) is the minimum perturbation of the initial profile required to satisfy the outgoing radiance observations. As a result, vertical structure in the 12-hour forecast below the vertical resolution of the radiance observations is retained in the satellite profile retrieval.

---

[1] The Infrared Temperature Profile Radiometer (ITPR) on Nimbus-5 was designed with an east-west scan capability. Owing to a scan mechanism malfunction, however, the ITPR was restricted to the nadir-looking position during this orbit.

(2) As mentioned earlier, the Nimbus-5 (ITPR + NEMS + SCR) retrieval system utilizes regression equations relating temperature to radiances, generated from a climatological sample of radiosonde data, to obtain the initial profile used in the minimum-information solution. Consequently, the Nimbus retrievals are independent of contemporary radiosonde or forecast information.

(3) Figure 15 shows that the Nimbus-5, NOAA-VTPR, and RAOB data are not entirely coincident geographically. The most important systematic geographical discrepancy is north of 30°N, where the Nimbus data are located over China and the VTPR and radiosonde data are located over Japan.

Figures 17, 18, and 19 are cross-sections of RAOB, Nimbus-5, and VTPR temperatures. Figures 20 and 21 show the difference of Nimbus-5 and VTPR retrievals with respect to the radiosonde observations. In the troposphere, differences with the radiosonde (RAOB) are generally small except around 25°N where +6°C (Nimbus-5) and near 25°N where 10°C (VTPR) differences occur. Looking at figure 14, however, we see that the RAOB location is seven degrees west of the Nimbus-5 and VTPR observations. In the tropopause region, 300 to 100 mb, large differences of Nimbus-5 and RAOB observations result from vertical resolution limitations of the satellite sensor. The VTPR-RAOB differences are smaller because of the good "first guess" used in the VTPR retrievals. This is verified by the differences, shown in figure 22, between the 12-hour forecast (used as the VTPR first guess) and the RAOB. Since the Nimbus-5 retrievals do not use such contemporary first guess information, larger differences in the tropopause region are expected.

Note the vertical compensation of the errors. Probably the most important feature illustrated in figures 20 and 21 is that the errors (or differences) are spatially correlated so that one would expect smaller differences between the spatial gradients than between the point values.

Figure 23 shows comparisons of the horizontal gradients, over three degrees of latitude, at isobaric levels of temperatures derived from the RAOB and Nimbus-5 soundings. There is very good correspondence between the two fields of temperature gradients. The differences are probably within the noise level expected to exist between two RAOBS spaced 3° of latitude apart and those due to the different locations of the RAOB and the Nimbus-5 data.

Figure 24 shows comparisons of the geostrophic wind derived from the Nimbus-5 and RAOB temperature cross-sections. The overall agreement of the distribution of wind associated with the jet streams is quite good. This experimental result confirms the study based on theoretical computations presented by Togstad and Horn (1974). The different location of the

wind maximum is probably a result of the different longitudinal orientation of the RAOB and Nimbus-5 data (see figure 15). The fact that the Nimbus-5 pattern displays more character and stronger maximum winds is probably due to the higher density of Nimbus-5 soundings.

Figures 25 through 28 present various statistics obtained from the entire 60°S and 50°N cross-sections. Part (a) of each figure shows the standard deviations of the differences between the radiosonde profiles and those obtained from the dynamical forecast (i.e., the initial profile used in the VTPR solution), the VTPR soundings, and the Nimbus-5 soundings. Part (b) of each figure shows the correlation of the differences between the satellite soundings and the radiosonde observations with the differences between the forecast soundings and the radiosonde observations. Finally, part (c) shows the minimum standard deviation expected between the radiosonde observations and an analysis constructed by updating the forecast with the satellite soundings. This analysis procedure, initially suggested by Bonner (1974), consists of prescribing the analyzed temperature at each level as a linear combination of the forecast temperature and the satellite-derived temperature. The weighting coefficient of this linear equation is obtained through a minimization procedure. Its numerical value is a function of the expected standard errors of the forecast and the satellite retrieval, as well as the expected correlation of forecast and satellite profile errors. (In this analysis the radiosonde observations are taken as "truth" in computing these statistically expected values.)

Since here the weighting coefficient has been defined in an optimum way, using "the radiosonde truth" for its determination, the final analysis result is bound to be more accurate than either the forecast or satellite value. Although an optimum weighting coefficient cannot be defined in practice (since "truth" is always unknown), this analysis procedure is still a convenient way of illustrating the added information content of the satellite soundings over that already contained in the dynamical forecast.

In figure 25(a), we see that below the 500-mb level the Nimbus data agree much better with the radiosonde data than do the VTPR observations. This result is most likely due to the superior ability of the Nimbus-5 sounders to probe into, between, and through clouds. (The Nimbus-5 ITPR has four times the area resolution of the NOAA-2 VTPR, and the Nimbus-5 NEMS microwave instrument is able to probe directly through clouds.) In the tropopause region, however, the Nimbus-5 soundings are inferior to the VTPR profiles. The superiority of the VTPR profiles is probably a result of the incorporation of the 12-hour forecast in the solution. Evidence of this is given in the correlation coefficient profiles shown in part (b). We see that in the upper troposphere the error of the VTPR retrieval is highly correlated with the error of the 12-hour forecast, indicating that the forecast has a dramatic influence on the VTPR profile result.

It is interesting to note the high correlations of the error of the forecast-independent Nimbus-5 retrievals and the error of the forecast in the surface layer below 700 mb and in the 200- to 500-mb region. This is apparently due to the fact that both the forecast profiles and Nimbus-5 satellite profiles tend to smooth through fine scale vertical structures such as surface and tropopause inversions. Consequently, since both the forecast and satellite retrievals resolve a similar vertical scale which is larger than that resolved by the radiosonde, a high correlation results in regions where fine scale structure exists. The fact that the VTPR error is slightly less correlated than the Nimbus-5 error in the lower troposphere is probably a result of cloud noise.

Combining the satellite data with the 12-hour forecast using optimum weights yields the analysis result shown in figure 25(c). Note that the most dramatic influence of the satellite data is above the 700-mb level for both the Nimbus-5 and VTPR retrieval cases. The minor influence below 700 mb is a result of the relatively high error correlations (the vertical scale correlation discussed above), and the fact that the forecast profiles are relatively accurate. Remember, however, that the forecast is probably unrepresentatively accurate for this case since the cross-section area is within, and downstream of, a dense network of radiosonde data. Also, note that the large differences between the Nimbus-5 and VTPR standard deviations with radiosondes are greatly diminished when retrievals are combined with the 12-hour forecast using optimum weights to produce the analysis result. This result suggests that the differences between the two satellite profiles shown in figure 25(a) mainly are due to the difference in the initial profile used in the retrieval process and not to the information content of the radiance observations. The differences in information content of the two satellite sounding systems are more accurately reflected in 25(c).

Figures 26, 27, and 28 show similar statistical results for temperature gradients, geopotential heights, and geostrophic winds. In viewing the standard deviation portions (a) of each figure we note that, except for the Nimbus-5 derived geopotential height, the satellite results are generally inferior to the relatively accurate 12-hour forecast results. However, portion (c) of each figure reveals that the satellite data, when added to the forecast profiles to construct an analysis, leads to a significant reduction of the error of the forecast even though that error is relatively small (in this case). Of course one would expect to see an even more dramatic impact of the satellite data in situations where the forecast error is much larger, which is more likely to be the case in areas where radiosonde data are sparse.

In summary, this limited case study has revealed the following characteristics of the Nimbus-5 and VTPR temperature retrieval data:

(1) Much better agreement exists between temperature gradients derived from Nimbus-5, VTPR, and radiosonde data than between the absolute temperatures. (Compare figures 25 and 26.) This better agreement indicates that the satellite retrievals possess large horizontal scale bias errors which could be caused by (a) biases in the initial data used in the retrieval process (i.e., statistical or dynamical forecast data), (b) biases caused by aerosols or undetected large-scale cloudiness, or (c) systematic errors in the weighting functions.

(2) The geostrophic wind distribution associated with intense baroclinic phenomena such as the jet stream can be diagnosed accurately from the satellite temperature retrieval data. The results shown here indicate that the Nimbus-5 results may even be superior to radiosonde results, suggesting that the thermal gradients obtained from the closely spaced Nimbus data are more accurate than those obtained from the more coarsely spaced radiosonde observations.

(3) Even in regions where the forecast is relatively accurate, such as the case investigated here, the satellite retrieval data are sufficiently independent to provide an analysis with an accuracy superior to that of the forecast.

5.0 AN INTERCOMPARISON OF RESULTS OBTAINED WITH THE NIMBUS-5 RETRIEVAL ALGORITHM VS REAL TIME REGRESSION

As mentioned in earlier chapters, a principal aim of the Nimbus 5 processing was to achieve accurate and useful vertical temperature profiles which are independent of contemporary information obtained from other sources (e.g., radiosonde data and/or analyses and forecasts produced with other data)[2]. It was hypothesized that results obtained with the Nimbus 5 method might show larger absolute discrepancies with other data than results obtained with methods incorporating the other data, but it was hoped that the independence of the Nimbus 5 temperatures would compensate in terms of the utility of the data. To some extent this hypothesis has been verified in the discussion of chapter 4 where the Nimbus 5 temperatures are compared with VTPR results which use contemporary information. However, in those comparisons there are problems in that different instruments are involved and that the measurements are not colocated. In the following the hypothesis has been tested by comparing results obtained with the Nimbus 5 method with results obtained with a second method that differed only in replacing the climatological statistical bias vector (cf. chapter 1) with one obtained with real time statistics.

Data was taken from 1-5 April 1973 when all instruments were functioning normally. The dependent sample for the real time regression statistics was obtained from temperature fields analyzed at NMC, interpolated in space and time to the locations of Nimbus soundings. Exactly

[2]This aim was never fully realized because radiosonde data had to be used to tune the transmission function. However, tuning was infrequently done so the real data influence was not very contemporary.

as in the climatological statistics a dependent sample of 400 was generated for 3 latitude zones. No attempt was made to insure that the data were obtained from areas with good radiosonde coverage.

Verification of the temperatures obtained by the two retrieval methods was done on a very carefully selected set of matched radiosonde and Nimbus-5 soundings which occurred within 3 hours and 225 km of each other. The Nimbus data were screened to exclude all cases with significant cloud contamination or where the soundings indicated large spatial temperature variation. The radiosonde data were screened to exclude all obvious transmission errors and to include only cases where the radiosonde also reported 12 hours previously. The latter restriction assisted in error checking and also permitted the radiosonde/satellite comparisons to be segregated according to the observed variance of the atmosphere (as was done in the Data Systems Test verification discussed in chapter 8).

Table 2 presents the bias difference and standard deviation between the two Nimbus-derived and radiosonde temperature profiles. The encouaging part of the table is that there is little difference (except in the 150- to 100-mb layer) between the method using climatological statistics and that using real time statistics. The real time statistics yield consistently better, but only slightly better results. The disappointing feature of table 2 is that the bias errors associated with the climatological statistics are so large. Part of the bias is likely associated with the vertical resolution of the instruments since the variation of the bias with altitude is very similar for both methods. The remainder of the bias, however, would seem to represent the statistical resolution which is lost in replacing real-time with climatological statistics. As pointed out in earlier chapters the increased bias is probably of little consequence in terms of the utility of the data if they are treated in a relative rather than an absolute sense.

Table 2--Bias and standard deviation of Nimbus-derived mean temperatures derived from climatological and real-time statistics as compared to radiosonde observations

LAYER (mb)	BIAS (K)		STANDARD DEVIATION (K)	
	Climatological	Real time	Climatological	Real time
1000-850	-0.8	0.3	2.3	2.1
850-700	-0.1	0.3	2.3	2.2
700-500	1.3	0.2	1.8	1.6
500-400	2.2	0.6	1.8	1.6
400-300	2.1	0.7	1.6	1.5
300-250	1.1	1.0	2.8	2.4
250-200	-0.5	0.8	2.4	2.2
200-150	-2.0	-0.3	2.2	2.1
150-100	-1.4	-0.7	2.1	1.3

Figure 29 compares the results of the two retrieval methods as a function of the observed variance of the atmosphere in layers approximating the resolution of the 8-layer forecast model soon to be operational at NMC. (The uppermost layer is not shown because of the small sample

size). The observed variance has been determined by the 12 hours change registered by the radiosonde reports, and the sample size is successively reduced along the abscissas of the figure as cases with smaller 12 hour temperature changes are excluded. The values plotted are the RMS 12 hour change as measured by the radiosondes (heavy dashed line), the RMS difference between the same radiosondes and temperatures obtained with climatological statistics (light-dashed line), and the RMS difference between the radiosondes and temperatures obtained with real time statistics. As an example of reading the figure consider the sample of cases for the 850-700 mb layer where the 12 hour change in temperatures is at least 2K. The figure shows that the sample size is 14, the RMS temperature change is approximately 4.5, the RMS difference between radiosonde and climatological statistics method is approximately 1.8K, and the RMS difference between radiosonde and real-time statistics method is approximately 2.1K. In general the Nimbus 5 temperatures are a great improvement over 12 hour persistence, and they become increasingly useful as the atmospheric variance increases. Except for the 1000-850 mb and 300-200 mb layers the Nimbus error does not increase significantly with increasing atmospheric variance. As seen earlier in Table 2 the real-time statistical method gives better results in most cases, but the improvement is almost totally attributable to the additional bias errors introduced with the climatological statistics. Finally it is interesting to note that the trend of the RMS error is similar for both retrieval methods as the lines in the figure run nearly parallel. This effect would be caused by one or a combination of: noise in the verification method (i.e., real variance due to the inexact colocation of the radiosonde and Nimbus soundings); error in the radiances common to both retrieval methods; a lack of vertical resolution in the measurements; an error in the radiosonde sounding.

In summary there appears to be only one major difference between temperatures obtained with real-time statistical method or climatological statistical method. The difference is the size of the vertically distributed bias. Even with the bias both methods have been shown to produce temperatures much more accurate than 12-hour persistence values and with the bias removed the accuracies are in the neighborhood of the noise level of this type of verification. Since both methods demonstrate a significant bias problem it is evident that care must be exercised in using Nimbus temperature in conjunction with other data.

6.0 APPLICATION OF THE NIMBUS-5 SOUNDING DATA TO THE STUDY OF TROPICAL CIRCULATION

This study was conducted to determine the value of satellite sounding data, particularly that from the Nimbus-5, for diagnosing significant meteorological characteristics of the tropical atmosphere to be studied as part of the GARP Atlantic Tropical Experiment (GATE). Example results were obtained for late July and August 1973 to demonstrate the capability of the satellite infrared sounder for providing useful data for the study of tropical circulation and energetics as well as to illustrate some of their shortcomings.

Figure 30 is a time cross-section of temperature (departure from mean), water vapor, cloudiness, and outgoing flux as specified from ITPR radiance data for the GATE B-scale area (5-15°N, 21-31°W). The temperature, water vapor, and flux values represent mean values for an entire ITPR grid (a 200 x 300 n.mi. area) so that the variations shown can be attributed to the passage of A-scale waves as well as large-scale convective processes responsible for "cloud clusters". The temperature variations shown over this brief period are well organized and therefore are probably associated with A-scale wave phenomena. The greatest amplitude (about 1.5°C) of the well organized temperature variations appears in the upper troposphere near 350 mb. The lower stratospheric variations near 50 mb seem to have a higher frequency (3-4 day period) although lower amplitude (about 1°C) than the tropospheric variations. Also interesting is the tendency of a local warming (by as much as 3°C) of the tropopause region (near 100 mb) to occur after strong convection has taken place.

The total water vapor content of the atmosphere derived from the ITPR data varies by more than 100%, a range of 2.5 - 5.5 gm/cm^2. The total outgoing longwave radiation flux varies by less than 25% and as expected is inversely correlated with the total moisture and the degree of cloudiness derived from ITPR radiances.

The large-scale temperature variations indicated by the ITPR data are about five times as large as those estimated from the "statistical compositing" of radiosonde data. (Statistical compositing techniques are necessary because noise due to instrumental error and small scale processes in a spot radiosonde observations is generally greater than the maximum amplitude of the large-scale thermal wave). Consequently, one might seriously question the satellite data. Unfortunately it is difficult to verify the ITPR-derived level temperatures in the tropics using radiosonde data. The RMS difference between the two sets of observations is generally higher than the small standard deviation of either estimate about the mean. The skill of the satellite data can be demonstrated, however, by comparing layer average temperatures derived from the ITPR data with layer averages of the radiosonde profiles. In this case the radiosonde (mean) temperature is more representative of the vertical resolution of the satellite-derived temperature and the vertically random errors are minimized in the averaging process.

Figure 31 shows some comparison statistics for layers extending from the surface (1000 mb). As may be seen, for the 1000-mb level the standard deviation of the difference between the ITPR and radiosonde data is much higher than the standard deviation of the radiosonde data about the mean. However, for layers thicker than 200 mb the standard deviations between the two observations are significantly less than the radiosonde standard deviation about the mean, being less than 1°C for layers extending to and beyond the 500-mb level. Also noteworthy is the large mean difference of more than 1°C at low levels which diminishes with altitude. This apparent cold bias in the ITPR low level temperature derivations are believed to be caused by very small low level cumulus clouds which cannot be resolved by the ITPR instrument.

Figure 32 shows similar results for layers extending from the 500-mb level. For example, at 500 mb the standard deviation between the ITPR and radiosonde temperatures is 1.5°C whereas the variability about the mean estimated from the radiosonde data is only 1.2°C. However for the 500-200-mb layer the standard deviation between the ITPR and radiosonde data drops below 1°C whereas the expected natural variability is greater than 1.5°C. The mean difference between ITPR and radiosonde data is near zero for the upper tropospheric layers.

Based upon the above statistics an attempt was made to verify the time variations of layer mean temperature indicated by the ITPR data near Cape Verde (just north of the B-scale area) with the Cape Verde radiosonde data. Figure 33 shows an encouraging result in that where significant variations in the layer mean temperature occurred, the ITPR and radiosonde variations correspond (e.g., the 3°C drop between the 23rd and 25th and the subsequent 4°C rise between the 25th and 29th of July). Thus, the verification of the ITPR data with respect to radiosonde data lends credibility to the amplitude of the temperature variations diagnosed for the GATE B-scale area.

Analyses of various meteorological parameters derived from ITPR radiance data have been constructed for the entire GATE A-scale area. Figure 34 shows some example analyses of outgoing longwave flux for 3 days in late August. The longwave flux pattern is dominated by the cloud and moisture distribution and the surface temperature distribution over North Africa near the Sahara Desert. The lows follow the Inter Tropical Convergence Zone and moisture highs (as will be shown later) except over Africa where the low flux values and cloudiness (as indicated from cloud pictures are shifted 5 degrees to the south of the moisture maximum. Highest values occur over the Sahara desert and over the subtropical high pressure regions in the Northern and Southern Hemispheres.

Figure 35 shows corresponding analyses of total precipitable water derived from the ITPR radiance data. In general the moisture field is quite reasonable in that highest values correspond to regions of strong convection along the ITCZ and the dry zones are confined to the Sahara Desert and the subtropical anticyclones. A major exception occurs over Africa where the ITPR derived moisture maximum is displaced 5-7 degrees north of the region of the deepest convection cloudiness.

An analysis of the available surface and radiosonde data over Africa reveals that the derived moisture maximum coincides with the region of maximum surface wind convergence but that the total precipitable water estimates from the ITPR are erroneously high (by as much as 100%). (It is well known that over Africa, the region of maximum convection is shifted about 5 degrees south of the region of maximum surface wind convergence. This is due to the overrunning of the Southwest Monsoon by hot dry Sahara air producing stable conditions which do not allow deep convection to take place.) On the other hand the moisture estimates to the north and south of this region compare well (generally within 20%) of available radiosonde data. One possible explanation for the erroneously high water vapor estimates along the

relatively cloud-free ITCZ over Africa is the attenuation of the radiance measurements by dust blown southward from the Sahara which might tend to concentrate in the low level convergence zone. Although more studies must be done to support this explanation, the erroneous result certainly indicates that satellite profiles may be seriously compromised by Sahara dust, which is known to reach altitudes as high as 10,000 feet.

Figure 36 shows a comparison of the sea-surface temperature for July and August derived from the ITPR window channel radiance data with climatology based on 60 years of ship data. In general there is a close correspondance between the overall patterns; e.g., both show relatively cold water along the African coast north of 15°N, due to the cold Canaries Current, and south of 5°N, due to the Benquela Current. Relatively warm water stretches across the Atlantic in the vicinity of the ITCZ (10°N).

The most dramatic departure of the ITPR-derived surface temperature patterns from the climatological mean charts occurs off the northeast coast of Brazil where the satellite data shows a pool of relatively warm water. One can see an apparent southward shift of the warm pool between the July and August analysis periods.

A close inspection of the sea surface temperature charts reveals that the ITPR-derived values are generally lower than the climatology. Figure 37 shows that the largest differences, which are as much as 4.5°C, are confined to the zone of maximum water temperature along the ITCZ. Some differences are expected due to actual deviations from the climatological mean and to physical differences between surface skin temperature and the water temperature sampled several meters below the surface by commercial ships. However, these bias differences are excessive and clearly indicate that the ITPR sea temperatures are erroneous in the vicinity of the ITCZ. An analysis of high-resolution cloud picture data indicates that this cold bias is caused by small radiometric attenuations by low level "popcorn" trade cumulus which are not detected as being within the ITPR field of view. This low-level cumulus tends to be uniformly distributed across the Atlantic Ocean in the ITCZ.

Figure 38 shows a scatter diagram of available ship observations in the North Atlantic and the analyzed ITPR-derived sea surface temperatures for the GATE area. As can be seen, the mean difference is almost 3°C and the bias is a function of surface temperature. This result indicates that more work is needed to reduce the error of the satellite-derived sea-surface temperatures to an acceptable level, particularly in the Intertropical Convergence Zone. However the correlation coefficient of 0.7 and standard error of regression of 1.25°C are encouraging, especially since the ship temperatures cannot be expected to be representative of surface skin temperatures to within 1°C.

Figure 39 shows the temperature distribution at the 850-mb level as determined from the ITPR radiance data. As shown the space and time variations of temperature in the lower troposphere are small (<2°C) over the oceans. Over Africa, however, large horizontal gradients caused by the different radiational characteristics of the land masses and oceans are clearly depicted by the ITPR derivations. High surface temperatures over the Sahara and low ocean surface temperatures to the west cause sharp meridional gradients north east of the Cape Verde Islands. The relatively cool air south of 10°N along the west coast of Africa is associated with the advection of cooler maritime air by the prevailing southwesterly winds.

Figure 40 shows the derived temperature distribution for the 250-mb level. As may be inferred, the gradients over Africa seen at the 850-mb level diminish with altitude and then re-appear in the opposite sense at the 250-mb level. For example, over the western Sahara it is relatively cold at the 250-mb level.

Although the horizontal gradients are much smaller than at the 850-mb level, due to the lack of surface influences, the local temperature changes appear to be much greater reaching 4°C over the four day period in many areas. At 850 mb the local changes rarely exceed 2°C over the four day period. This result probably reflects the influence of large scale traveling waves which are known to be associated with larger temperature variations in the upper troposphere than in the lower troposphere. The strong and persistent meridional temperature gradient across the Sahara desert at the 250-mb level is also noteworthy.

Finally figure 41 shows the deduced temperature distribution for GATE region at the 100-mb level. At 100 mb, the development and intensification of warm and cold cells can be seen, as in the closing off and intensification of neighboring warm and cold cells over South America. On the 25th, warm air is located just off the northwest coast of South America and cold air is dominating the middle of South America near 10°S. By August 27th the warm and cold air have been cut-off and displaced slightly eastward. The gradient between the two systems is less than 4°C. By August 29th however the two systems have greatly intensified with the gradient being larger than 6°C and the warm air displaced about 5 degrees of latitude northward.

In summary, the results of this fairly limited analysis of the Nimbus-5 ITPR data indicate that the small but organized temperature fluctuations associated with the passage of A-scale waves and convection processes in the tropics can be detected with the Nimbus-5 ITPR sounder. As a result, this data should prove to be a valuable tool for interpolating the information to be derived from the more spatially limited conventional surface radiosonde data to be collected during the

GATE experiment. The moisture, cloud, and temperature information appears to be of sufficient quality for obtaining reasonable energy flux divergence estimates.

There are two major shortcomings of the infrared derivations revealed in this limited study:

(1) Erroneously high values of moisture result along the surface wind convergence zone over Africa, due to radiance attenuations in the 20-μm water vapor channel possibly caused by dust advected southward from the Sahara Desert.

(2) Erroneously low sea-surface temperature estimates are obtained along the Intertropical convergence zone due to attenuations caused possibly by the uniformly distributed "popcorn" trade cumulus clouds which are well below the resolution of the ITPR instrument. More research is needed to alleviate these difficulties.

7.0 APPLICATION OF THE NIMBUS-5 SOUNDING SYSTEM TO SOUTHERN HEMISPHERE DATA

In this chapter results are presented for the Southern Hemisphere's winter of 1973 which demonstrate the quality of the Nimbus-5 derived quantities in conventional data-sparse areas and their usefulness for specifying the state of the oceans and atmosphere of the Southern Hemisphere.

The meteorological parameters derived on the synoptic scale from Nimbus-5 satellite data are illustrated for the Southern Hemisphere in the Equator to South Pole cross-section for August 11, 1973, shown in figure 42. The derived parameters are temperature, water vapor, cloud heights and amounts, and total outgoing longwave flux. The temperature and water vapor distribution diagnosed from the Nimbus radiance measurements is typical for this time of the year. The coldest air exists over the Antarctic continent near the 30-mb level where the temperature is below -90°C. The lower stratosphere is relatively warm at mid-latitudes. The Southern Hemisphere polar front near 30°S is clearly depicted in both the temperature and water vapor distribution. As can be seen there are sharp temperature gradients near the earth's surface and the axis of the sloping isotherms shifts poleward with altitude. The total precipitable water drops from 4 gm/cm^2 in the warm air ahead of the front to below 1 gm/cm^2 in the cold air behind the polar front. There are also sharp gradients of atmospheric temperature in the troposphere and an increase in convective cloudiness associated with an Antarctic front near 67°S.

In order to assess the ability of the Nimbus-5 sounding system to provide synoptic scale data useful for Southern Hemisphere weather forecasting, example analyses of the Nimbus data are presented for a large geographical region surrounding Australia and New Zealand during an active mid-winter period, August 1-11, 1973. The satellite derived meteorological analyses depict weather developments in the conventional data sparce Indian Ocean upwind from Australia and New Zealand. The analyses of the satellite data in the conventional data-rich Australia and New Zealand areas allow for verification of the satellite results. It is important to reiterate the fact that the analyses were obtained solely from the Nimbus data (i.e., no conventional data was used in either the parameter deviations or in the analysis of them). Also, since the satellite data is not synoptic, 24 hours of satellite data centered about 00GMT of each day had to be used to construct the daily analyses.

Figure 43 shows an example analyses on a distorted latitude-longitude grid of sea-surface temperature for four days in August (2, 5, 8, and 11), spaced three days apart. As may be seen, the overall features are stable in the manner one expects the sea surface temperature to behave. Two exceptions to this stability occur on August 2 near 45°S and 80°E and on August 11 just off the southwest coast of Australia. In both cases the temperatures are believed to be erroneously low due to radiance contamination by low clouds. (The temperatures of low clouds do not differ from the surface temperature enough to be detected in the cloud filtering scheme used to process the Nimbus data.) Some of the more subtle variations revealed may be related to the passage of an intense cold front during this period. The known persistent characteristics of the sea-surface temperature distribution such as the relatively cool water off the northwest coast of Australia due to the West Australian current and the relatively warm water off the southeast coast of Australia due to the East Australian currents are visible in the Nimbus derivations.

Figure 44 shows the 850-mb temperature distribution for this time period. As may be seen, the low-level Nimbus temperature data reveal a cold front developing in the South Indian Ocean, intensifying greatly as it moves across the southwest coast of Australia and then dissipates as it moves off the East Coast of the Continent. Local temperature variations of 15°C occurred at the 850-mb level along the southern coast of Australia with the passage of this cold front.

Figure 45 shows the Nimbus satellite-derived temperature field for the 500-mb level. Also shown are available 300-mb rawinsonde wind observations to demonstrate geostrophic correspondence between the derived temperature field and the circulation changes with this frontal passage. (It is reemphasized that the Nimbus analyses were obtained completely independent of conventional wind or temperature data.) As

shown the agreement between the satellite derived temperature field and the rawindsonde wind observations is amazingly good as far north as 10°S. (This is despite the fact that the satellite analyses were derived from data obtained over the 24-hour time interval centered about 00Z of each day.) Note the apparent development of another front off the southwest coast of Australia on the last day, August 11. There is no evidence of this development in the available wind observations on the west coast.

Figure 46 shows the thermal patterns at the 100-mb level. At this lower stratospheric level the variations in temperature are inversely correlated with those shown to be taking place in the troposphere.

The formation, intensification, movement, and decay of this frontal system is even more dramatically displayed in the total precipitable water vapor patterns derived from the Nimbus radiance data. As shown in figure 47 a moisture tongue is just beginning to penetrate southeastward from the northwest coast on August 2. By August 5 the moisture tongue has penetrated along the front down to the southeast coast of the Continent. Sharp moisture gradients exist due to dry air over the northwest desert, very moist warm air just ahead of the front, and extremely dry cold air behind the front. Note that the moisture tongue tends to be wiped out in the northern part of Australia as the front crosses the desert. On August 11, we see the southeast penetration of another moisture tongue associated with the development of another frontal system off the west coast of the Continent.

The satellite-derived temperatures have been compared with isotherm analyses of radiosonde observations in the conventional data rich areas. Figure 48 shows the results of a statistical comparison of the mean temperatures for layers defined by the standard atmospheric pressure levels.

As may be seen, the standard deviation of the satellite-derived temperatures and the radiosonde-observed temperatures are nearly identical except at the earth's surface and in the tropopause region. In both regions the variability of the satellite temperatures is less than the radiosonde-observed temperature variability. This feature is probably a result of the lower vertical resolution of the satellite temperature profiles. The RMS difference between the satellite and the analyzed radiosonde observations is less than 2°C except in the tropopause region where the difference approaches -3°C. The mean difference is near zero, except in the lower stratosphere where the mean difference is close to 1°C.

Finally, figure 49 shows a comparison of the geopotential height profiles derived from the satellite and radiosonde temperature data. As may be seen, there is excellent agreement between the relative geopotential height profiles, their RMS differences being less than 50 meters

throughout the troposphere and their maximum RMS difference being about 65 meters at the 100-mb level. This result suggests that good initializations of the mass field for dynamical weather prediction models for the southern hemisphere can be made from the Nimbus satellite temperature profile data.

8.0 AN INTERCOMPARISON OF RADIOSONDE AND NIMBUS-5 DERIVED CROSS-SECTIONS DURING THE AMTEX

An Air Mass Transformation Experiment (AMTEX) was conducted over the East China sea near Okinawa, Japan from February 14 to 28, 1974 (GARP, 1973). The experiment was conducted to increase our understanding of the air-sea interaction which occurs during the modification of the cold polar continental air mass when it flows over the warm ocean.

During the AMTEX observational period, four orbits of the Nimbus-5 satellite were over the AMTEX area. Orbital number and the synoptic situation during the orbital transverses are given in Table 3. Figure 50 shows the Nimbus-5 orbital tracks and the locations of nearby radiosonde stations. Note that the orbits of February 16, 18, and 23 were decending at night whereas the orbit of February 27 was ascending over the AMTEX area during the daytime.

The purpose of this study is to compare meteorological parameters derived from the Nimbus satellite radiance measurements with those derived from the conventional radiosondes in order to assess the usefulness of satellite observations for diagnosing the intense weather situation under study during AMTEX.

Table 3--Orbit number and synoptic situation

Date	Orbit no.	Time (U.T.)	Synoptic situation
2-16-74	5804	1509-1517	Weak monsoon and warm weather. Cold front passed through the AMTEX area at 1200Z.
2-18-74	5830	1525-1534	Weak monsoon, migratory anticyclone centered over Japan Sea.
2-23-74	5897	1512-1521	Weak monsoon, intense cold front passed through AMTEX area between 0600Z and 1200Z. However, a strong anticyclone built up over Siberia ready to sweep over China.
2-27-74	5944	0242-0251	After polar air outbreak, open and closed cell cumulus convection was observed in the AMTEX area.

The total water vapor contents derived over the Kuroshio area are given in Table 4. The total water vapor contents derived from the microwave sounder and from the infrared temperature profile radiometer are in good agreement with those obtained from the radiosondes. The NEMS total water vapor contents are larger generally than those of the ITPR because the microwave energy penetrates clouds and the water vapor content of clouds is usually larger than the surrounding clear air sampled by the infrared observations. Note that the total water vapor contents in the first 3 days (February 16, 18, and 23) are 1 to 2 times higher than the day after the cold polar air outbreak (February 27).

Table 4--Total water vapor content (g/cm^2) over the Kuroshio region

Date	Synoptic condition	NEMS	ITPR	RAOB
2-16-74	Quiet period	2.9	2.6	2.8
2-18-74	Quiet period	2.6	1.9	2.3
2-23-74	Prior to polar air outbreak	3.5	2.2	2.9
2-27-74	After polar air outbreak	1.3	1.4	1.0

Figures 51 through 54 show the distribution of atmospheric water vapor content, radiative flux of outgoing longwave radiation, and the cloud cover as derived from the Nimbus-5 radiance measurements. Also shown is a pictorial image of the cloud distribution obtained from the four-mile resolution scanning THIR instrument aboard Nimbus-5.

As shown in figures 51 through 54, the flux of outgoing longwave radiation derived from the ITPR radiance data has a large variation because of non-uniform temperature of the underlying surface and the varying height and amount of clouds. The low radiation fluxes are associated with high dense clouds or low surface temperature in the north. On February 16, 1974 there were three areas of low outgoing radiation flux located near 25N, 35N, and 50N. The positions of these radiation minimums agree with the frontal cloud systems indicated on the NMC operational surface synoptic map (not shown) and also on THIR cloud image.

The lowest flux -- 360 langley/day -- was observed in the AMTEX area on February 23, just before the outbreak of the cold polar air mass. This low flux was due to the cloudiness associated with the intense cold front extending from an active cyclone located to the southeast of Japan. The maximum outgoing radiation flux of 600 langley/day observed in the AMTEX area occurred under clear sky conditions on February 16 and 18.

Figures 55 through 58 show the meridional temperature cross sections, plotted from 20N to 50N latitude and from 1000 mb to 10 mb. There are three parts in each figure. Part (A) shows the radiosonde temperature observations; part (B) the original temperatures derived from Nimbus-5 (ITPR+NEMS+SCR) radiation measurements; and part (C) the Nimbus-5 temperatures after correcting for systematic differences between the Nimbus and radiosonde level temperatures (i.e., the level mean error is removed).

The pattern of the Nimbus-5 temperatures follows closely those of the radiosondes. These is generally better correspondence between the two fields of temperature gradients than their absolute values. In fact, by removing the level mean difference between the satellite and radiosonde temperatures enables good agreement to be obtained between the satellite and the radiosonde cross-sections.

Perhaps the best way of determining how well the thermal field derived from the Nimbus data describes the state of the atmosphere is by comparing the geostrophic wind distribuiton obtained from it with the geostrophic wind obtained from the radiosonde temperature profiles and with the true wind distribuiton also observed by the rawinsonde. (The geostrophic wind computations were performed assuming zero wind velocity at the 1000-mb level.)

Figures 59 through 62 show a comparison of geostrophic winds derived from the Nimbus-5 temperatures, the radiosonde temperatures, and the radiosonde winds. (For locations of Nimbus-5 and radiosonde temperatures see figures 55 through 58.) The relatively good depiction of the wind field associated with the jet stream from the satellite data again confirms the study based on theoretical computations presented by Togstad and Horn (1974). The latitude and altitude locations of the jet core (wind maximum) from the satellite-derived temperature profiles appear to be more accurate than the location indicated by the radiosonde temperature profiles on three of the four days studied, despite a three hour time difference between the satellite and radiosonde observations. The best agreement is on February 18 for which the Nimbus orbital track is closest to the radiosonde stations (figure 50). Table 5 below summarizes the major jet stream features given in figures 59-62.

Table 5--Major features of the observed (true), radiosonde-derived (geostrophic) and satellite-derived (geostrophic) zonal wind distributions

	Altitude of max. wind (mb)			Latitude of max. wind (°N)			Intensity (m/s)		
	obs	sat.	RAOB	obs	sat.	RAOB	obs	sat.	RAOB
2-16-74	275	250	175	33	34	31	70	90	90
2-18-74	225	225	175	30	32	35	70	80	70
2-23-74	250	250	250	38	34	41	60	80	80
2-27-74	250	250	250	31	31	33	80	90	80

The reason for the higher accuracy of the satellite data for geographically locating the jet core is probably a result of the relatively high density of Nimbus-5 soundings as compared to the coarsely spaced radiosondes along the suborbital track. The reason for somewhat better altitude positioning of the jet core is not entirely clear. The satellite-derived vertical profiles generally smooth the sharp discontinuities of atmospheric temperature observed by the radiosonde near the tropopause where the jet core is found. Possibly the smoothing helps alleviate error amplification due to the finite difference approximation used in the numerical computation of the geostrophic wind. In any case, the results shown in figures 59 through 62 certainly indicate that the tropopause smoothing inherent in the satellite profiles has no adverse effect for defining the location of the jet core.

It is interesting to note that for February 16 and 23 (figures 59 and 61) both the satellite and radiosonde derived geostrophic winds show a double maximum indicating the existence of two jet cores. This result is not verified by the actual zonal wind distribution. However the existence of two cirrus cloud streaks on February 23 is evident in the THIR photograph and the ITPR deduced cloudiness (figure 53) at the locations indicated in figure 61B. The cores of maximum wind are to the north of the extensive cirrus bands near 30° and 35°N along the satellite track. Thus the cirrus cloud streaks and the thermal winds indicate two cores of maximum wind instead of a single one as deduced from the rawindsonde data. The inability to diagnose the two jet cores from the rawindsonde data may be due to the horizontal spacing of the observations (see figures 50 and 57A).

In summary the comparison of meteorological parameters derived from the Nimbus-5 radiance measurements with those of the radiosondes for 4 days during AMTEX indicate the following:

(1) The total water vapor contents derived from the Nimbus-5 infrared temperature profile radiometer and the microwave spectrometer are in fair agreement with each other and with measurements by radiosondes. All observations show that during the cold polar air outbreak, the total water vapor content over the Kuroshio region was close to 1 g/cm^2. Prior to the cold air outbreak, the total water vapor content was about 3 g/cm^2 in the same region.

(2) The regions of low outgoing longwave radiative flux correspond well with the areas of deepest convection indicated on cloud photographs.

(3) There is good agreement between the vertical cross-sections of temperatures derived from the satellite and from the radiosonde observations.

(4) The geostrophic zonal wind distribution associated with the jet stream can be accurately diagnosed from the satellite temperature retrieval data. (The Nimbus-5 geostrophic zonal wind appears to have somewhat better correspondence with the actual zonal wind distribution than that derived from radiosonde temperature data possibly because of the observation density.) The inherent smoothing of the vertical temperature which occurs in the tropopause region does not seem to degrade the satellite-inferred geostrophic winds near the jet core.

9.0 EVALUATION OF THE NIMBUS-5 SOUNDING SYSTEM DURING THE MAY (1974) GARP DATA SYSTEMS TEST (DST)

Soundings from the Nimbus-5 satellite were processed in real time at the Goddard Institute for Space Studies (GISS) and transmitted to the National Meteorological Center to be included in the global numerical analysis-forecast operation conducted during the May test.

For the global experiment, both the yield and information content of the satellite soundings are important. Table 6 shows an example of the yield of soundings obtained completely down to the earth's surface from Nimbus-5 for a typical day during the 15-day test.

Table 6--Example yield statistics (May 9, 1974)

Latitude Zone	Total number of soundings possible	Percentage of soundings for which clear column radiances could be derived [1]	Percentage of clear column radiances yielding acceptable temperature profiles [2]
60°N-90°N	134	77	98
30°N-60°N	191	83	96
30°N-30°S	370	90	98
30°S-60°S	186	90	99
60°S-90°S	184	63	73
TOTAL	1065	82	93

[1] Passed quality control tests in the clear radiance algorithm.

[2] Passed quality control tests in the temperature inversion algorithm.

Since soundings obtained in overcast cloud situations were not believed to be reliable, only soundings derived for situations where ITPR clear column radiances could be obtained were transmitted to NMC for archival. Since the ITPR was not spatially scanning during May due to a malfunction of its scan system, the total yield of soundings was severely limited during this test. As shown in Table 1 the percentage of cases in which clear-column radiances were obtained decreased from 90% in tropical regions to 77% and 63% in the north and south polar regions, respectively. It is, however, encouraging to note, from the last column of the table, that most of the temperature profiles derived from the clear-column radiance soundings were judged to be good on the basis of internal checks in the retrieval program. An exception occurs in the Antarctic region where the percentage of good soundings is low, presumably due to problems associated with the height of the continent and with the difficulty of detecting cloud contamination in the inverted or isothermal lower polar atmosphere. These yield statistics indicate that special attention should be given to improving our retrieval techniques for the polar regions.

It is important to note that because the HIRS-infrared and SCAMS-microwave sounders on Nimbus-F (scheduled for launch June 12, 1975) both spatially scan, the retrieval yields are expected to improve markedly for the 1975 DST.

The quality and information content of the temperature profile determinations from Nimbus during the DST is investigated here in two ways. First statistics comparing satellite-derived temperature and thickness values to radiosonde measurements are presented for a sample taken during the second week of the DST. Second, a cross-section of Nimbus-derived temperature profiles through a weather system is compared to a cross-section of contemporary radiosonde profiles near the satellite orbit. For this case thermal wind distribution is computed to determine how well the Nimbus temperature profiles defined the atmospheric circulation associated with the frontal condition.

Table 7 presents the bias difference and standard deviation between the Nimbus-derived and radiosonde temperature profiles. The sample consists of 90 sets of profiles in which the satellite and radiosonde observations were made within 3 hours and 225 km of each other. The bias difference shown in Table 7 is significant, especially at low levels. The generally negative bias indicates a calibration uncertainty of Nimbus sensors. The increase in the bias with decreasing pressure is most likely caused by cloud contamination which is a serious problem with the ITPR instrument restricted to the non-scanning nadir mode due to a prior malfunction of its scanning mechanism.

Table 7--Bias and standard deviation of Nimbus-derived mean temperatures bounded by constant pressure levels with respect to radiosonde observations

LAYER (mb)	BIAS (°C)	STANDARD DEVIATION (°C)
1000-850	-2.3	3.0
850-700	-1.3	2.5
700-500	-0.9	2.5
500-400	-0.1	2.6
400-300	-0.5	2.8
300-250	-0.9	3.0
250-200	-1.0	2.6
200-150	-0.4	2.2
150-100	-0.1	1.9

The standard deviations are also larger than should be achievable with a satellite sounding system. It must be remembered, however, that the Nimbus-5 retrievals are obtained without the aid of contemporary radiosonde or forecast information so that the deviations are larger than would be achieved if contemporary data were used in the profile estimations (e.g., the way conventional data is used by NESS and GISS in the VTPR data reduction).

Figure 63 is presented in order to more clearly assess the information content of the Nimbus retrievals. Shown is the RMS deviation of the Nimbus-derived thickness of various pressure layers with respect to radiosonde measurements and the RMS deviation of the persistence forecast with respect to the radiosonde measurement. (The bias temperature error given in Table 7 was removed before computing the thickness values from the Nimbus retrievals.) The RMS errors are plotted as a function of the magnitude of the 12-hour persistence forecast error. (The previous 12-hour old radiosonde is used as the forecast.) The ordinate represents the RMS error whereas the abcissa represents a cropping of the sample into categories such that the forecast error is greater than the abcissa value. The number of cases within each sample is shown above the abcissa value. As may be seen from this figure, when the sample includes all cases (Forecast Error > 0), the RMS error of the persistence forecast thickness values is less than the RMS error of the Nimbus derived

values. This is not surprising considering the fact that RMS error of the persistence forecast (or the 12-hour variability) of the mean temperature of these layers is close to 1°C. From this statistic alone one might be tempted to draw the false conclusion that the Nimbus data is inferior to the 12-hour persistence forecast and therefore provides no information to the analysis forecast operation. However we see that for all samples in which the forecast error of layer mean temperature exceeds a value of 1°C (5, 15, 15, and 32 meters for the four pressure layers, respectively) the RMS error of the Nimbus thickness values are significantly less than RMS error of the forecast. It is encouraging to note that the Nimbus error does not increase as the atmospheric variability (persistence forecast error) increases. Consequently, the Nimbus retrievals should be quite effective in controlling errors in forecasts conducted with the May DST data sets.

Statistics, however defined, cannot tell the whole story of the value of the Nimbus data. It is frequently more informative to consider the synoptic situation and the capacity of the satellite derivations to define the salient meteorological features. To this end we have selected an orbit of 24 May which passed over a significant weather feature in the vicinity of the dense radiosonde coverage of western Europe. Figure 64 presents an analysis (based on the radiosonde data) of the thermal field at 500 mb together with some of the reported radiosonde data at that level. The satellite track with the locations of the temperature retrievals is also shown. The synoptic situation has a warm ridge pushing north over Iceland with a closed cold low centered over France. A strong thermal gradient extends over Spain and the northern Mediterranean Sea. The satellite overpass (northbound and within 1 hour of synoptic time) passes only slightly to the west of the low center and directly through the ridge over Iceland. From the radiosonde and satellite data vertical cross section analysis have been constructed and compared. The radiosonde stations numbered in figure 64 are those used to construct the radiosonde cross sections. Where more than one station has the same number the data was averaged for the cross section analysis. The averaging allows the satellite and radiosonde data to more nearly coincide, although it also somewhat smooths the radiosonde data. The cloud conditions along the orbital track are revealed in the NOAA satellite cloud picture shown in figure 65.

Figure 66 shows the temperature cross sections prepared from the radiosonde and Nimbus data. Figure 67 shows the cross sections in terms of isentropic rather than isothermal contours. The major synoptic features are very similar in both analysis. Scanning across the isentropic cross-sections from North-South we see that the isobaric gradient of potential temperature below the 400-mb level in the vicinity of a ridge at 64°N is much stronger in the Nimbus cross section than in the radiosonde cross section. However, looking at figure 64 it appears that the satellite

result is probably more correct since the radiosonde estimates results from an interpolation of data which is more than a hundred miles off the orbital track. Both cross sections reveal weak isobaric gradients of potential temperature near the center of the low-pressure system near 48°N. The double minimum at 500 mb near 45°N and 50°N, however, is more pronounced in the radiosonde case. However, the very pronounced isobaric isentropic gradients across the frontal region between 40° and 43°N south of the low pressure system is much more pronounced in the Nimbus result, but this again may be due to the fact that the radiosonde reports are some distance away from the orbital track (see figure 64). The packing of isentropes near 350 mb near the storm center revealed in the radiosonde cross section is washed out in the Nimbus case. This probably results from the inability of the satellite soundings to capture the vertical temperature structure properly in the tropopause region.

Figure 68 shows the normal component geostrophic winds (m/sec) computed from the radiosonde and Nimbus temperature cross section data via the thermal wind relationship. It can be seen that the circulation implied by the Nimbus temperature soundings is in generally good agreement with that implied by the radiosonde data, although in this situation the westerly wind component implied by the Nimbus thermal structure is greater than that obtained from the radiosonde analysis while the easterly component is slightly weaker. Examples like this reinforce our conviction that thermal profile data from satellites is of sufficient resolution and quality for resolving the important features of the atmosphere's circulation.

During the May test, the absolute errors of the Nimbus retrievals were larger than is normally achievable if radiosonde data is used to alleviate systematic calibration errors and uncertainties in the weighting functions. For the processing of Nimbus-5 data at GISS there is no provision for such a use of radiosonde data. Since relatively large bias errors of the Nimbus retrievals occurred during the May test, it is recommended that provisions be made before the next DST to have current radiosonde data available at GISS and software prepared to use these data for minimizing errors due to uncertainties in instrument calibration and atmospheric transmission function calculations.

It has become increasingly obvious that the impact of satellite retrievals on numerical forecasts depends not only on the absolute values of the retrieval errors but also on the correlation of the retrieval errors with the errors of the forecast. When forming the level III analyses from satellite data, the satellite values are combined with forecast values using weights which are based on the expected errors of the retrieval and forecast, respectively. However, the weighting procedure used during the May DST were not optimum since they were not allowed to vary in space and time as a function of varying forecast uncertainty.

If the satellite retrieval errors are independent of the forecast errors, more "optimum" weights can be defined from the regional correlation between the two sources of data. Regions where the correlation is high reflect higher forecast accuracy than in regions where the correlation is low. (Methods of defining more optimum weights which are regionally dependent are now under development at both NESS and NMC.)

The use of an optimum weighting scheme for obtaining a level III data value which would then contain the information available in both the satellite retrievals and the forecast should minimize the effects of the errors of the satellite retrievals on the analysis forecast operation. At the same time the data values derived from an optimum combination of satellite and forecast data should be more compatible with other conventional data inputs than would be the raw satellite derivations. It is therefore recommended that such an "optimum" weighting scheme for combining the Nimbus satellite retrievals with the forecast be implemented for forming the level III Global Data Sets during the next DST.

10.0 FUTURE DEVELOPMENTS

The Nimbus-6 satellite scheduled to be launched during June, 1975 will carry much improved infrared and microwave sounding radiometers. A seventeen-channel High-resolution Infra-Red Sounder (HIRS) and five channel SCanning Microwave Spectrometers (SCAMS) will measure radiation in numerous spectral channels of the 4.3-μm CO_2, 15-μm CO_2 and 60-GHz O_2 bands to enable improved vertical temperature resolution. Also four spectral channels, two infrared and two microwave will permit the specification of the vertical profile of water vapor mixing ratio as well as the total precipitable water content. Unlike the Nimbus-5 sensors, the Nimbus-6 sounders will scan contiguously from horizon to horizon enabling complete global coverage to be achieved every twelve hours.

For the processing of the Nimbus-6 data, improved algorithms have been developed to make more accurate specifications from the amalgamated infrared and microwave sounding data. As a result of the improved instrumentation and data reduction procedures, one can expect results from Nimbus-6 which are much superior to those obtained from Nimbus-5 and described in this report.

REFERENCES

Bonner, William D. (National Meteorological Center, National Weather Service, U.S. Department of Commerce, Washington, D.C.), "An Analysis Procedure Constructed by Updating a Forecast with Satellite Soundings," 1974 (unpublished memorandum).

Fleming, H.E., and Smith, W.L., "Inversion Techniques for Remote Sensing of Atmospheric Temperature Profiles," Temperature, Its Measurement and Control in Science and Industry, Vol. 4, Part 3, Instrument Society of America, Pittsburgh, Pa., April 1972, pp. 2239-2250.

GARP, 1973: The Air-Mass Transformation Experiment. GARP Publication Series, No. 13, ICSU/WMO, Geneva, Switzerland, 54 pp.

Houghton, J.T. and Smith, S.D., The Nimbus 5 User's Guide, Goddard Space Flight Center, Greenbelt, Maryland, 1972, pp. 131-139.

McMillin, L.M., Wark, D.Q., Siomkajlo, J.M., Abel, P.G., Werbowetzki, A., Lauritson, L., Pritchard, J.A., Crosby, D.S., Woolf, H.M., Luebbe, R.C., Weinreb, M.P., Fleming, H.E., Bittner, F.E., and Hayden, C.M., "Satellite Infrared Soundings from NOAA Spacecraft," NOAA Technical Report NESS 65, National Environmental Satellite Service, National Oceanic and Atmospheric Administration, U.S. Department of Commerce, Washington, D.C., Sept. 1973, 108 pp.

Smith, W.L., Howell, H.B., Fischer, J.C., Chalfant, M.C., and Hilleary, D.T., The Nimbus 5 User's Guide, Goddard Space Flight Center, Greenbelt, Md., 1972, pp. 107-130.

Smith, W.L., Woolf, H.M., Abel, P.G., Hayden, C.M., Chalfant, M., and Grody, N., "Nimbus-5 Sounder Data Processing System; Part I: Measurement Characteristics and Data Reduction Procedures," NOAA Technical Memorandum NESS 57, National Environmental Satellite Service, National Oceanic and Atmospheric Administration, U.S. Department of Commerce, Washington, D.C., June 1974, 99 pp.

Staelin, D.H., Barath, F.T., Blinn, J.C. III, and Johnston, E.J., The Nimbus 5 User's Guide, Goddard Space Flight Center, Greenbelt, Maryland, 1972, pp. 141-157.

Togstad, William E., and Horn, Lyle H., "An Application of the Satellite Indirect Sounding Technique in Describing the Hyperbaroclinic Zone of a Jet Streak," Journal of Applied Meteorology, Vol. 13, No. 2, March 1974, pp. 264-276.

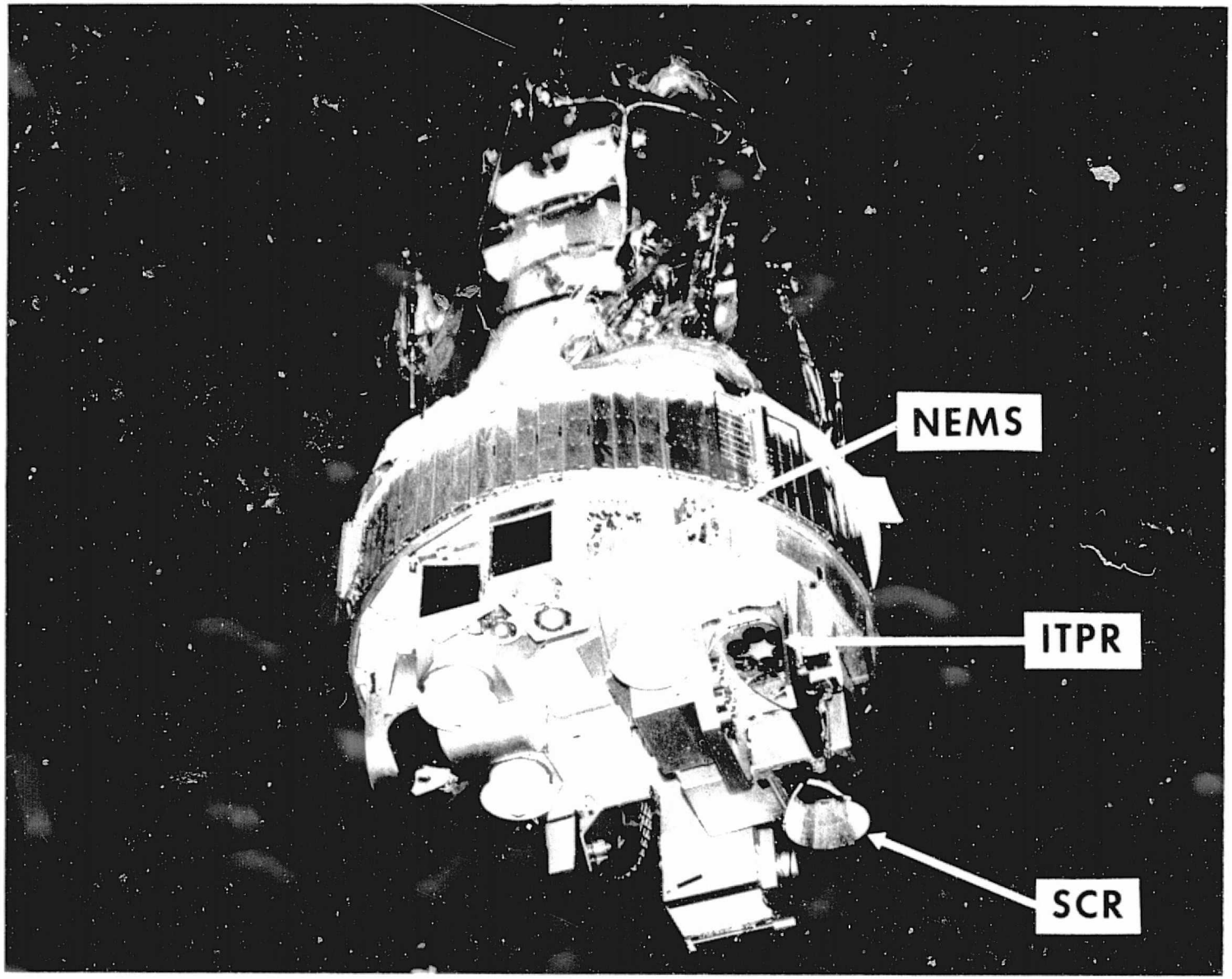

Figure 1--Photograph of the Nimbus 5 spacecraft showing the ITPR, NEMS and SCR instruments.

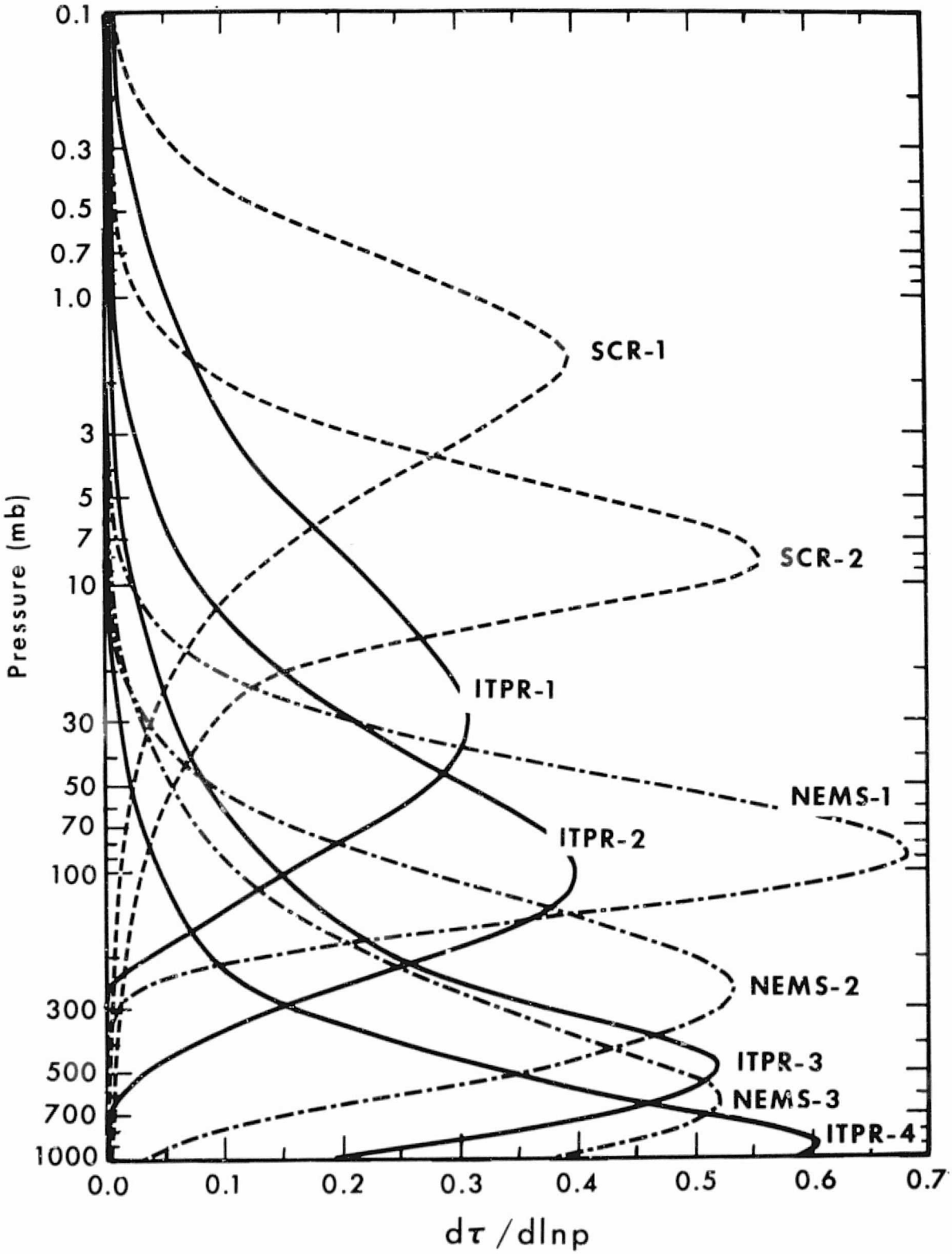

Figure 2--Atmospheric weighting functions for ITPR, NEMS and SCR spectral channels. Derivative of transmittance with respect to the logarithm of pressu

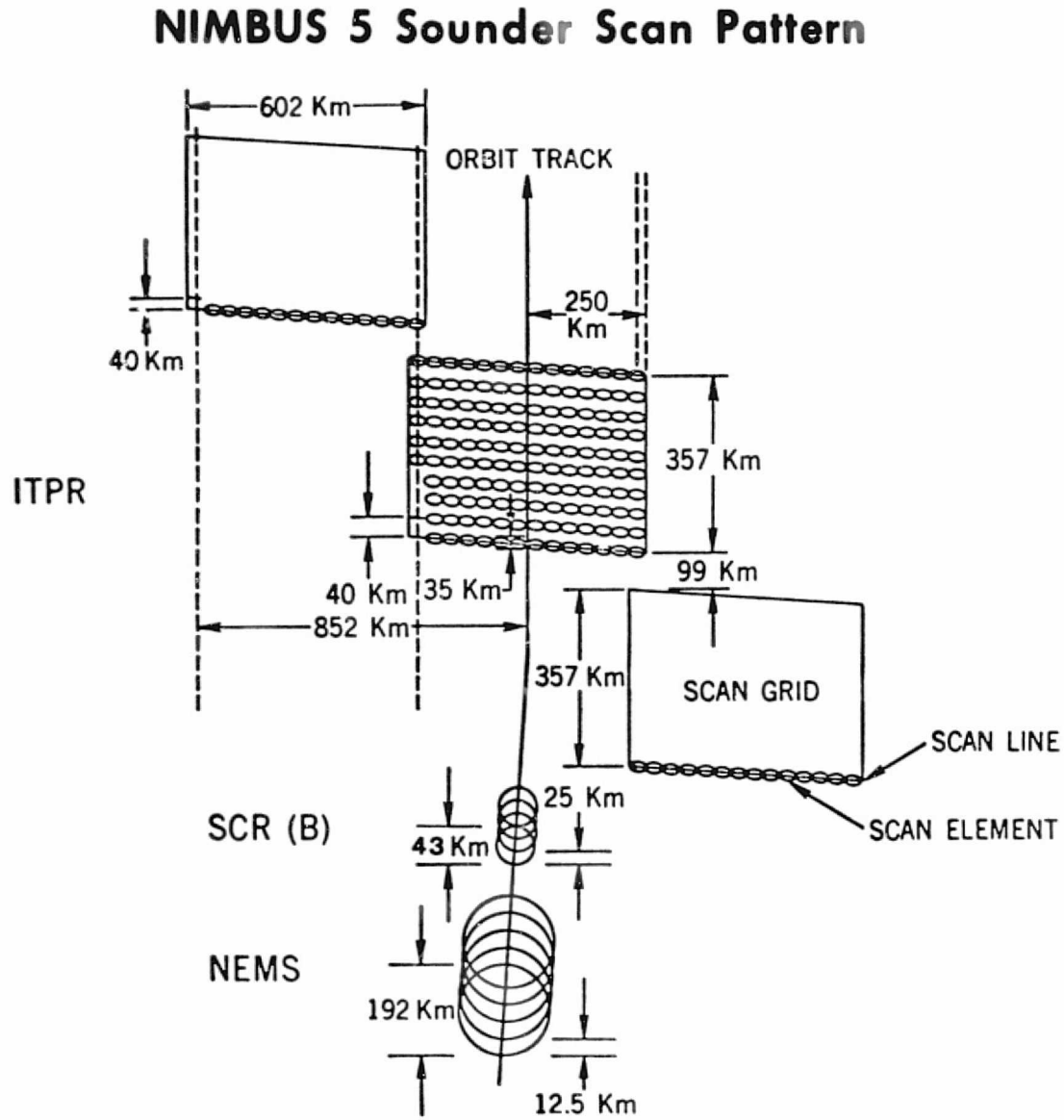

Figure 3--The earth fields of view for the ITPR, NEMS and SCR instruments.

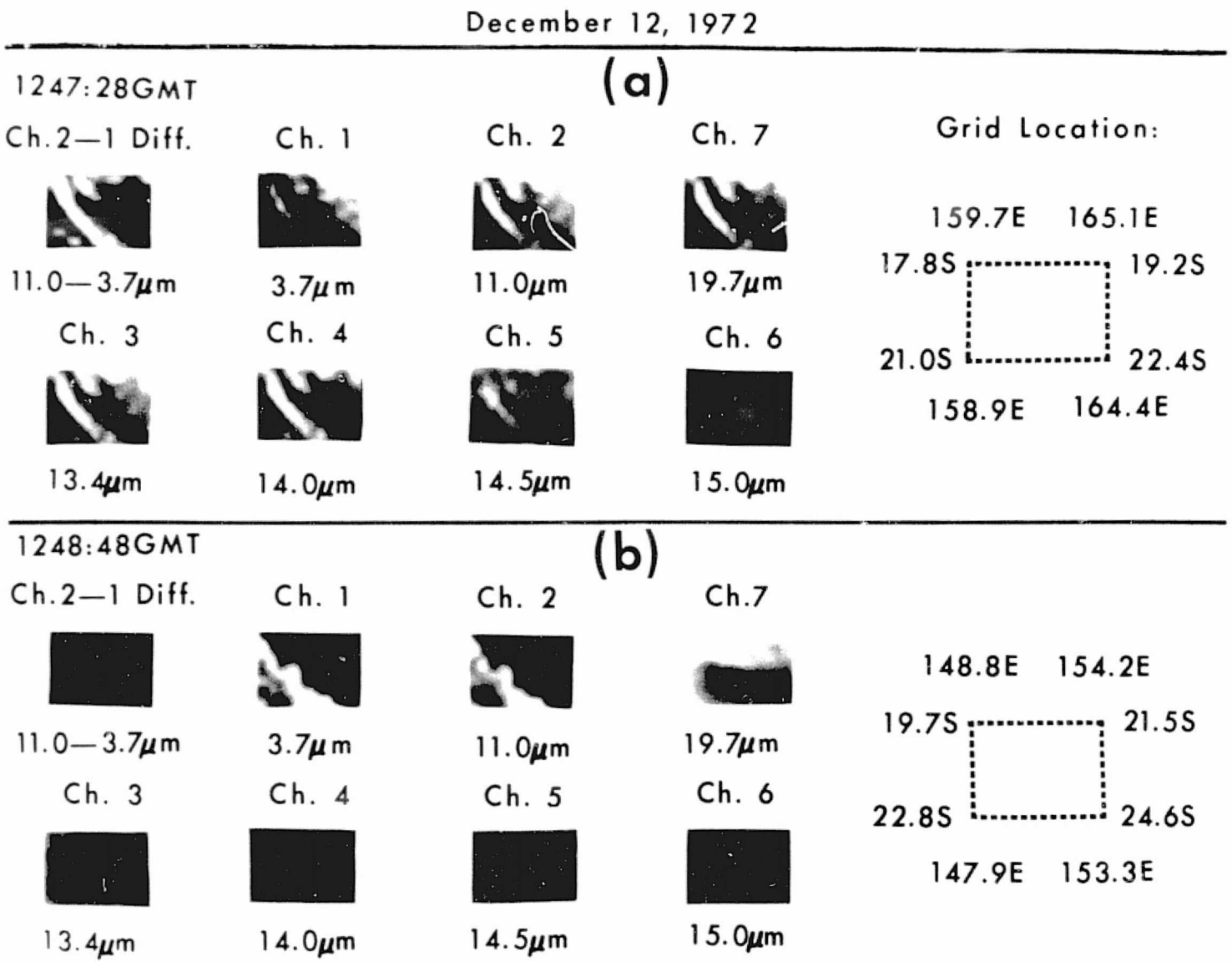

Figure 4--Images derived from ITPR window, water vapor, and CO_2 channel brightness temperature data for a geographical grid over the South Pacific Ocean (a) and over the Northeast Coast of Australia (b) on December 12, 1972.

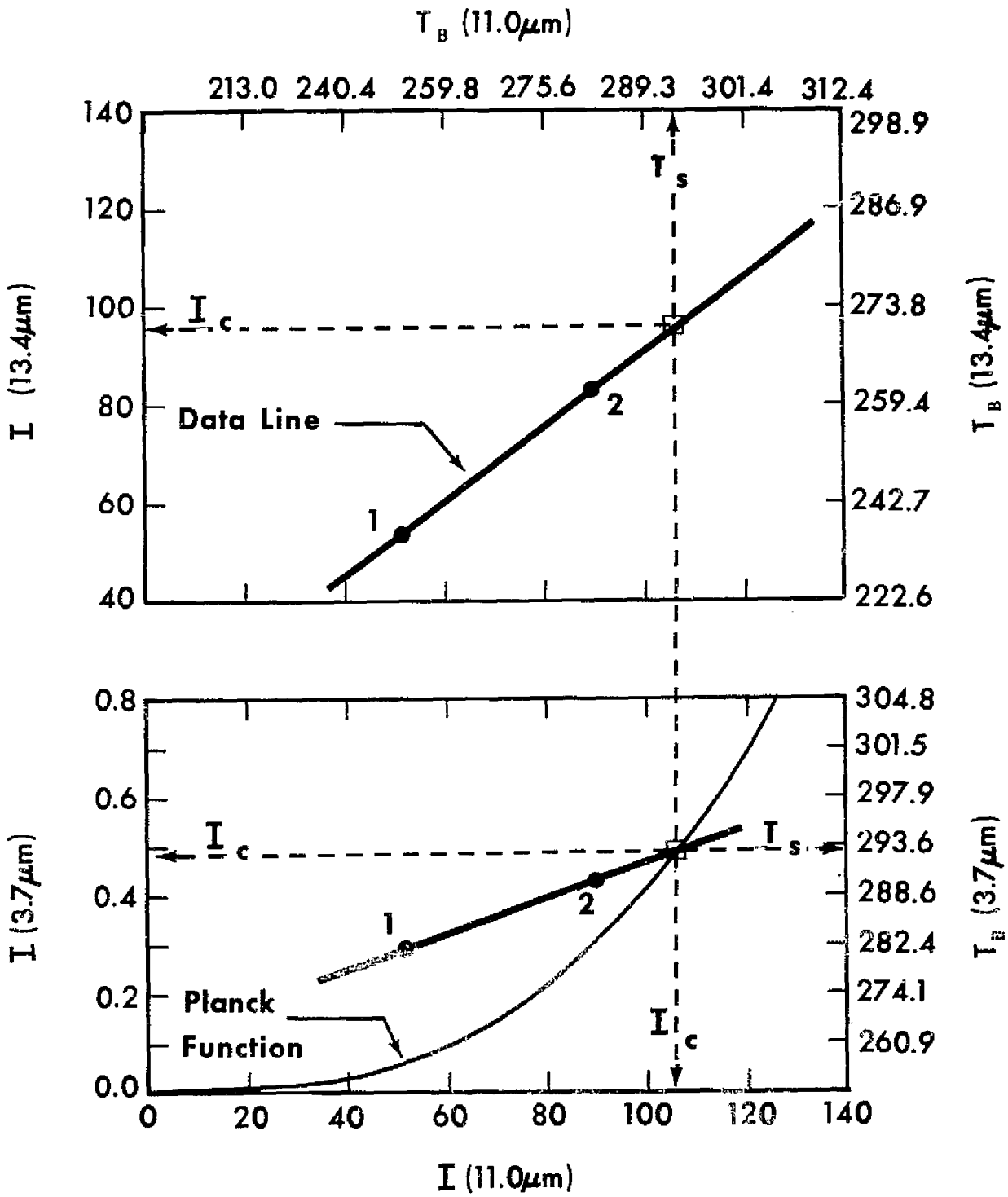

Figure 5--Plot of ITPR 3.7-μm, 11-μm and 13.4-μm radiance observations in a partly cloudy atmosphere. Also shown is the Planck Function which relates the 3.7-μm to the 11-μm radiances for an opaque and uniform surface.

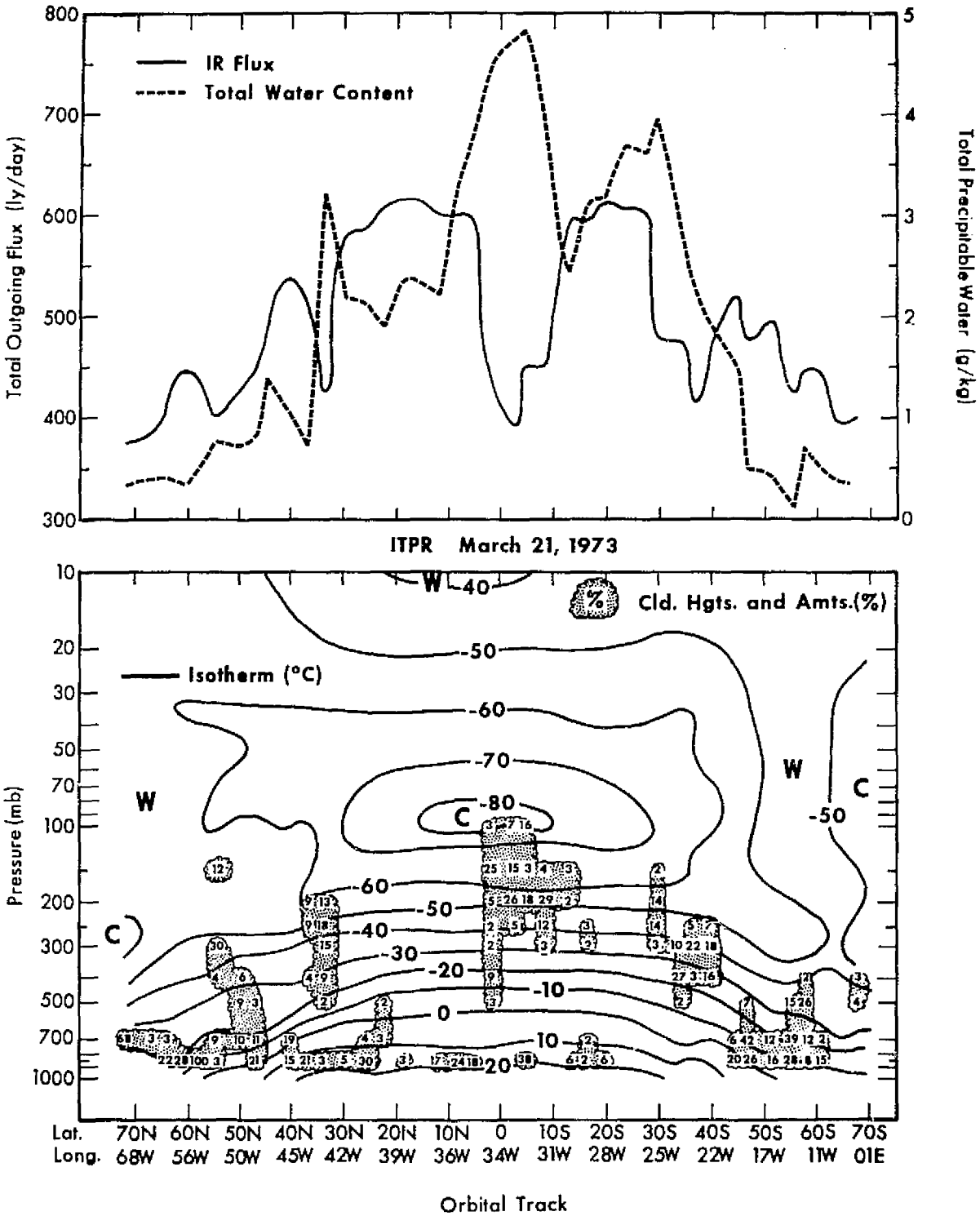

Figure 6--Vertical cross-section of the atmospheric temperature distribution, cloud heights and amounts, total outgoing long wave flux, and vertically integrated water vapor content, deduced from ITPR radiance data along an orbital track on March 21, 1973.

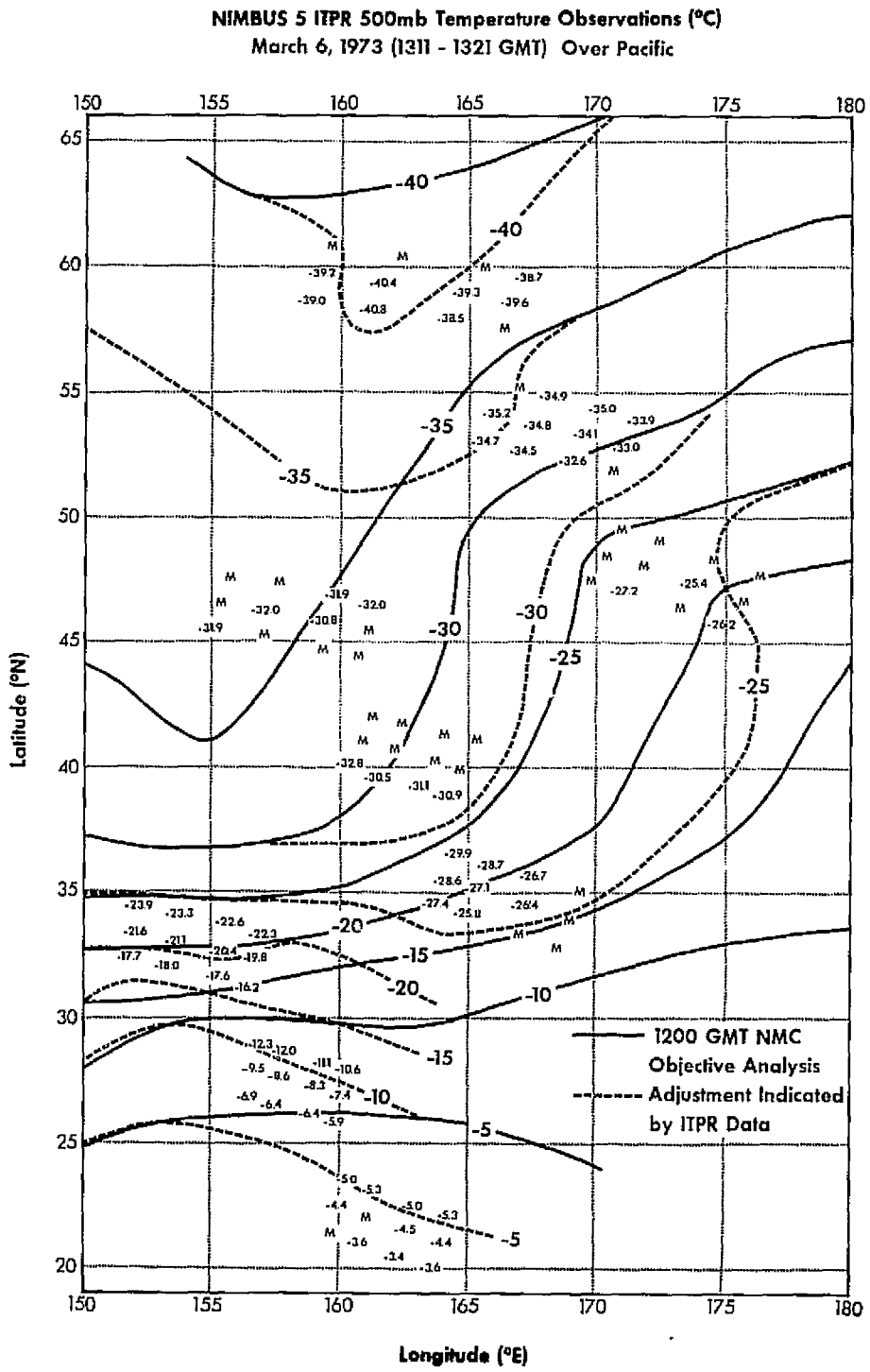

Figure 7--ITPR derived 500-mb temperatures (12 per grid unless missing) and analyses over a North Pacific low pressure system on March 6, 1973. The solid lines are the 1200 GMT NMC objective analysis and the dashed lines denote the adjustment required to fit the ITPR data.

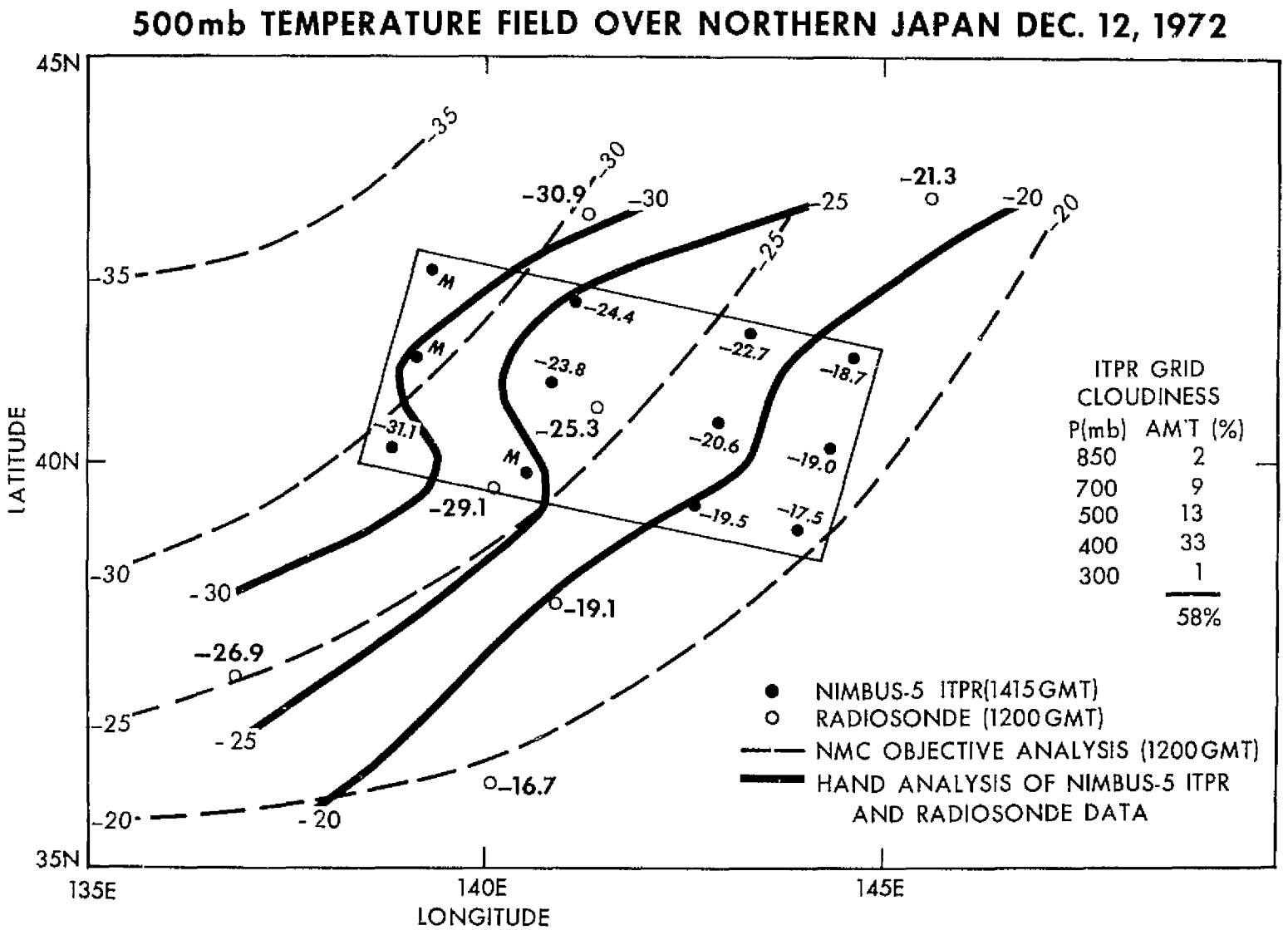

Figure 8--ITPR-derived 500-mb temperatures (solid circle) and radiosonde data (open circle) over Northern Japan on December 12, 1972. The dashed lines are the 1200 GMT NMC objective analysis and the solid lines are an analysis of the ITPR and radiosonde data.

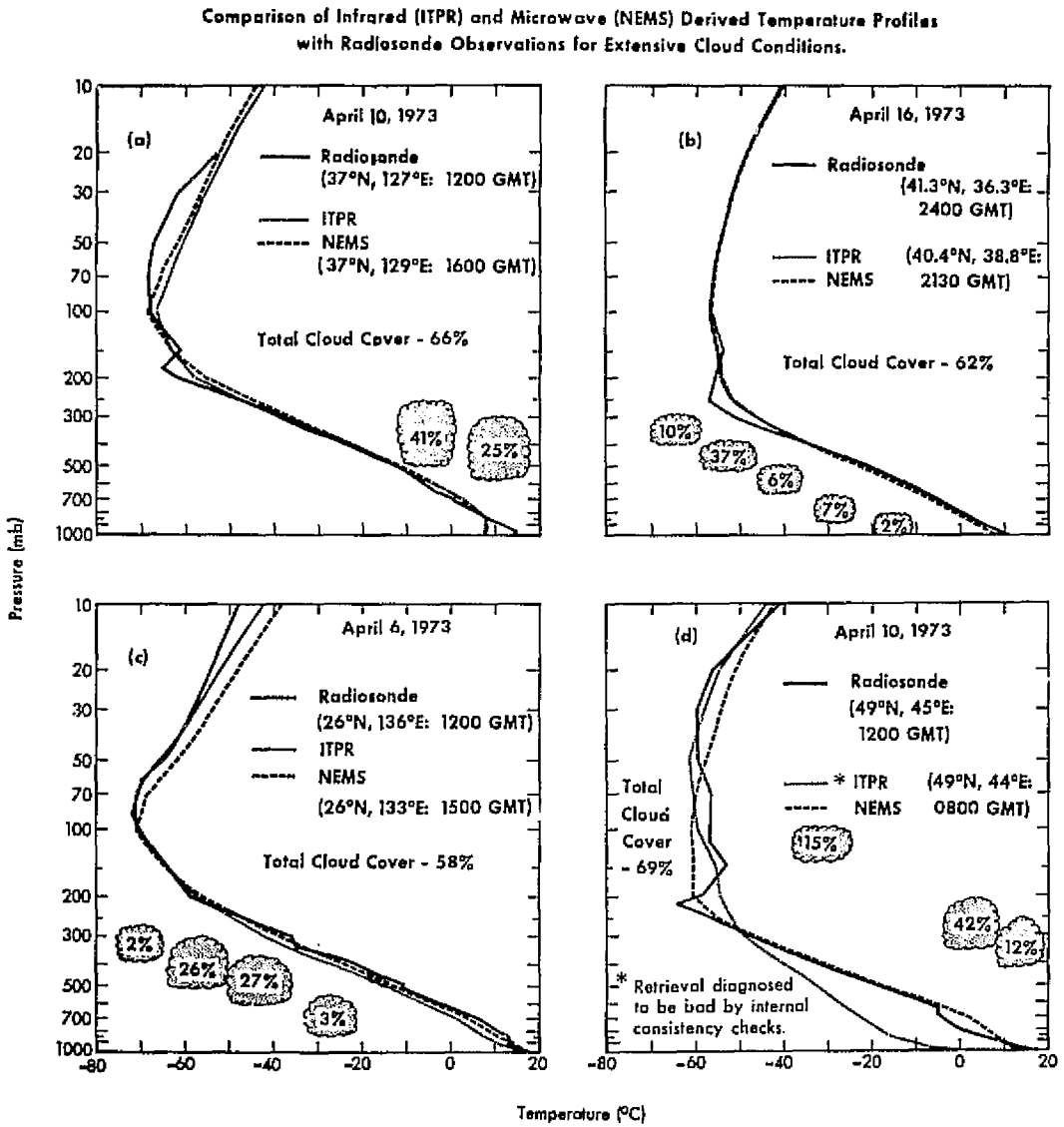

Figure 9--Comparison between Nimbus-5 temperature soundings derived from NEMS (microwave) and ITPR (infrared) observations with conventional radiosonde observations during April 1973.

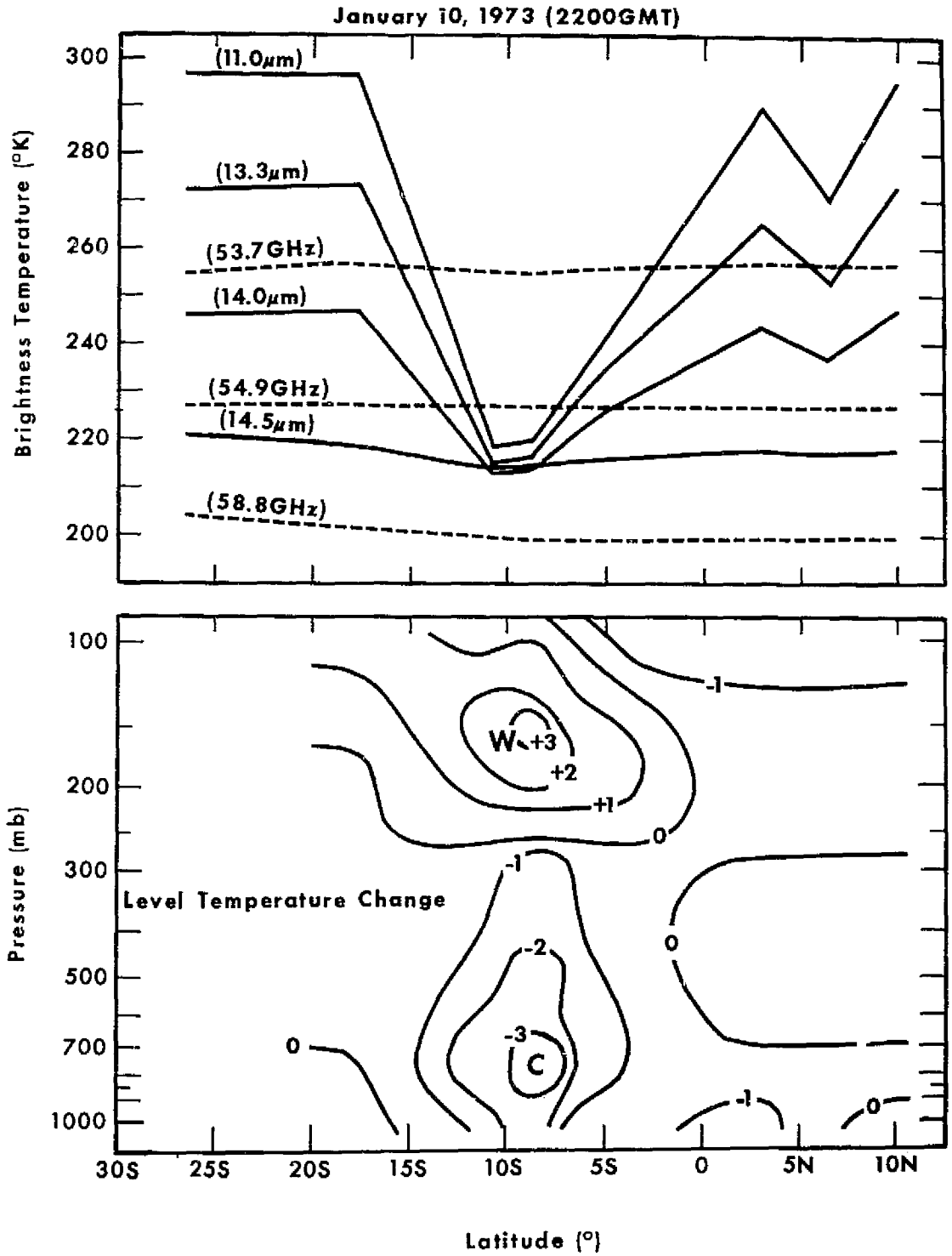

Figure 10--Brightness temperatures observed by NEMS (Microwave) and ITPR (infrared) channels over a tropical storm in the South Pacific on January 10, 1973. (top) Level mean difference between temperatures within the storm and those outside the storm's boundary. (bottom)

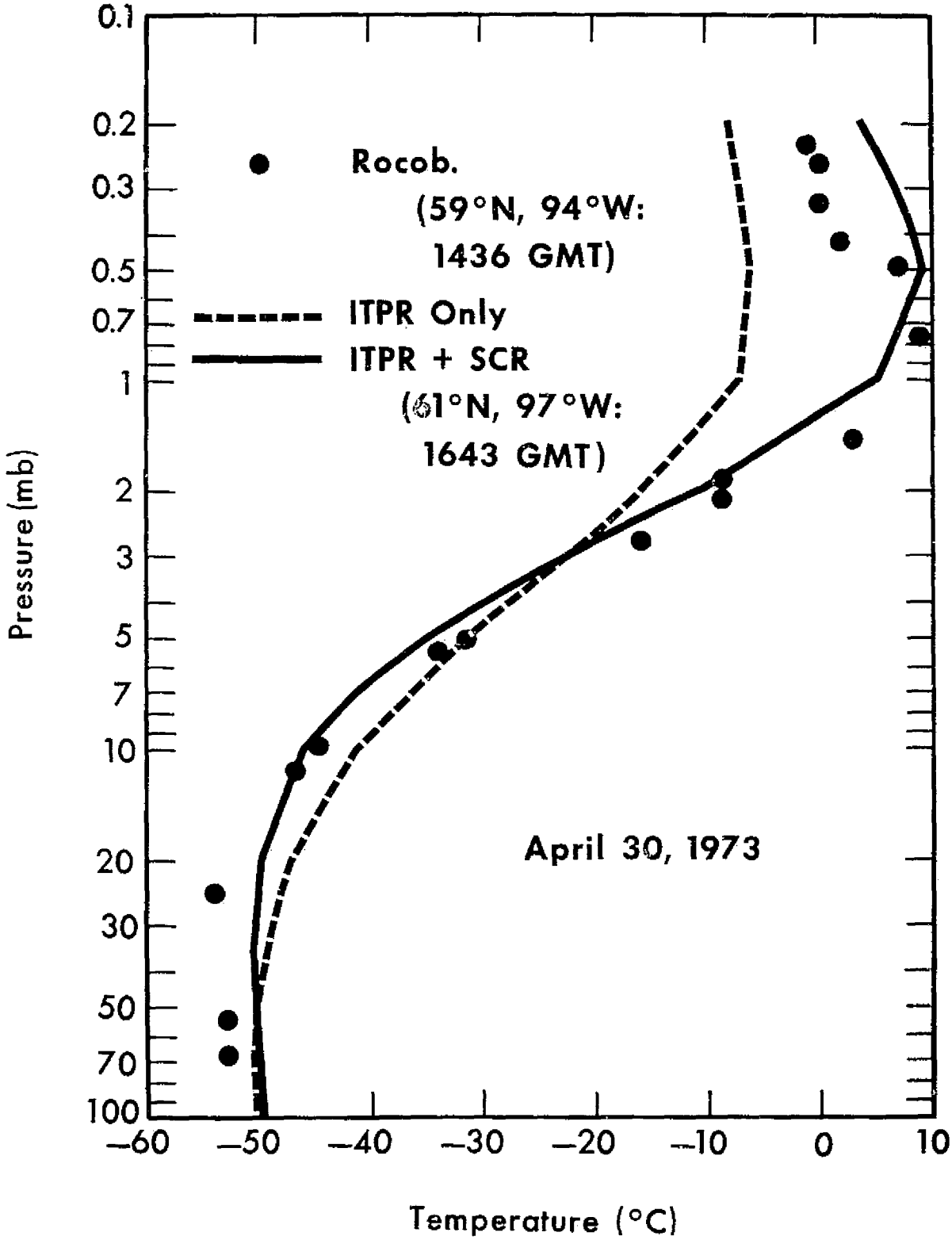

Figure 11--Comparison between derived temperature profiles from ITPR data alone and combined with SCR radiance data. The Ft. Churchill, Canada, rocketsonde observation is given to verify the profiles.

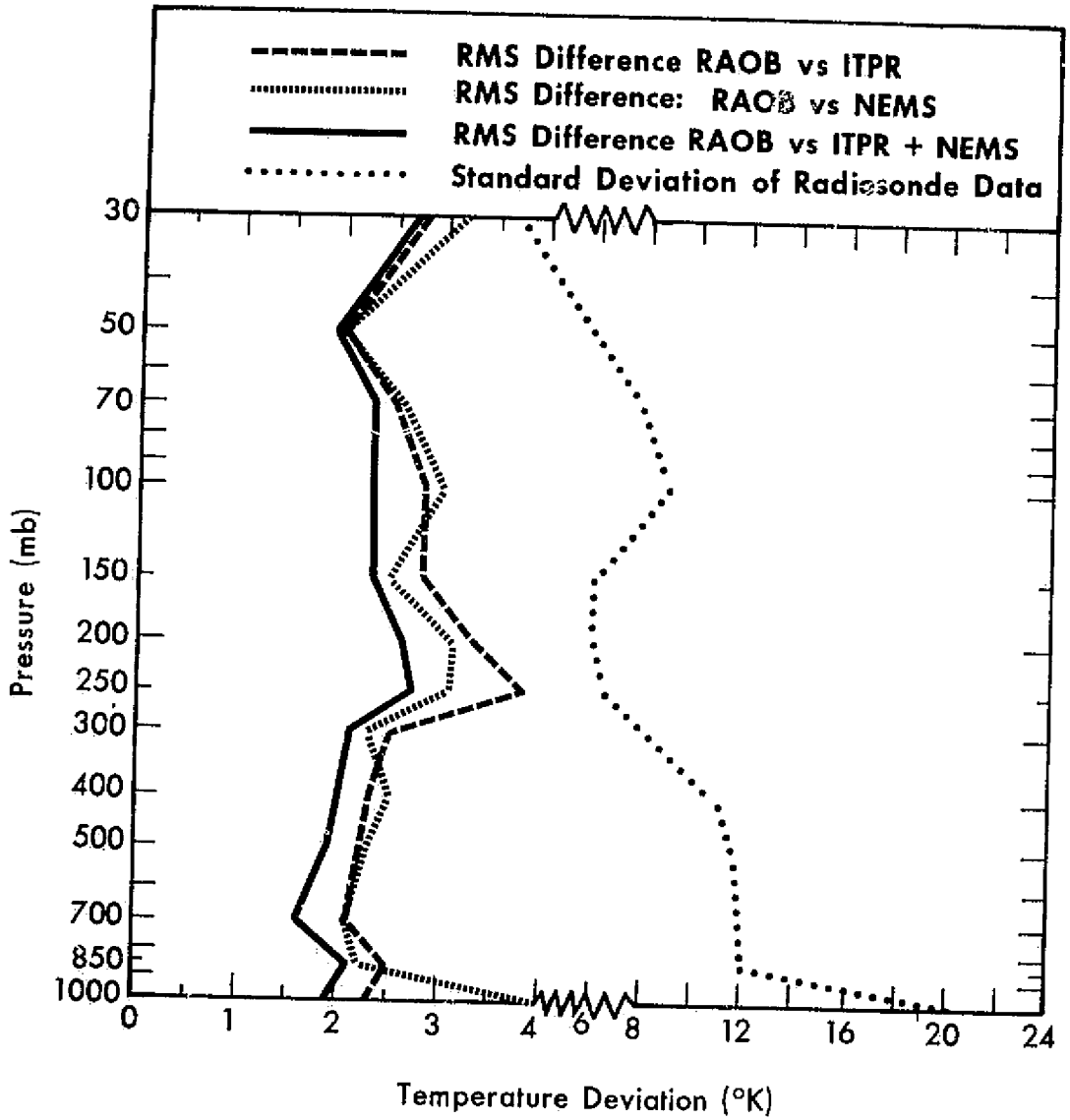

Figure 12--Standard deviations between radiosonde and radiance specified temperatures (ITPR alone, NEMS alone, and IRPR and NEMS combined.)

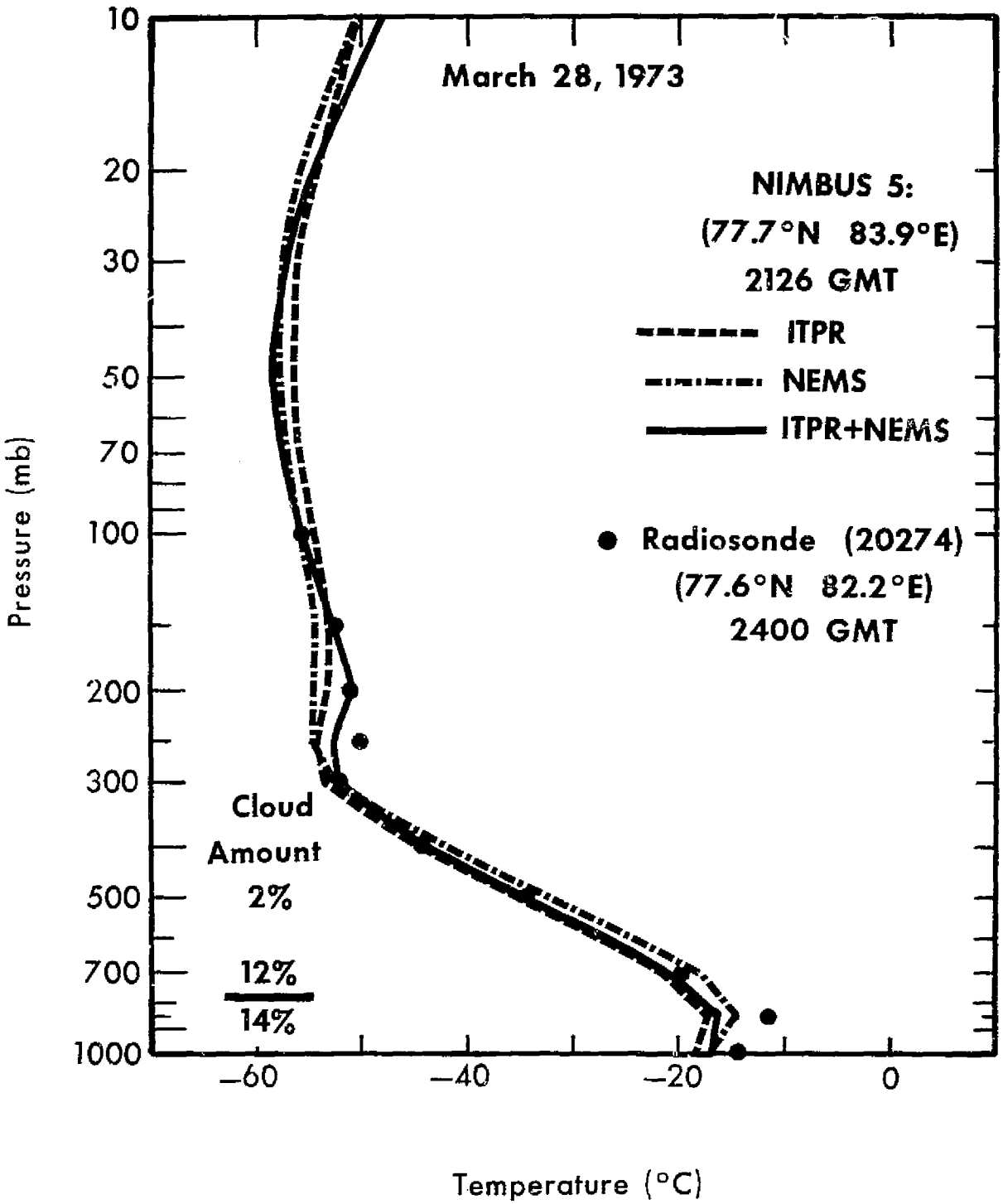

Figure 13--Comparison between temperature profiles derived from ITPR data alone, NEMS data alone, and ITPR and NEMS data combined. A conventional radiosonde observation is given to verify the results.

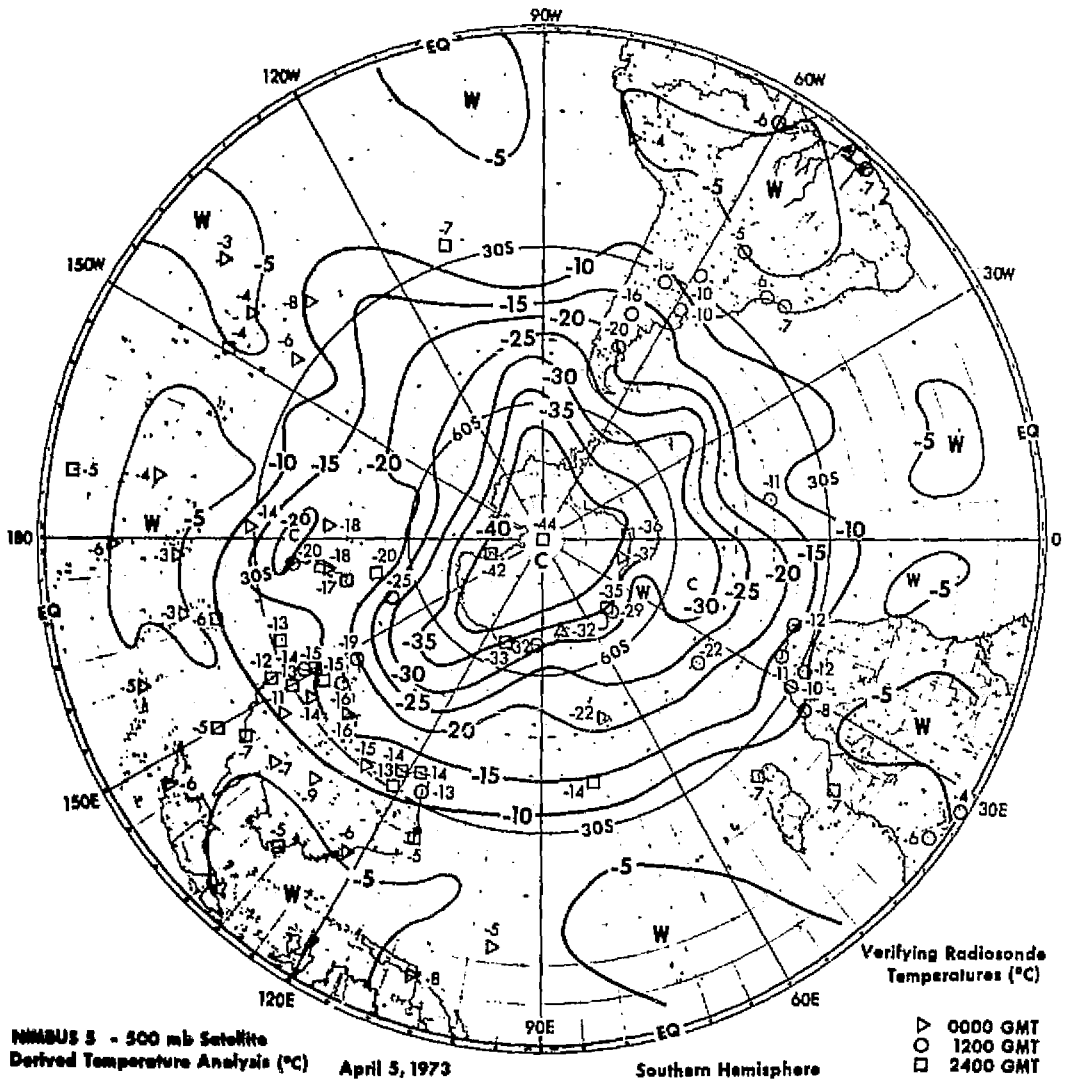

Figure 14--Southern Hemisphere 500-mb temperature analysis based solely on Nimbus-5 radiance data on April 5, 1973. Available radiosonde observations are shown to verify the Nimbus-5 data. ▷,0000GMT; ○,1200GMT; □,2400GMT.

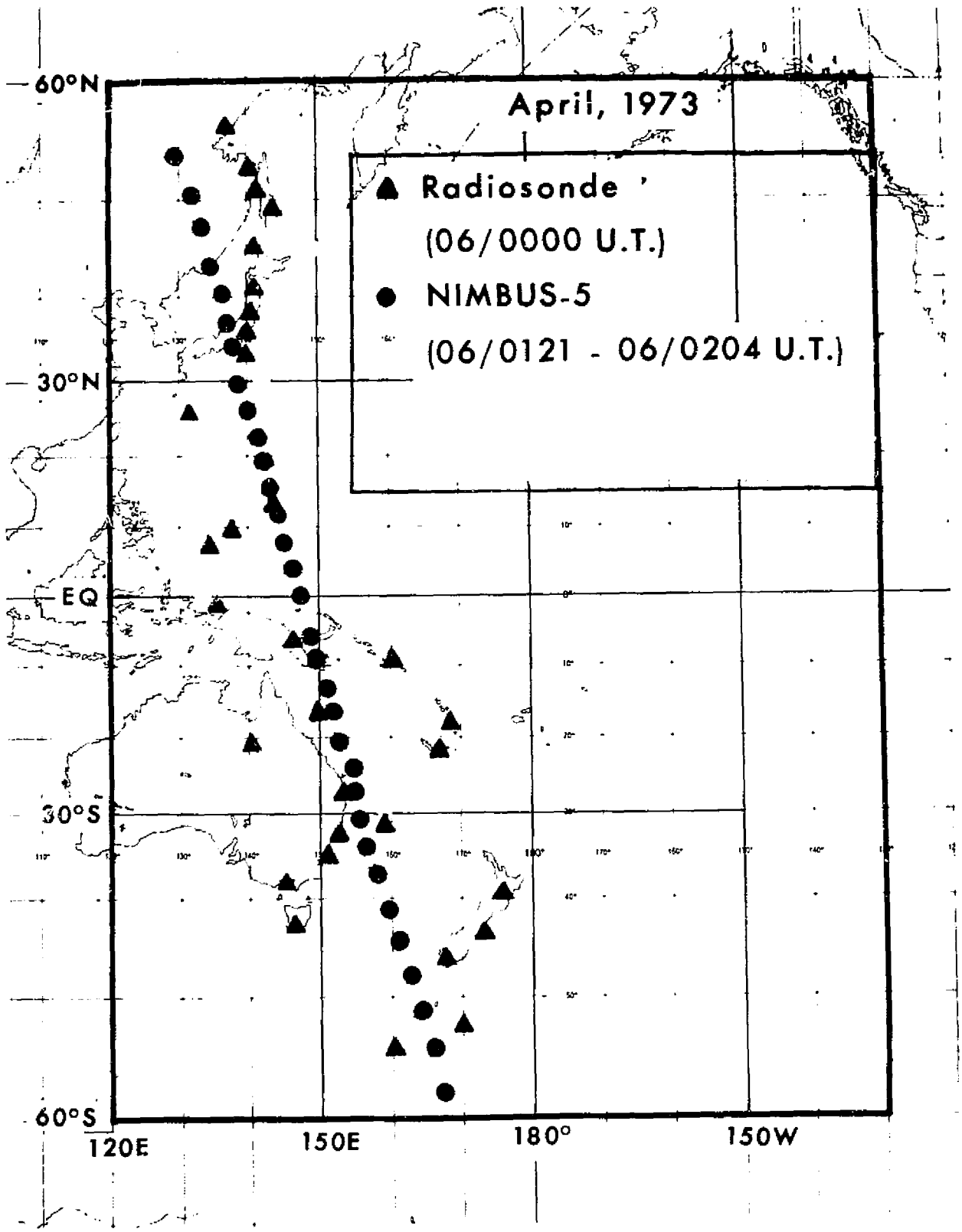

Figure 15--Geographical locations of radiosonde, Nimbus-5, and NOAA VTPR soundings. UT, Universal Time, is equivalent to GMT, Greenwich Meridian Time.

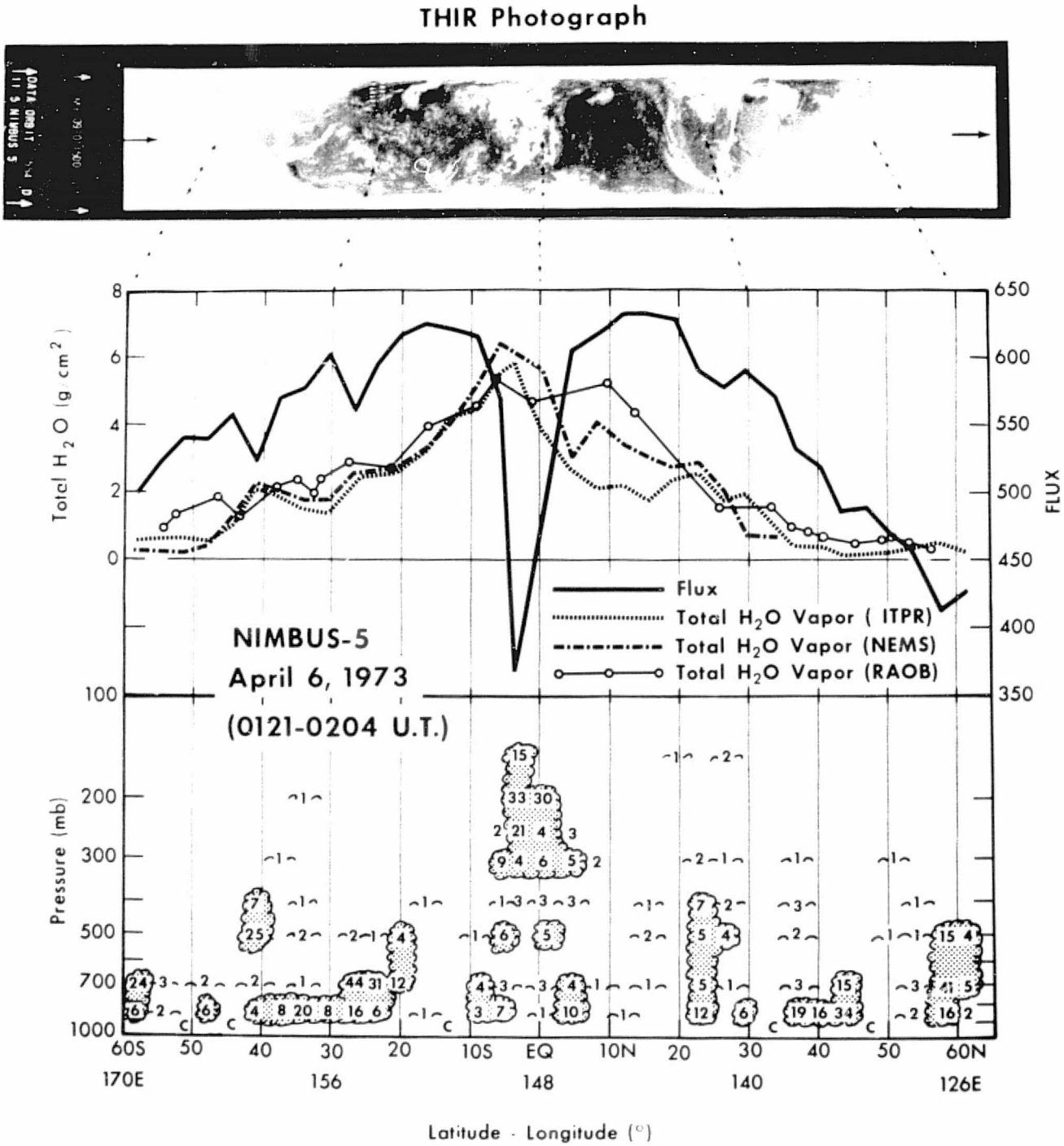

Figure 16--Latitude cross-section of total integrated water vapor (g/cm^2) total outgoing longwave flux (langleys/day), amount (%) of cloudiness reaching various pressure levels (derived from the Nimbus-5 radiance measurements). The cloud image obtained from the Nimbus-5 Temperature Humidity Infrared Radiometer (THIR) appears at the top. NEMS represents Nimbus-E Microwave Spectrometer, and RAOB represents Radiosonde Observation.

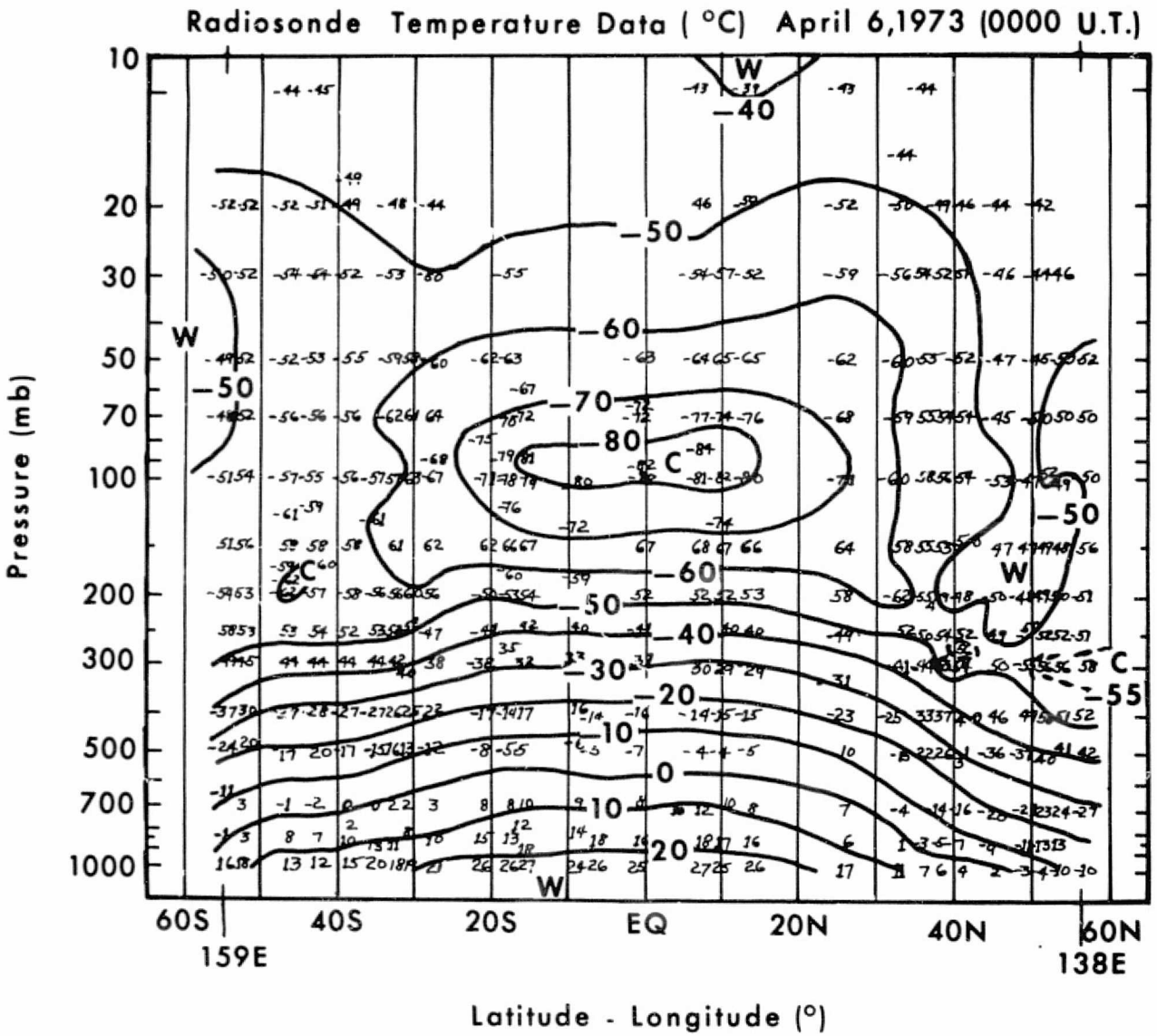

Figure 17--Vertical cross-section of radiosonde temperature observations (°C) on April 6, 1973 at 0000 GMT.

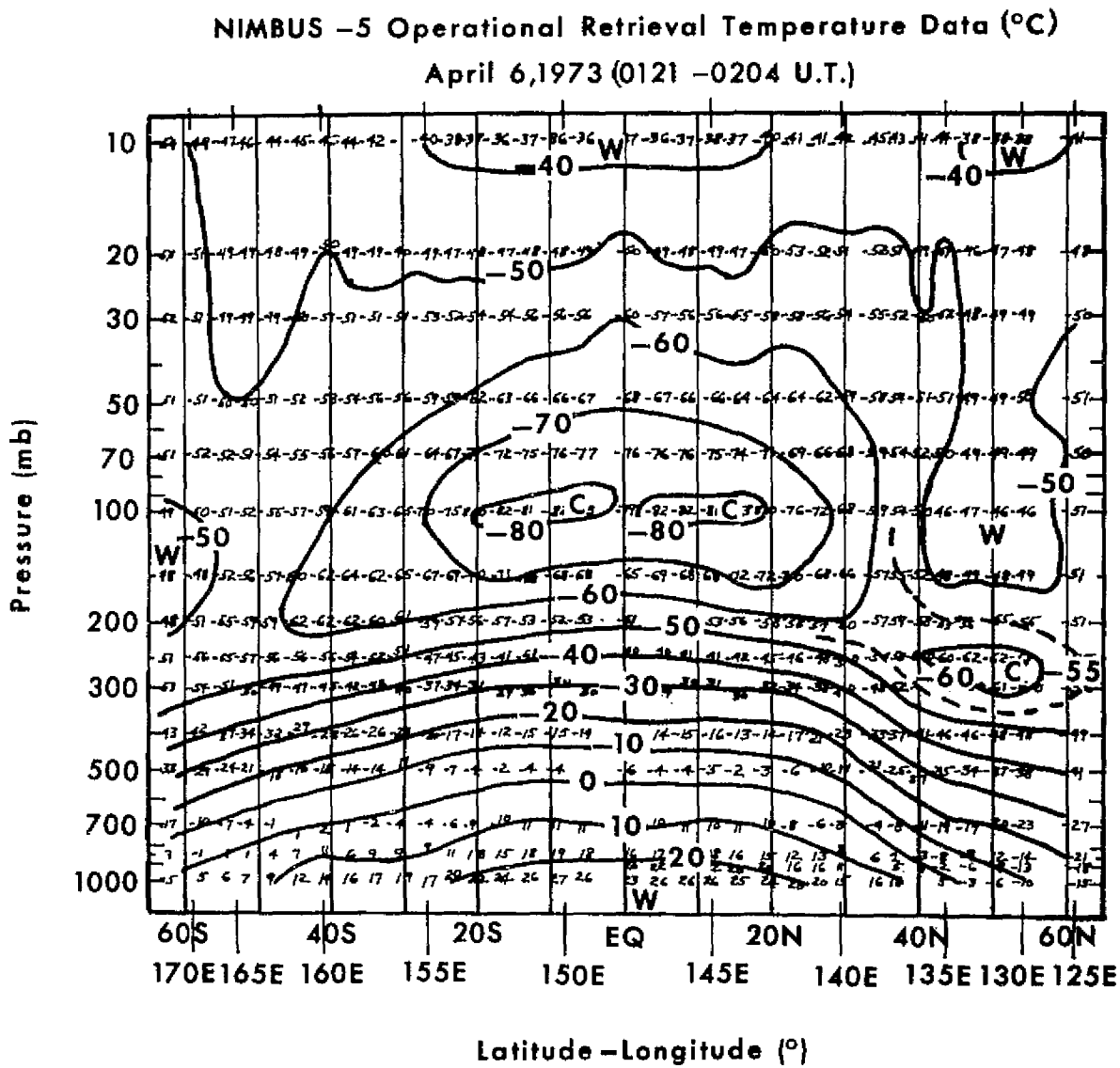

Figure 18--Vertical cross-section of Nimbus-5 temperature observations (°C) on April 6, 1973, at 0121 to 0204 GMT.

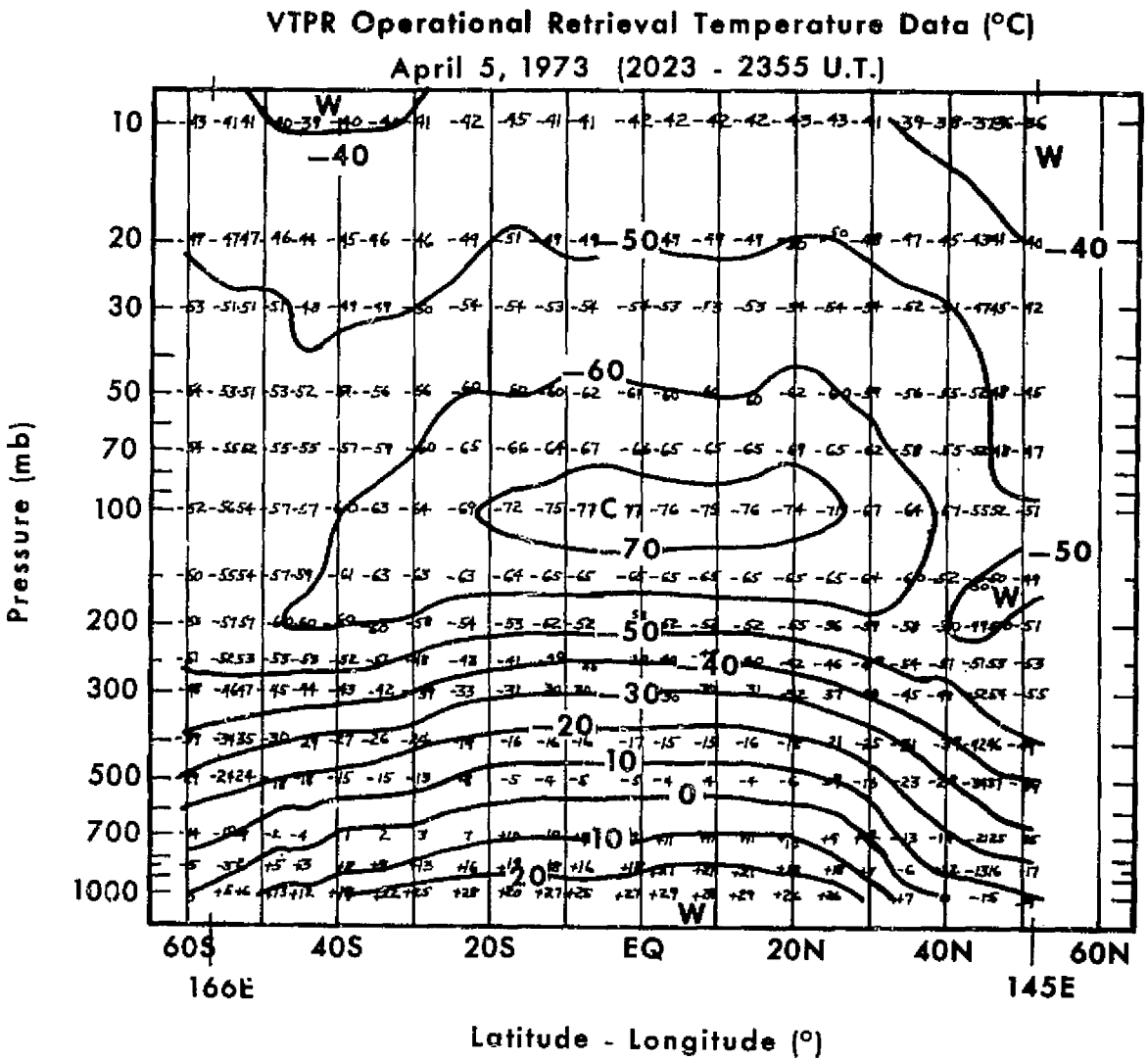

Figure 19--Vertical cross-section of NOAA-2 VTPR temperature observations on April 5, 1973, at 2023 to 2355 GMT.

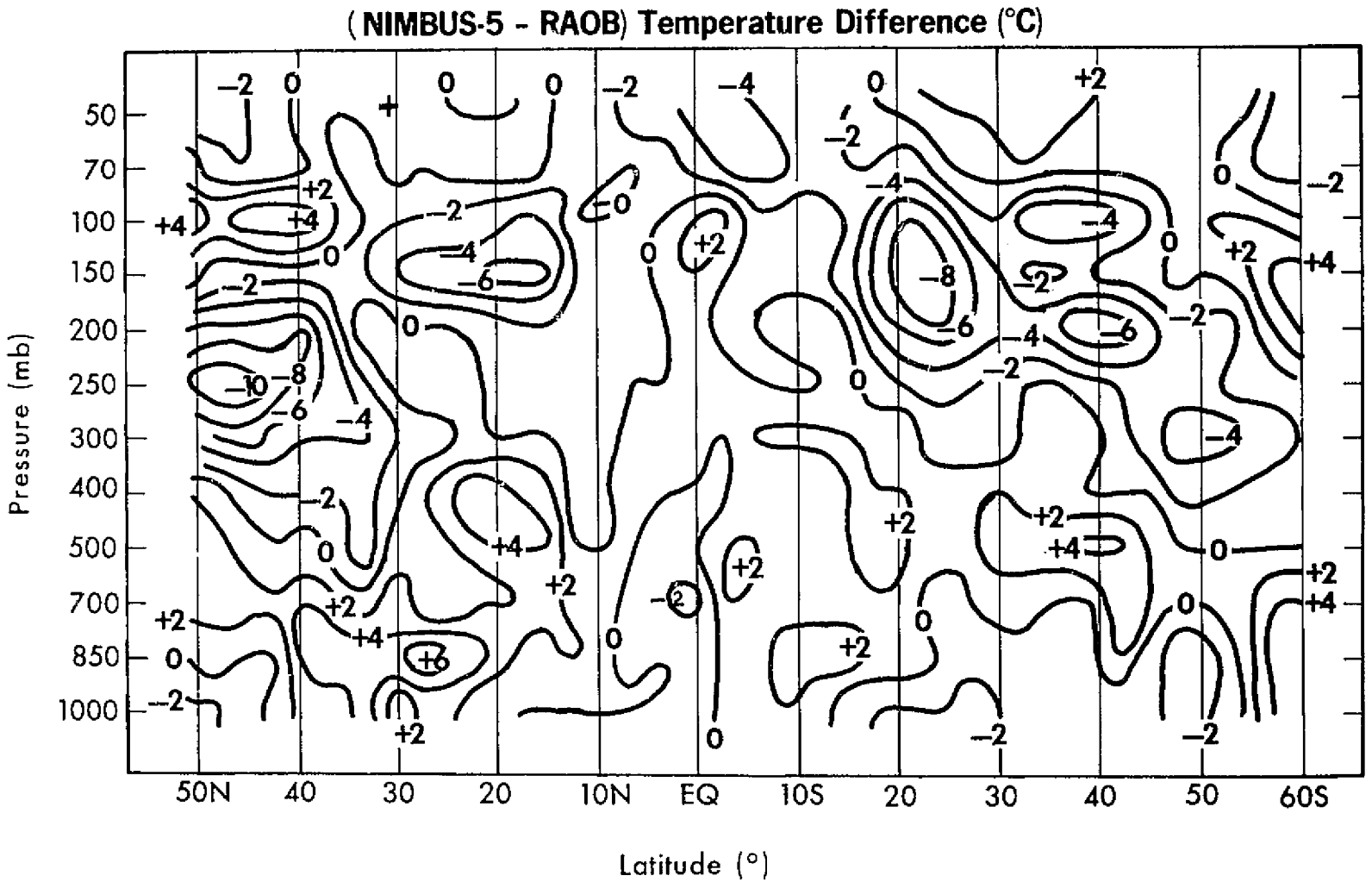

Figure 20--Difference (°C) between the Nimbus-5 and radiosonde temperature cross section analyses.

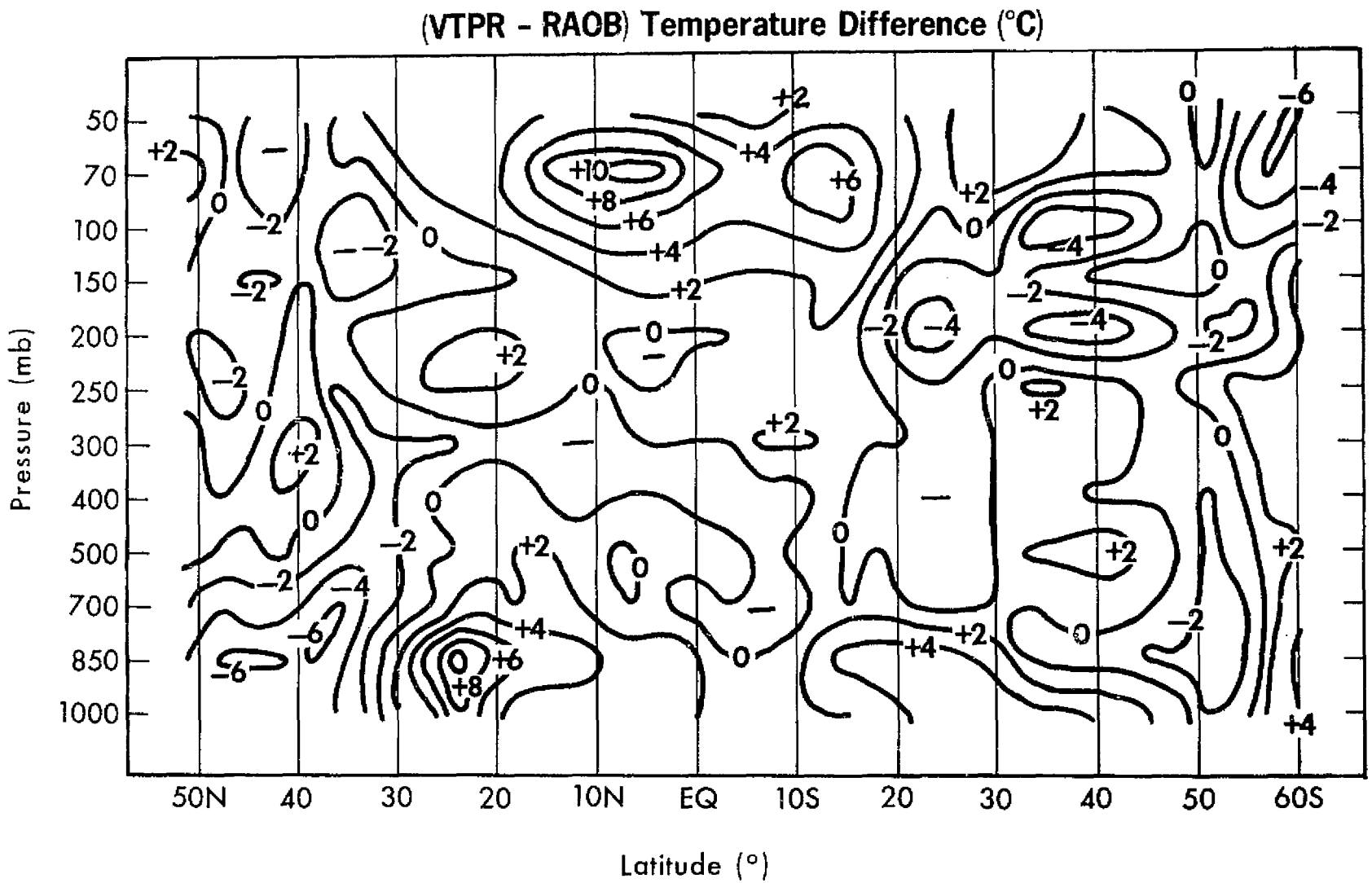

Figure 21--Difference (°C) between the VTPR and radiosonde temperature cross-section analyses.

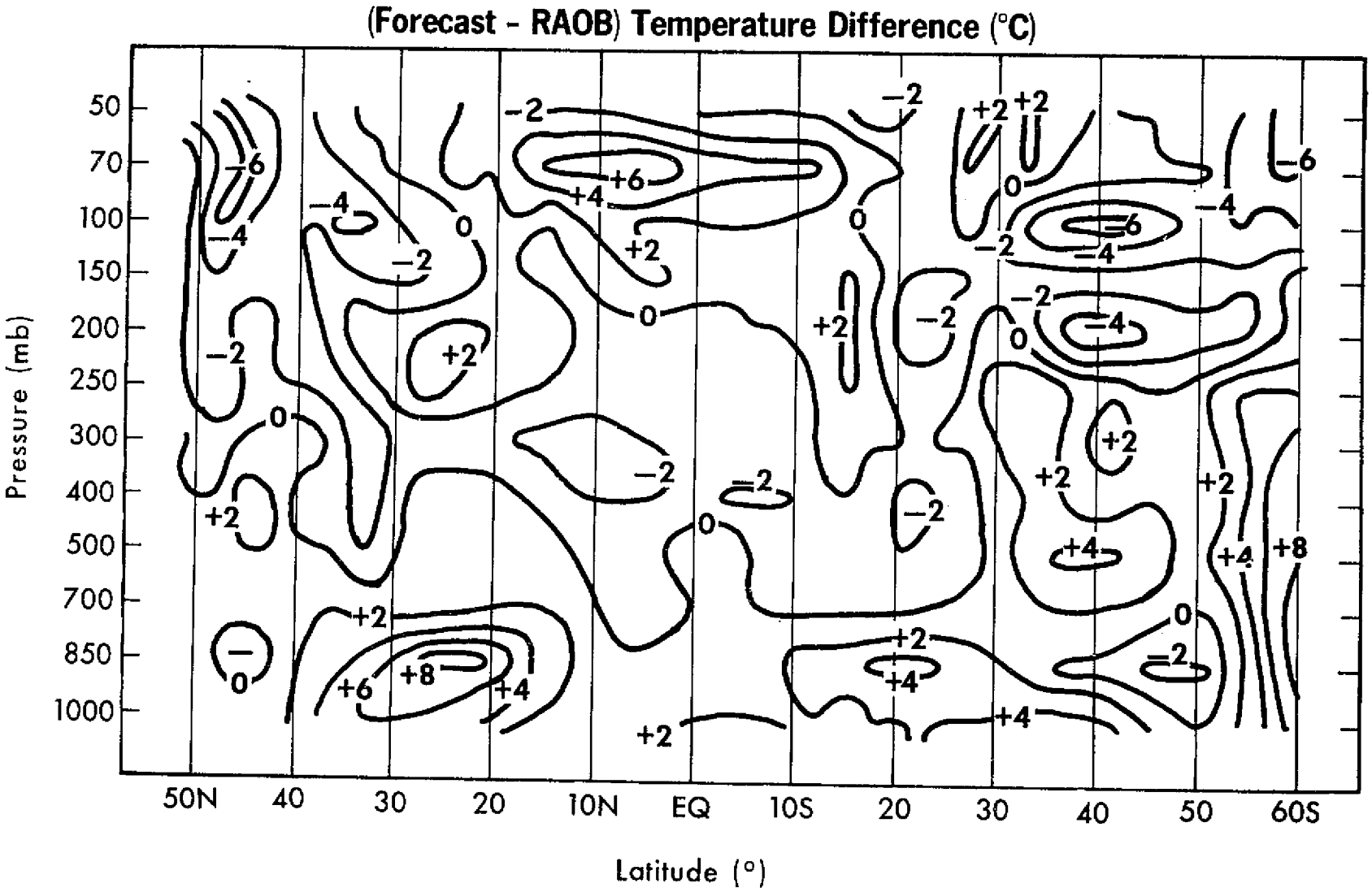

Figure 22--Difference (°C) between the 12-hour forecast and radiosonde temperature cross-section analyses.

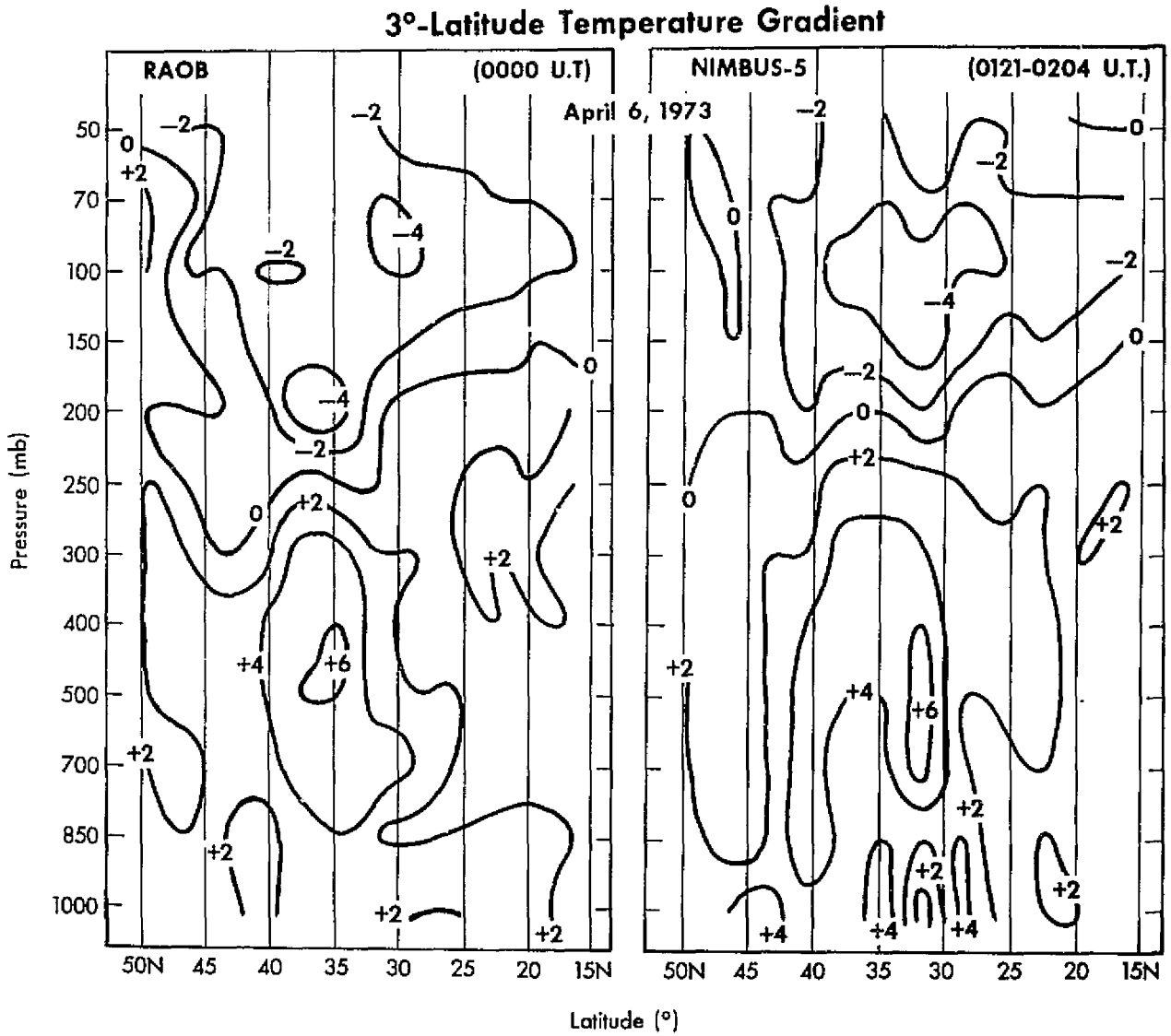

Figure 23--Radiosonde and Nimbus-5 temperature gradients over 3° latitude obtained from the cross-section analyses.

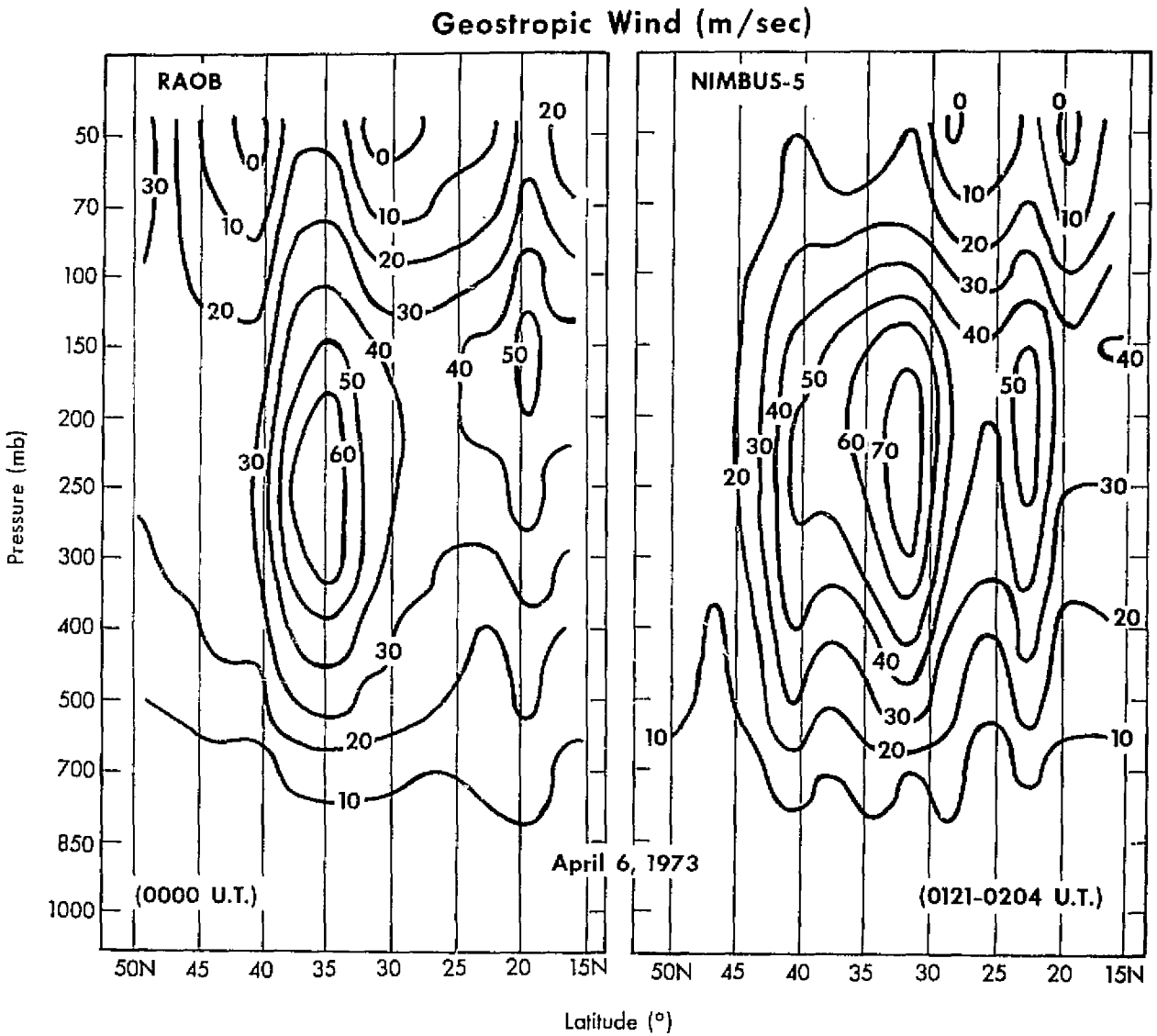

Figure 24--Geostrophic (integrated thermal) winds (m/s) computed from the radiosonde and Nimbus-5 temperature cross-sections.

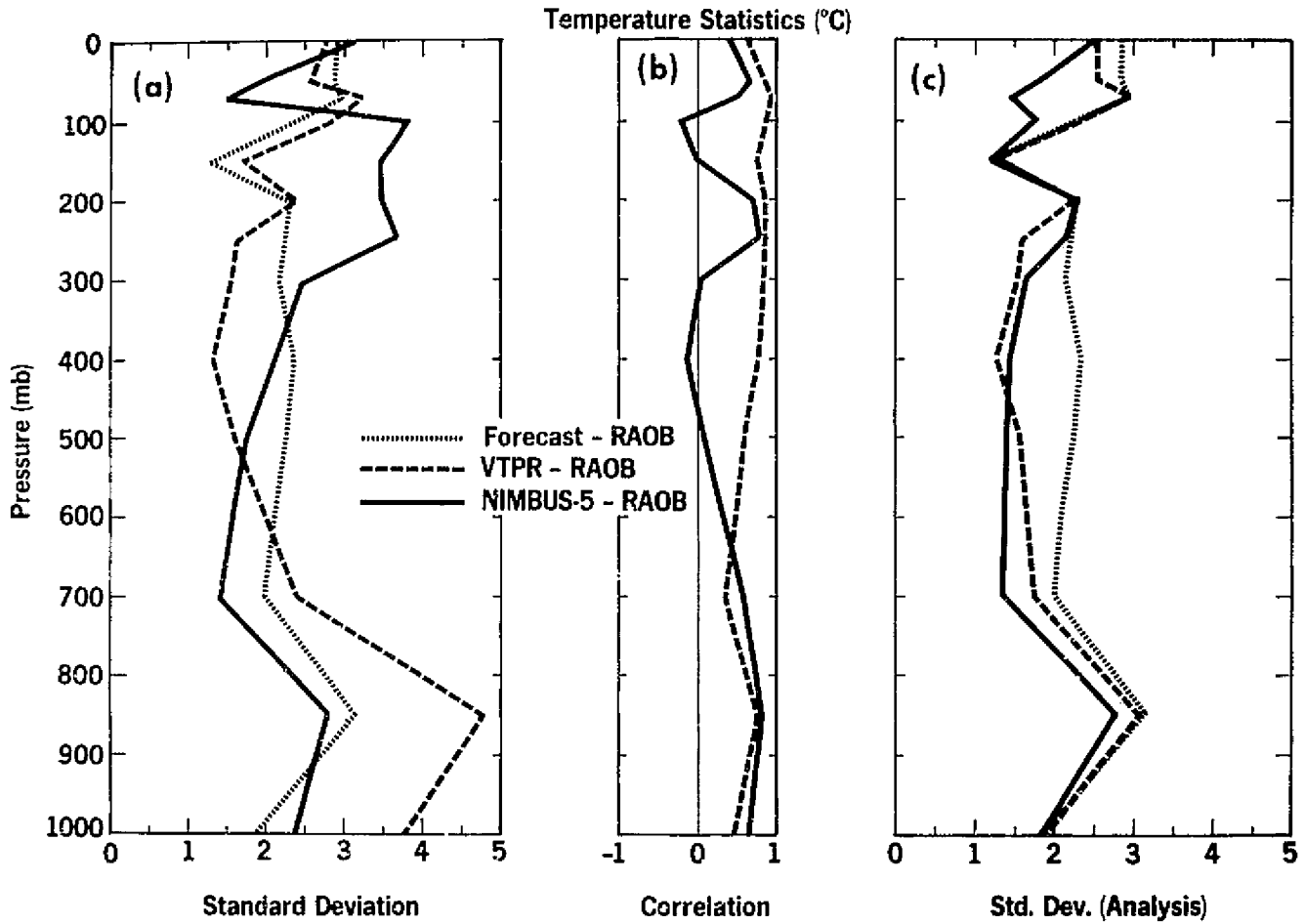

Figure 25--(a) Standard deviation of the difference of temperatures (°C) between those obtained from the radiosonde cross-section analyses and the cross-section analyses of (1) 12-hour forecast (short dashes), (2) the VTPR (long dashes), and (3) the Nimbus-5 (solid curve); (b) correlation of the differences between the cross-section analyses for the forecast and radiosonde temperature data with (1) the differences between the cross-section analyses for the VTPR and radiosonde temperature data (dashed curve) and (2) the differences between the cross-section analyses for the Nimbus-5 and radiosonde temperature data (solid curve); and (c) expected standard deviations of the cross-section analysis of radiosonde temperature data with an "optimum" analysis of (1) forecast data (short dashes), (2) VTPR data (long dashes), and (3) Nimbus-5 data (solid curve).

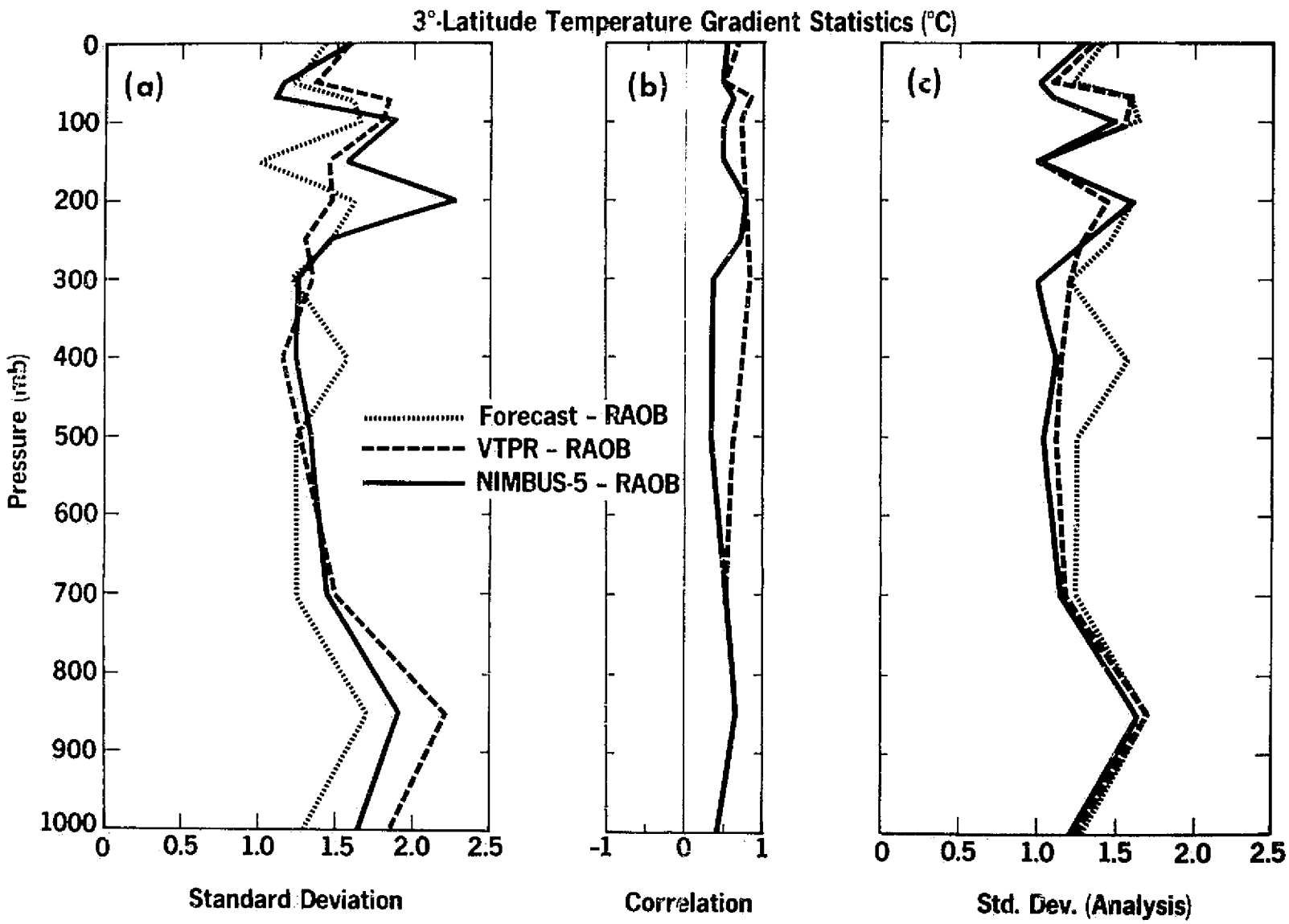

Figure 26--Same as Figure 25 except here it is for temperature gradients (°C) over 3° of latitude.

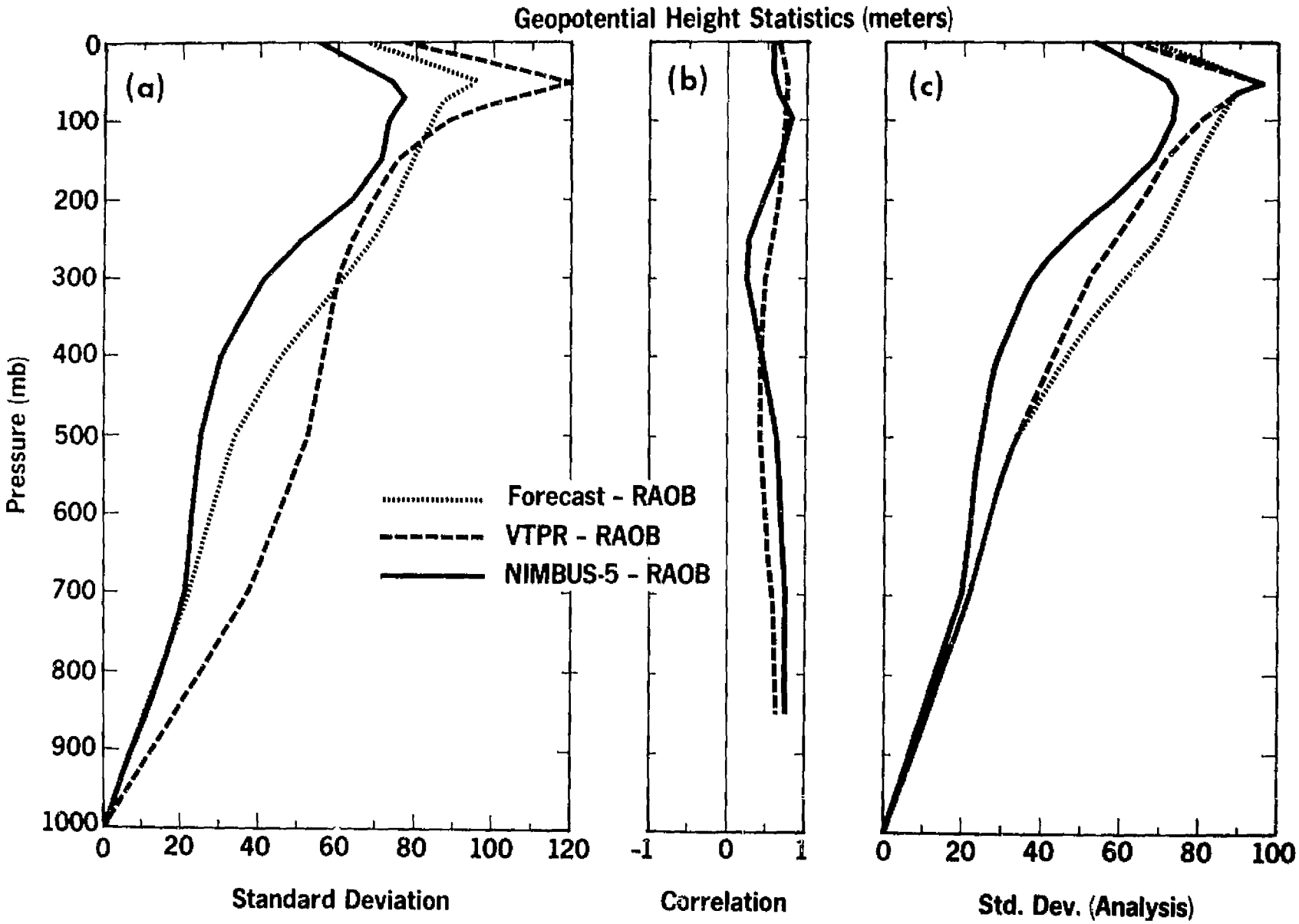

Figure 27--Same as Figure 25 except here it is for geopotential height (m).

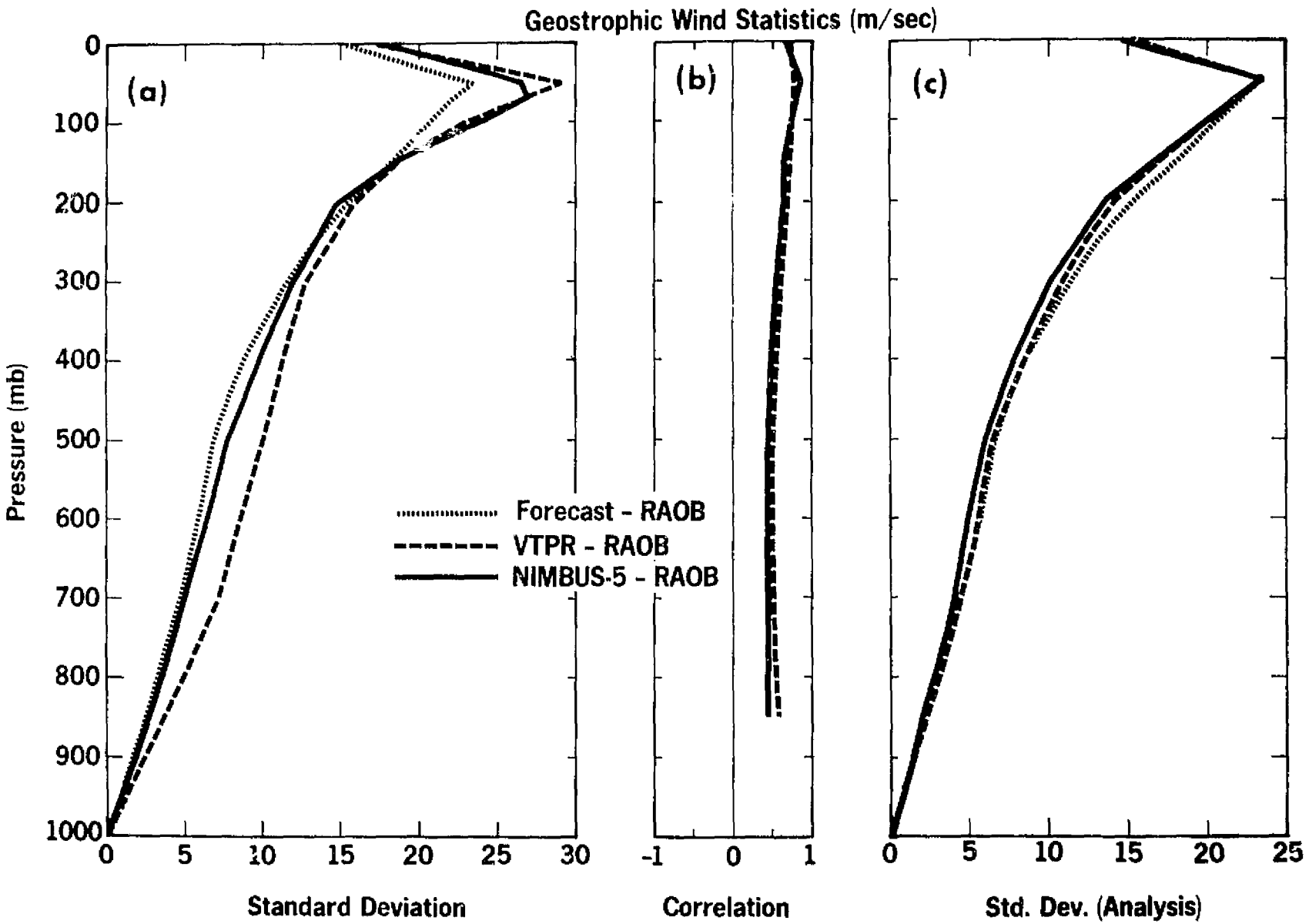

Figure 28--Same as Figure 25 except here it is for geostrophic wind (m/s).

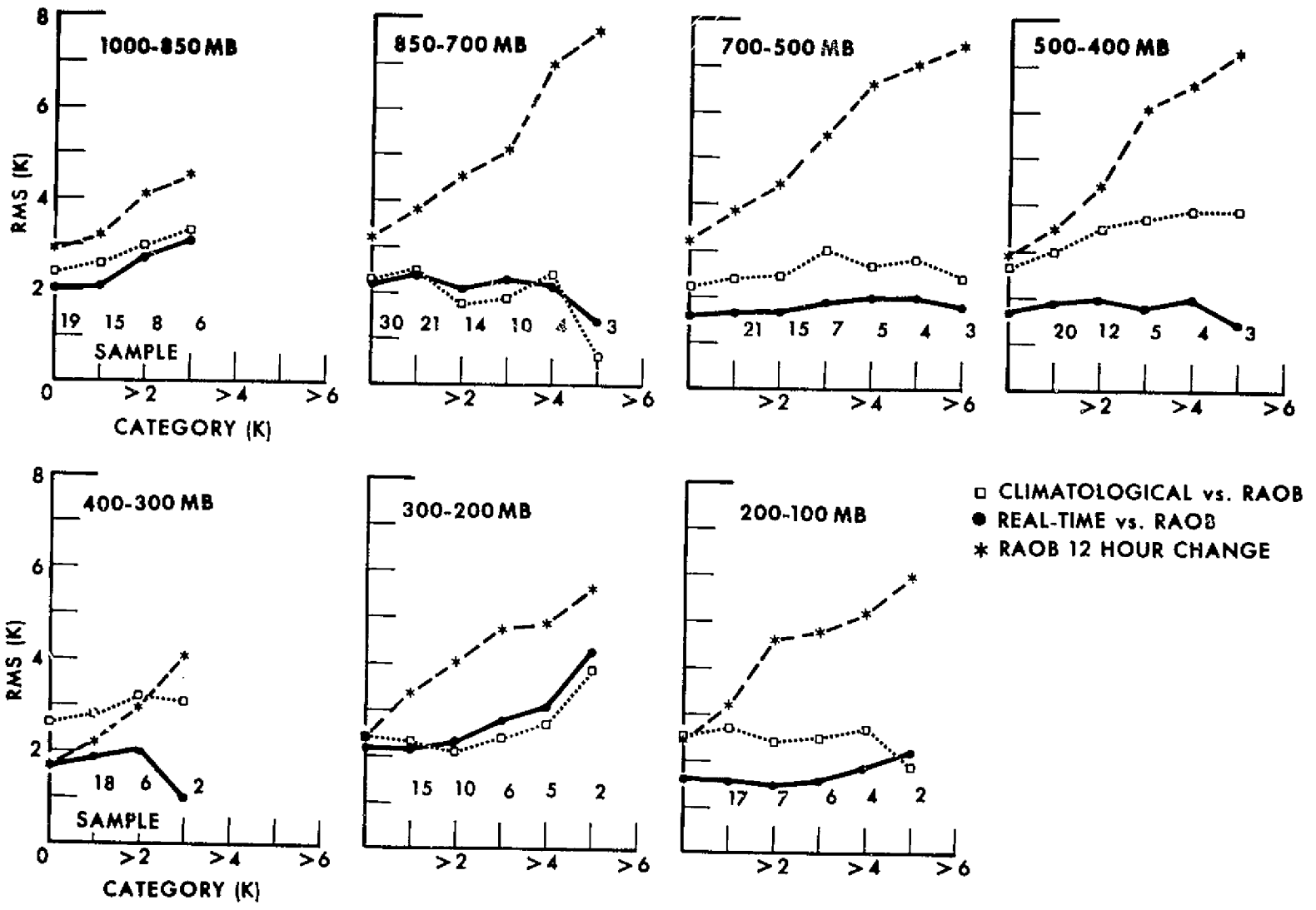

Figure 29--Comparison of Nimbus-5 temperatures obtained with climatological and with relative statistics. RMS differences between satellite-derived and neighboring radiosonde temperatures are shown for categories of 12-hour temperature change as measured by the radiosonde. Categories are selected to include all cases where temperature change is at least the value shown on the abscissa.

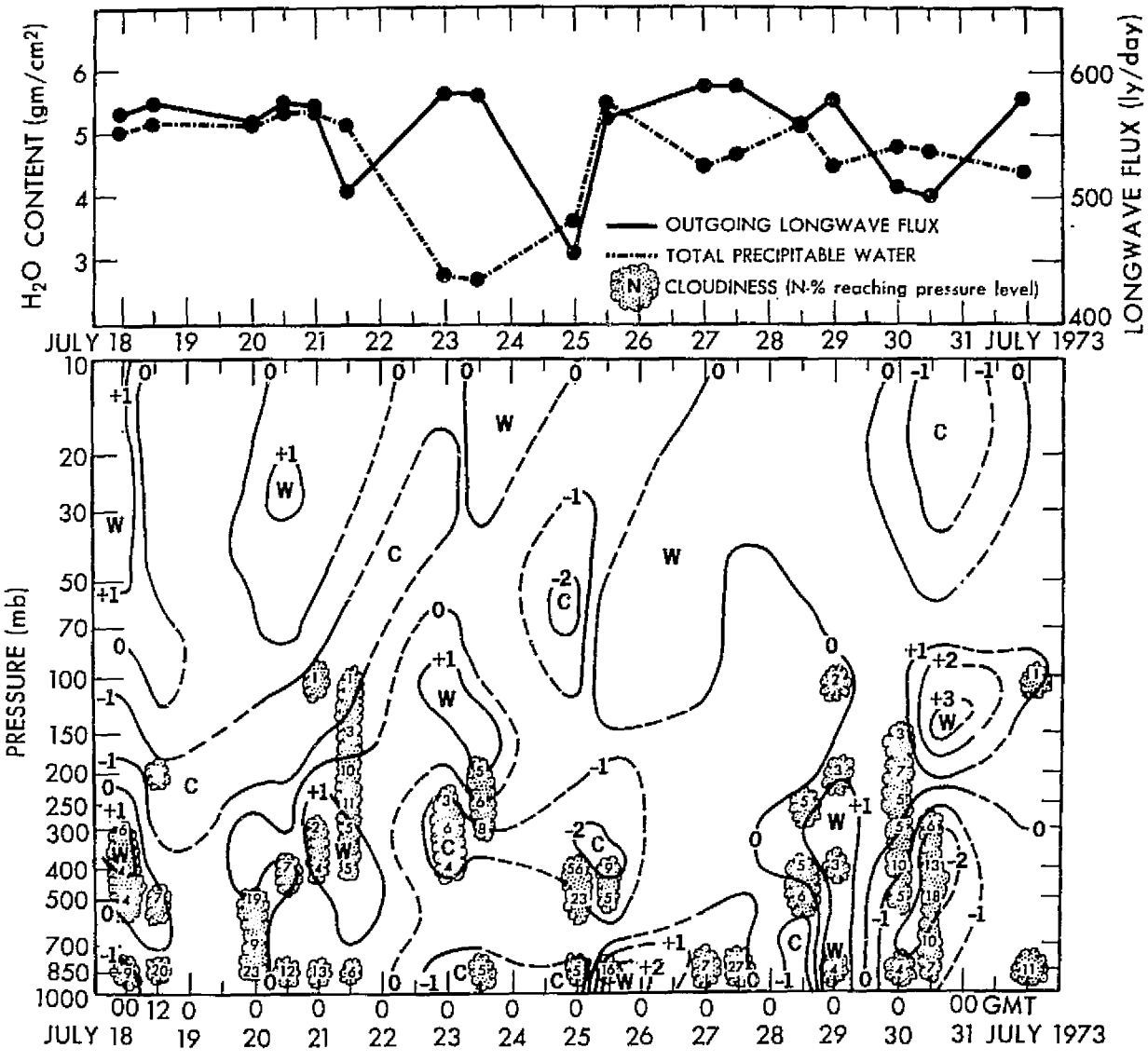

GATE B–SCALE AREA (5°-15°N, 21°-31°W) TEMPERATURE (DEPARTURE FROM MEAN) WATER VAPOR, CLOUDINESS, AND OUTGOING LONGWAVE FLUX DISTRIBUTION

Figure 30--Time cross-section (July 18-31, 1973) of vertical temperature (departure from mean) total precipitable water, cloudiness and outgoing longwave flux as specified from ITPR radiance data for the GATE B-scale area (5-15N, 21-31W).

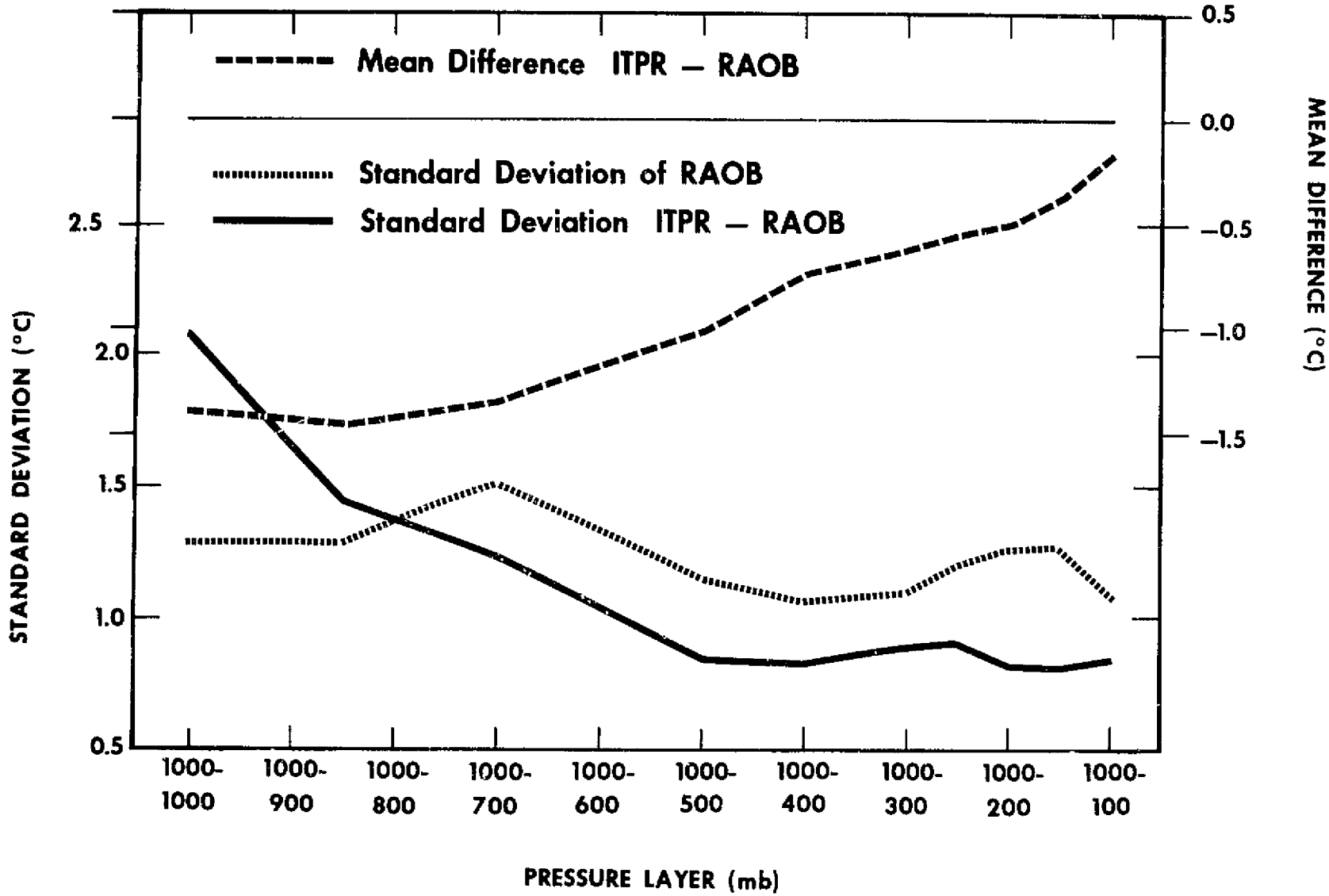

Figure 31--Standard deviations of RAOB, ITPR-RAOB and Mean difference of ITPR-RAOB temperatures for layers extending from the 1000-mb level.

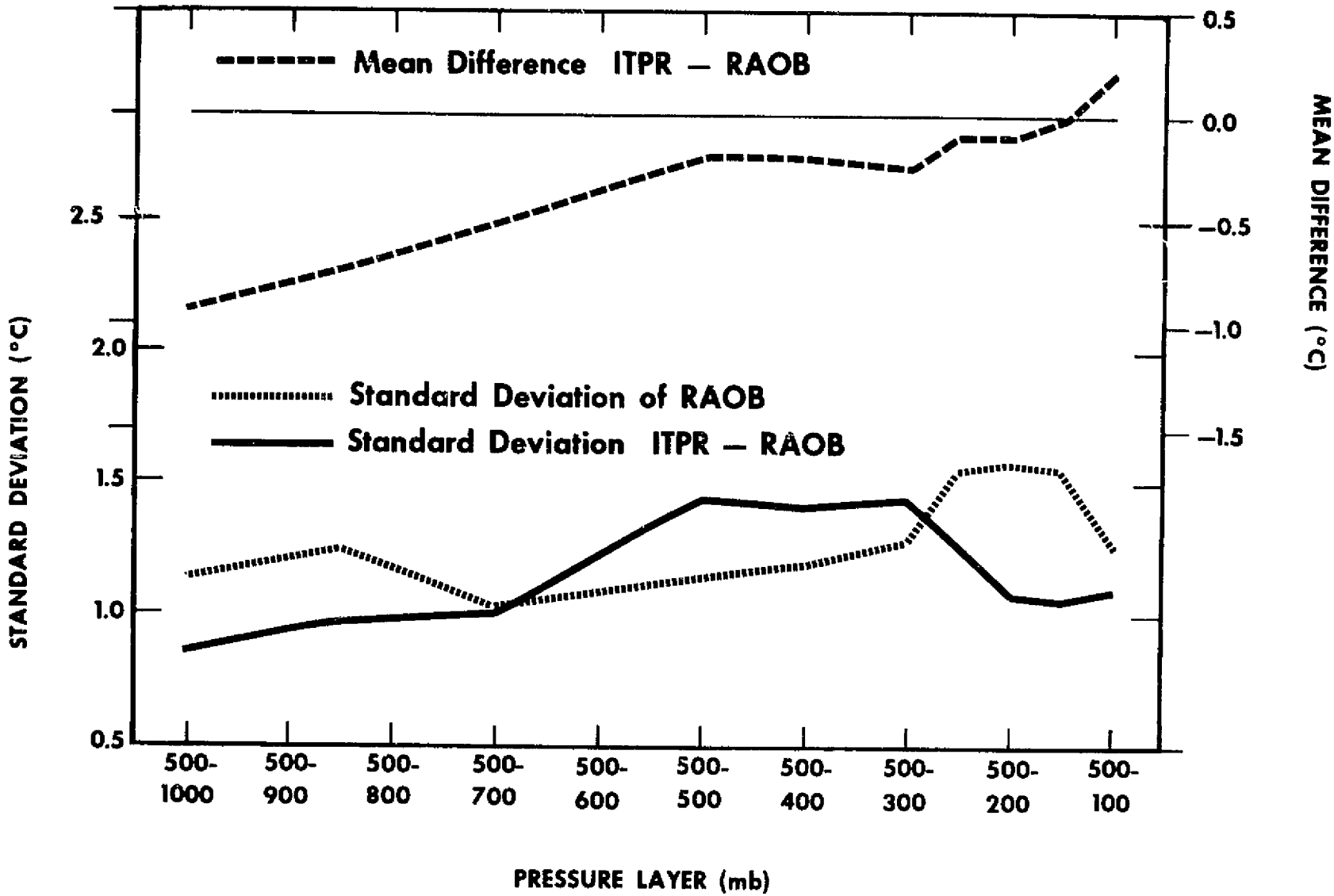

Figure 32--Same as Figure 31 except this is for layers extending from the 500-mb level.

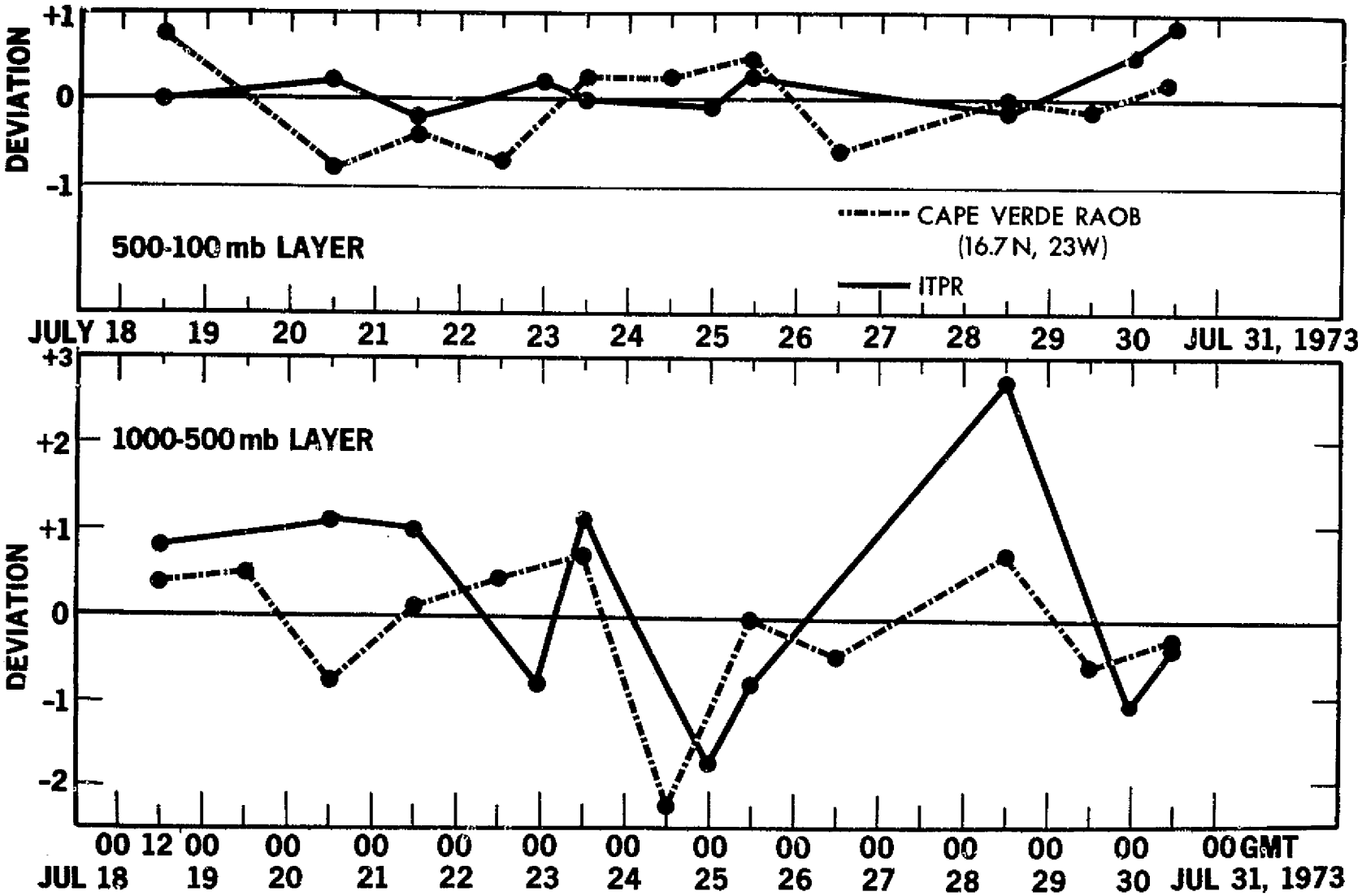

Figure 33--Comparison between ITPR layer mean temperatures and the Cape Verde RAOB.

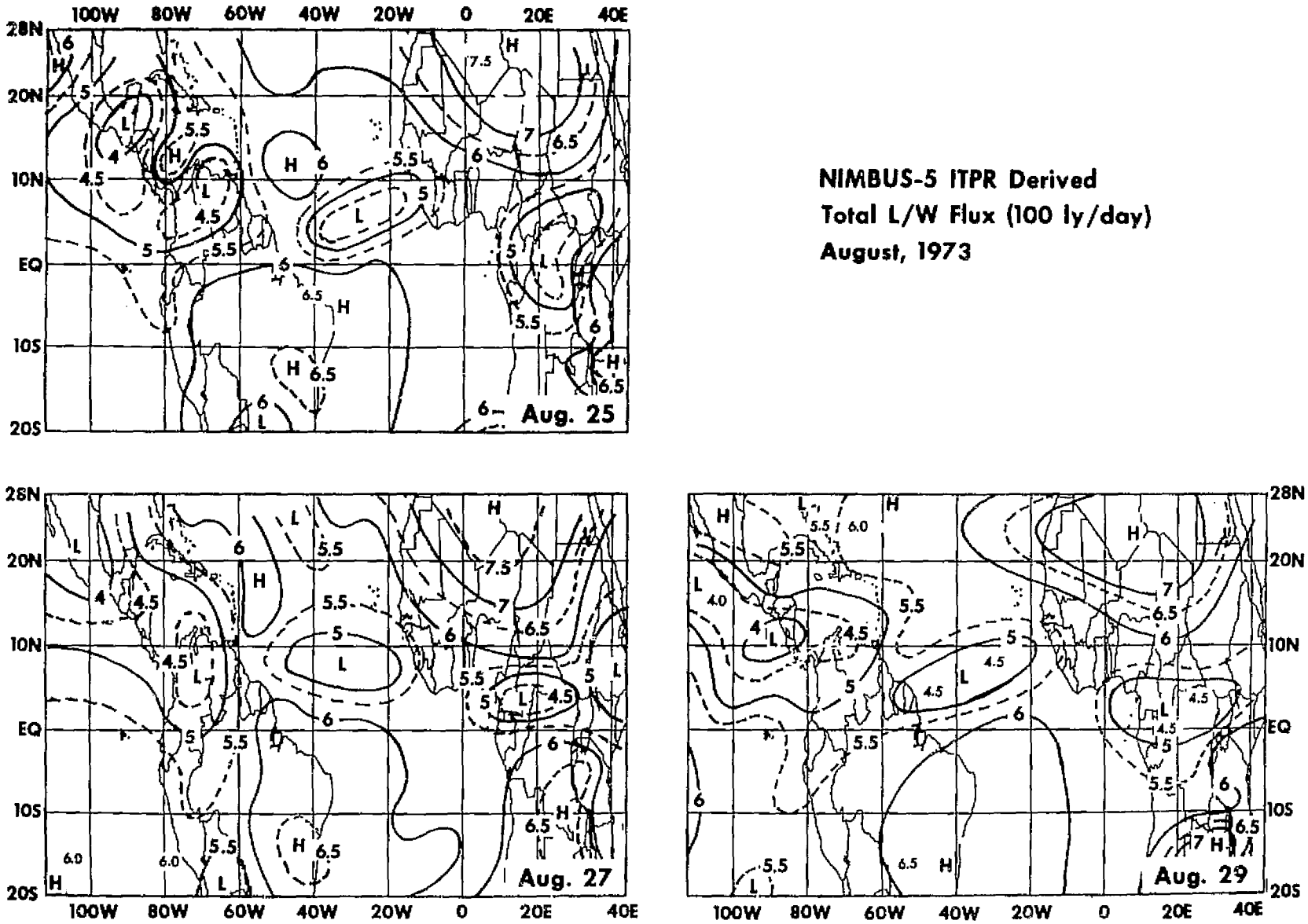

Figure 34--Analyses of ITPR derived longwave flux for August 25, 27 and 29, 1973, for the GATE A-scale area.

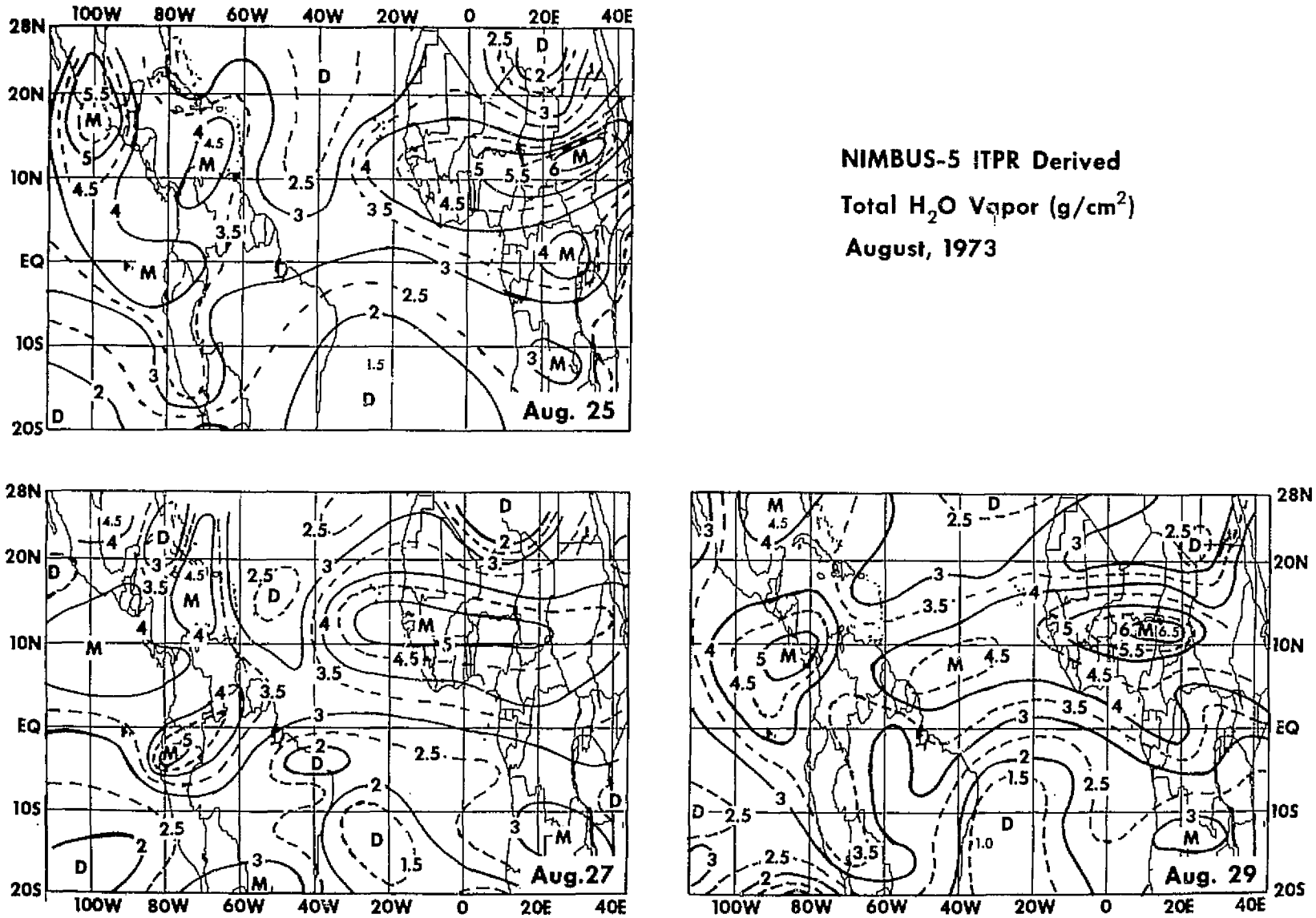

Figure 35--Same as Figure 34 except this is for total water vapor.

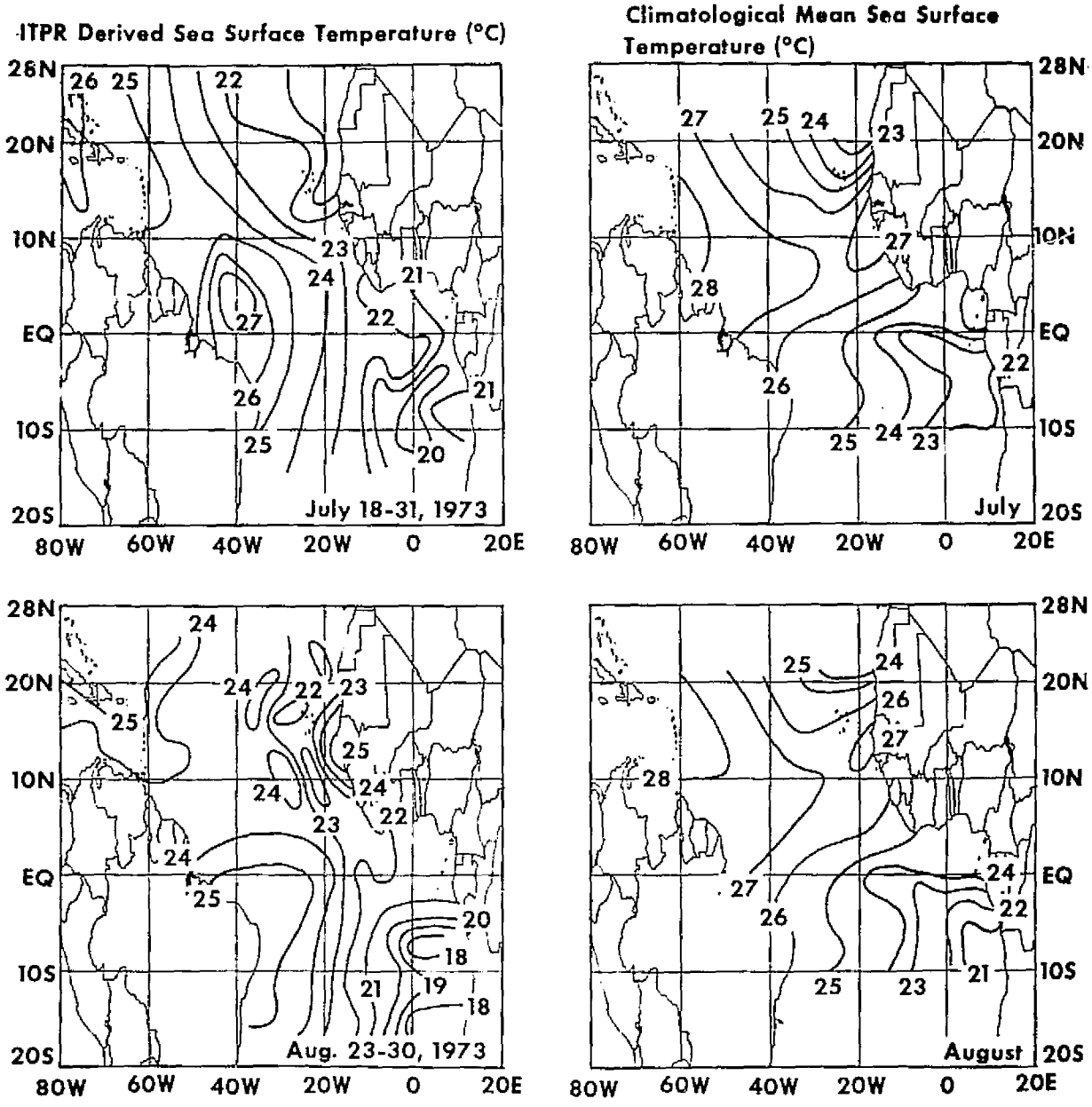

Figure 36--Comparison between ITPR-derived sea surface temperature analyses (July and August 1973) and Climatology (60 years).

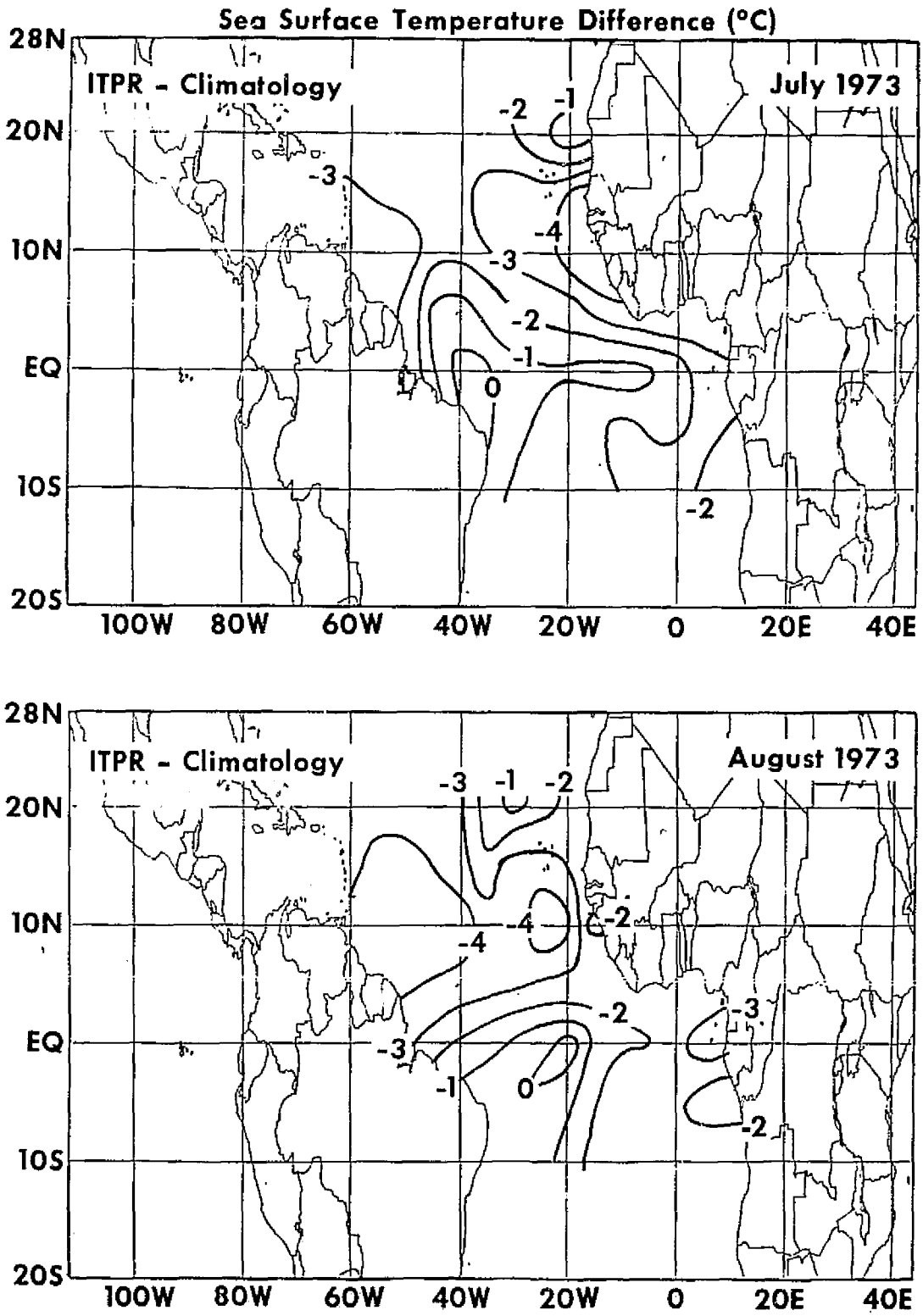

Figure 37--Sea surface temperature differences between ITPR-derived (July and August 1973) and Climatology (60 years).

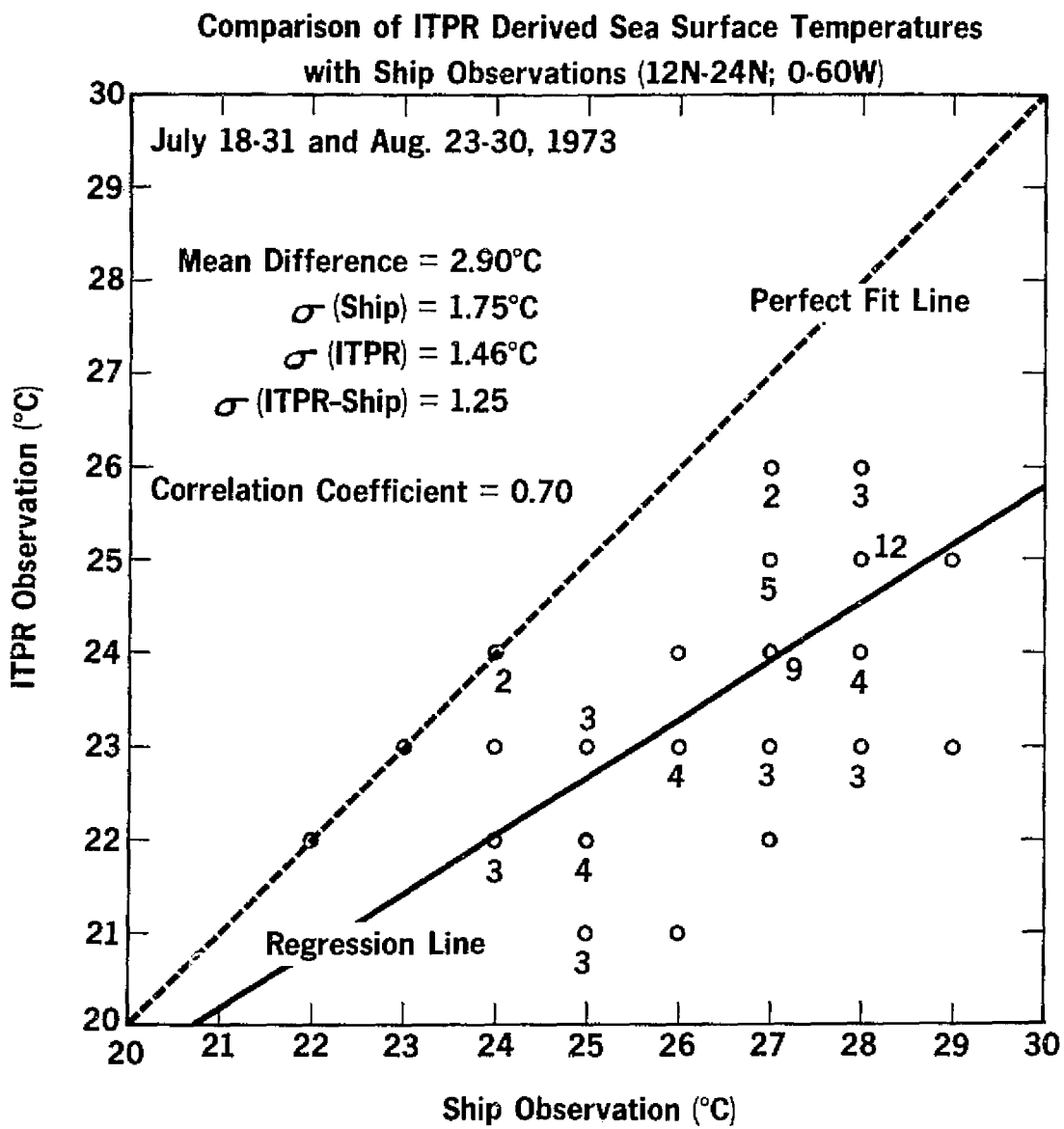

Figure 38--Scatter diagram showing comparison between ITPR derived sea surface temperatures and ship observations for July 18-31 and August 23-30, 1973. (Value below circles show number of identical points).

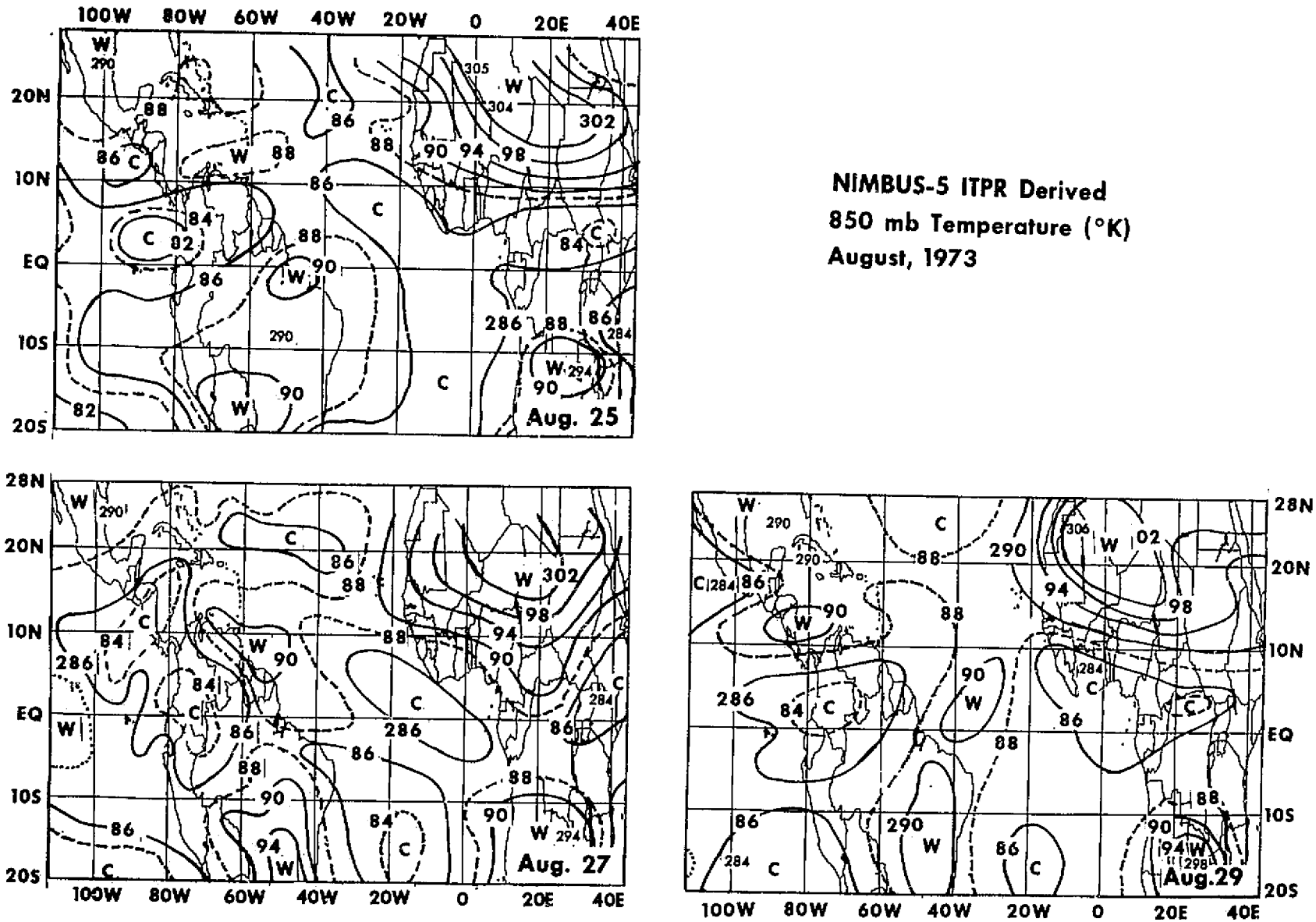

Figure 39--Same as Figure 34 except this is for 850-mb temperature.

NIMBUS-5 ITPR Derived
250 mb Temperature (°K)
August, 1973

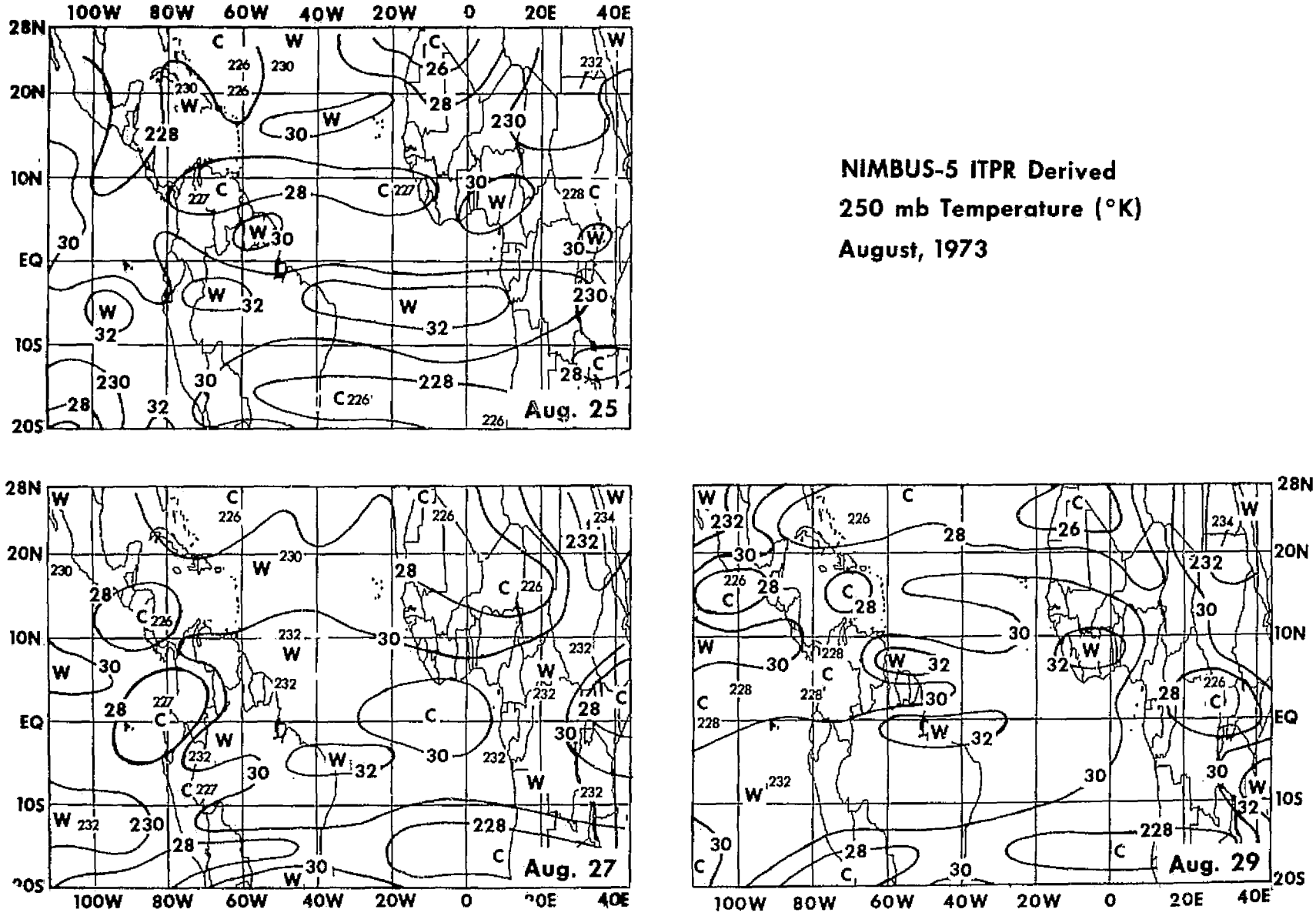

Figure 40--Same as Figure 34 except this is for 250-mb temperature.

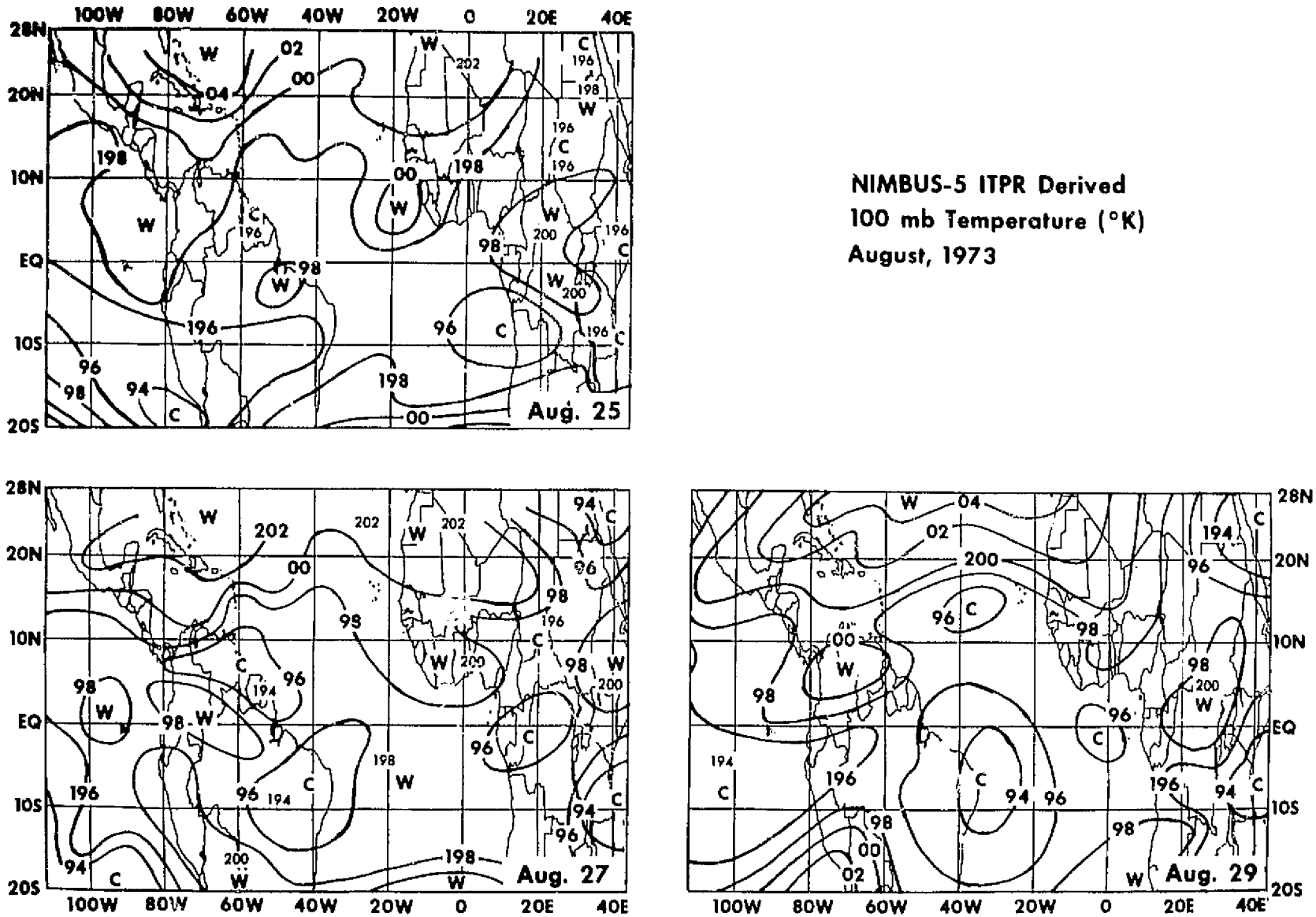

Figure 41--Same as Figure 34 except this is for 100-mb temperature.

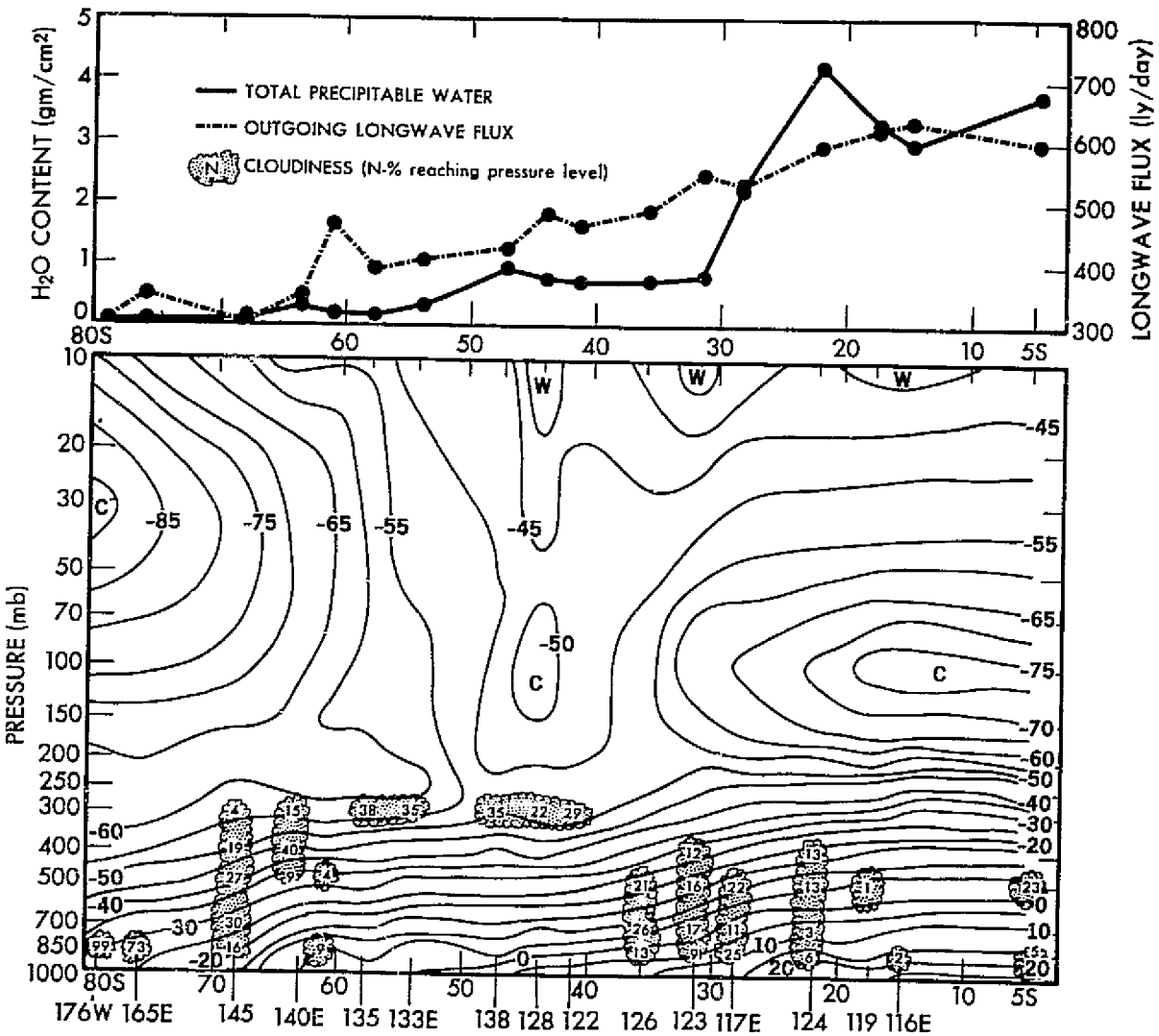

Figure 42--Cross-section of vertical temperature, total water vapor, cloudiness and outgoing longwave flux deduced from Nimbus-5 radiance data in the Southern Hemisphere for August 11, 1973.

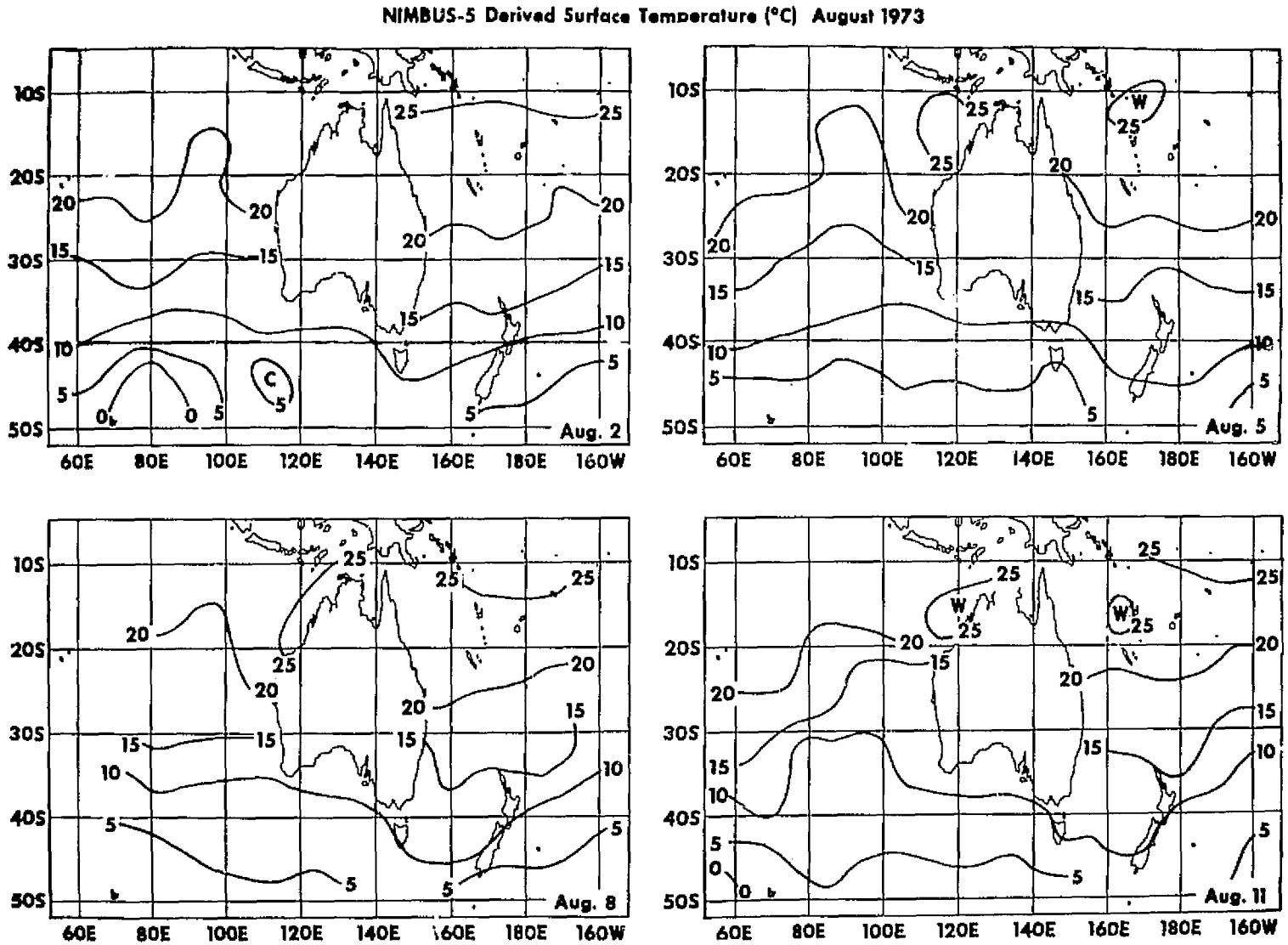

Figure 43--Analyses of Nimbus-5 derived sea-surface temperatures in the Southern Hemisphere for August 2, 5, 8, 11, 1973.

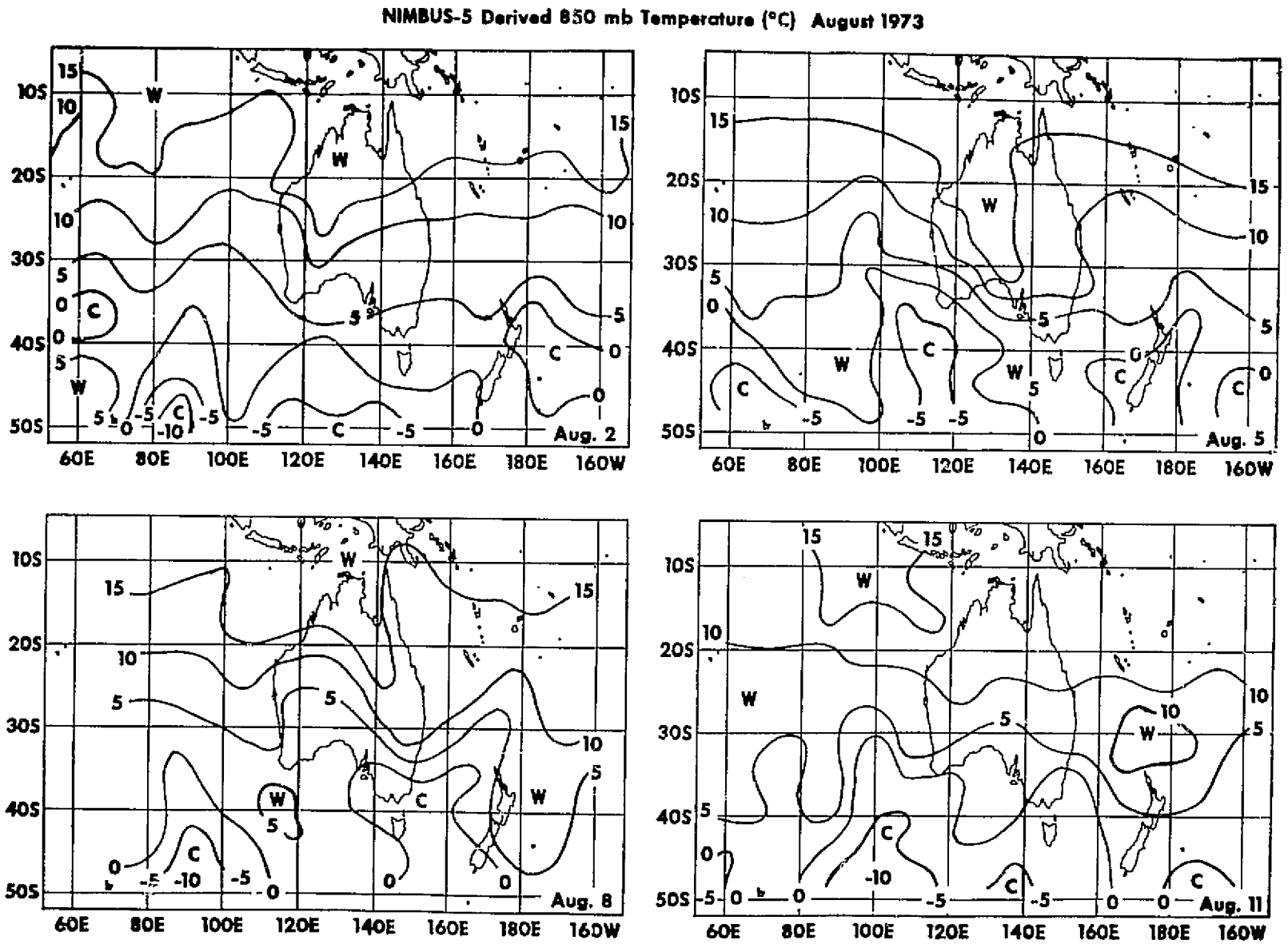

Figure 44--Same as Figure 43 except this is for the 850-mb level.

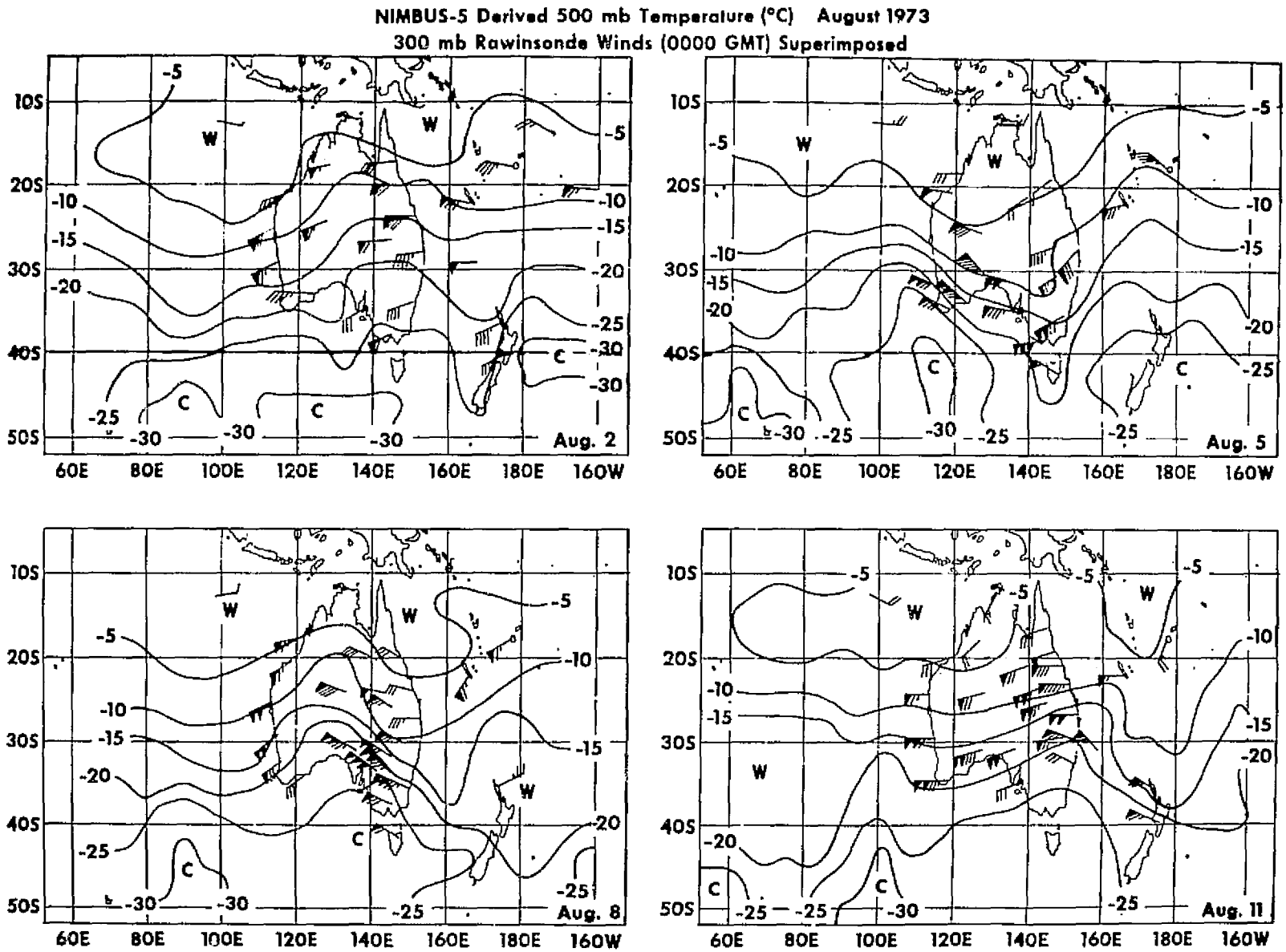

Figure 45--Same as Figure 43 except this is for the 500-mb level.

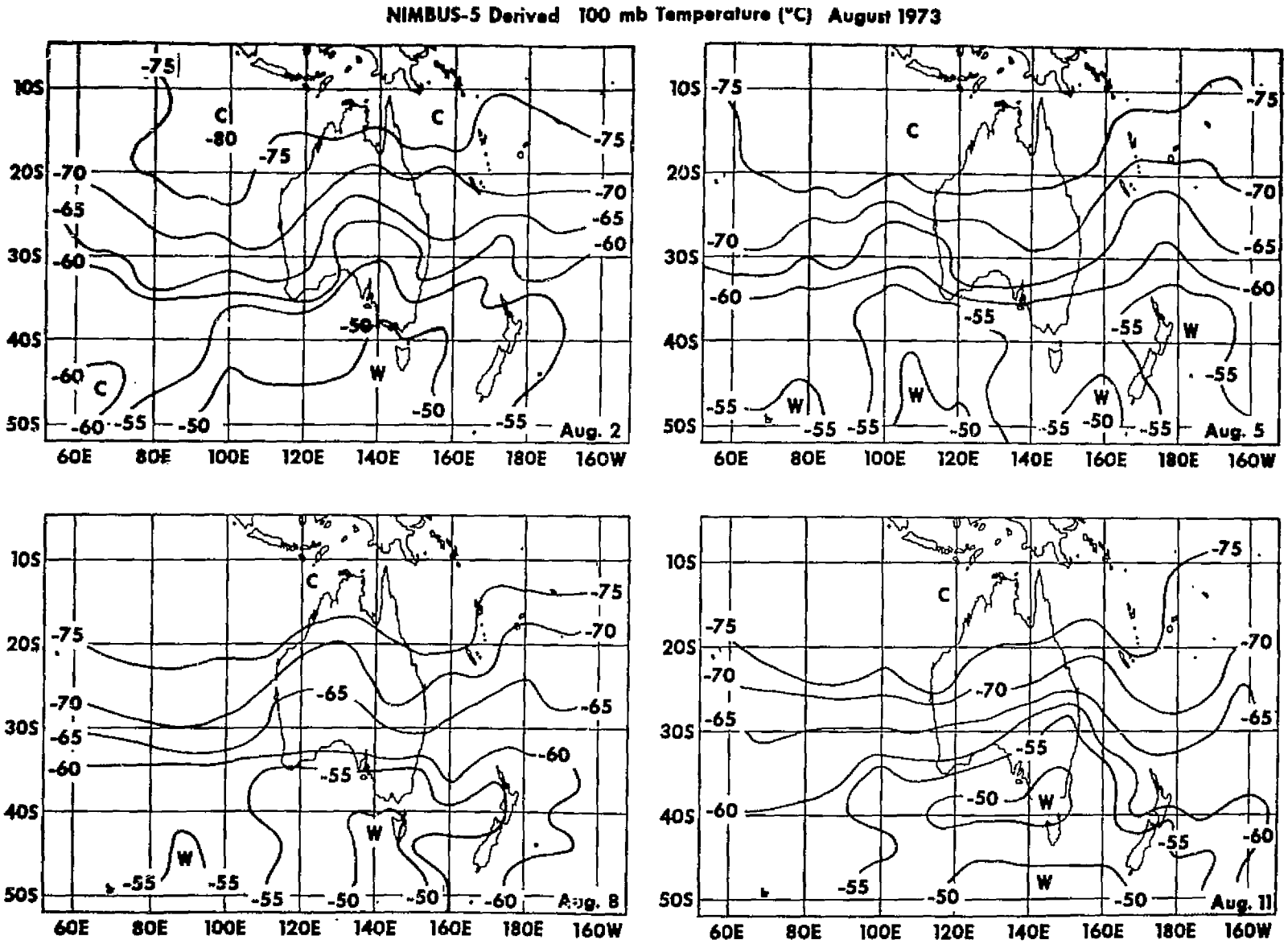

Figure 46--Same as Figure 43 except this is for the 100-mb level.

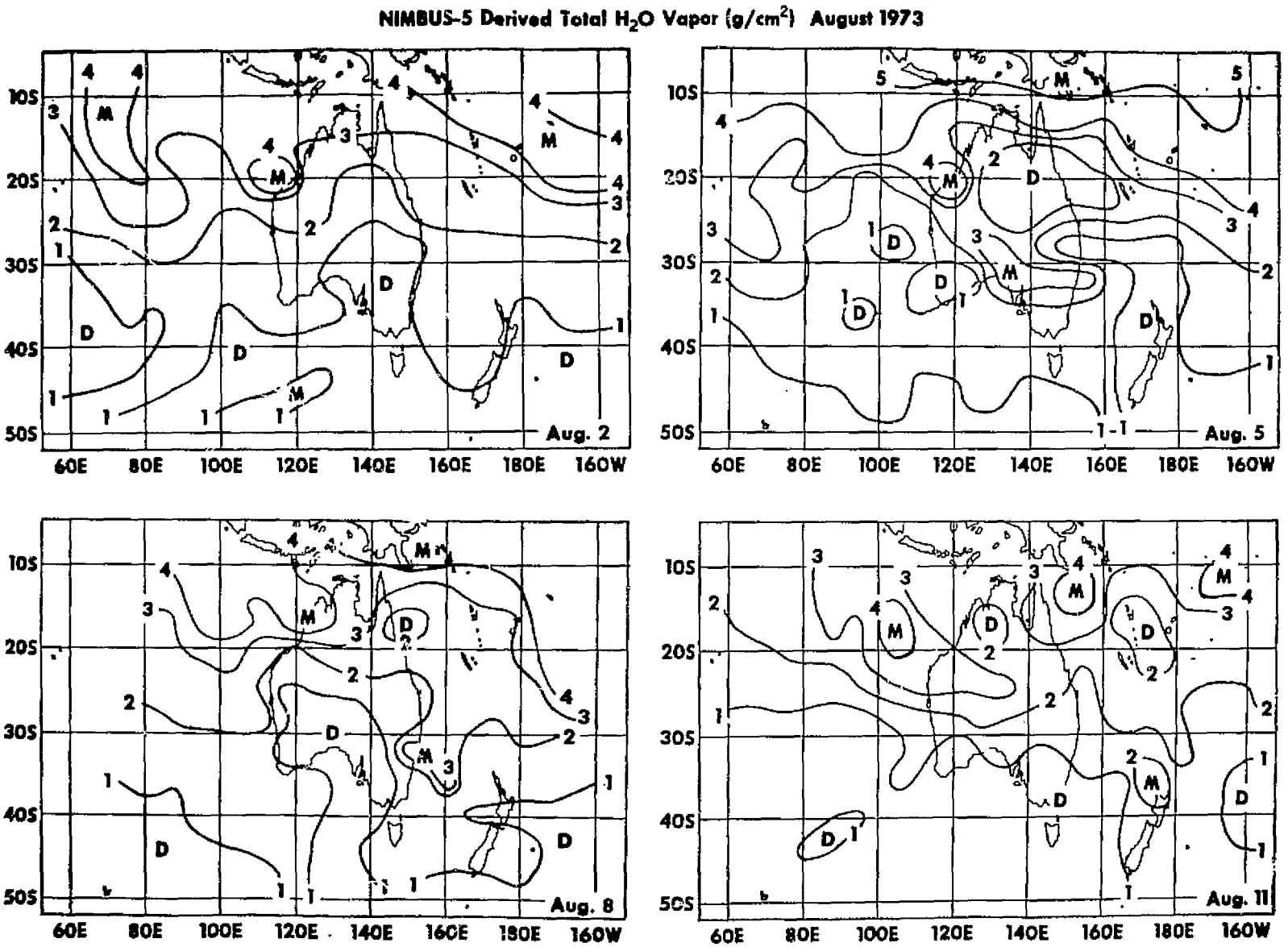

Figure 47--Same as Figure 43 except this is for the total precipitable water.

Comparison of NIMBUS-5 Derived Standard Layer Mean Temperatures (T_N) with Analyzed Radiosonde Observations (T_R) in the Southern Hemisphere (10°-60°S, 52°-208°E) during a Midwinter Period (Aug. 1-Aug. 11, 1973)

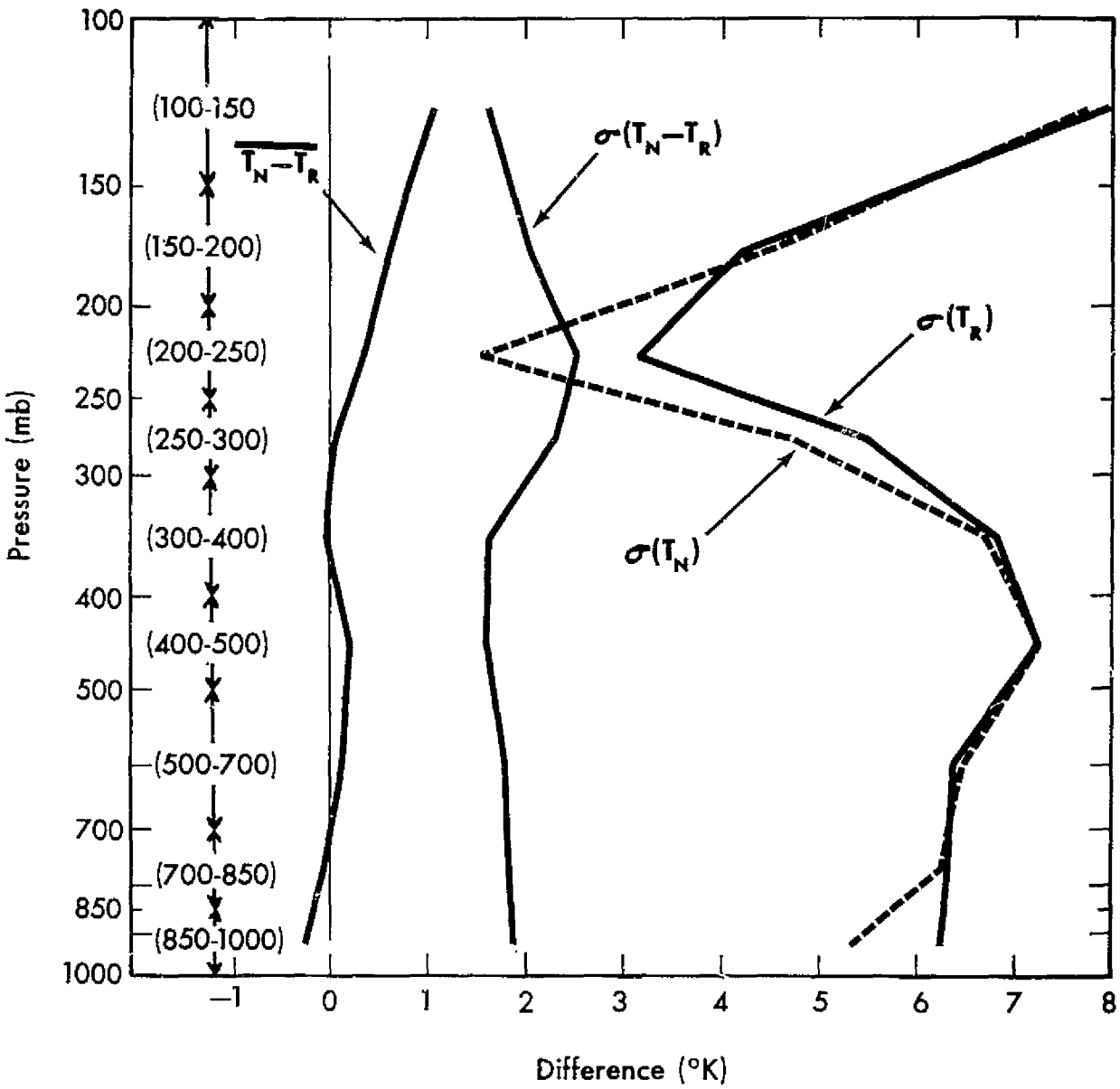

Figure 48--Comparison of Nimbus-5 derived standard layer mean temperatures (Tn) with analyzed radiosonde observations (Tr) in the Southern Hemisphere (10-60S, 52-208E) during a mid-winter period (August 1-11, 1973).

Comparison of NIMBUS-5 Derived Geopotential Heights Above 1000 mb (Z_N) with Analyzed Radiosonde Observations (Z_R) in theSouthern Hemisphere (10°-60°S, 52°-208°E) during a Midwinter Period (Aug. 1-Aug. 11, 1973)

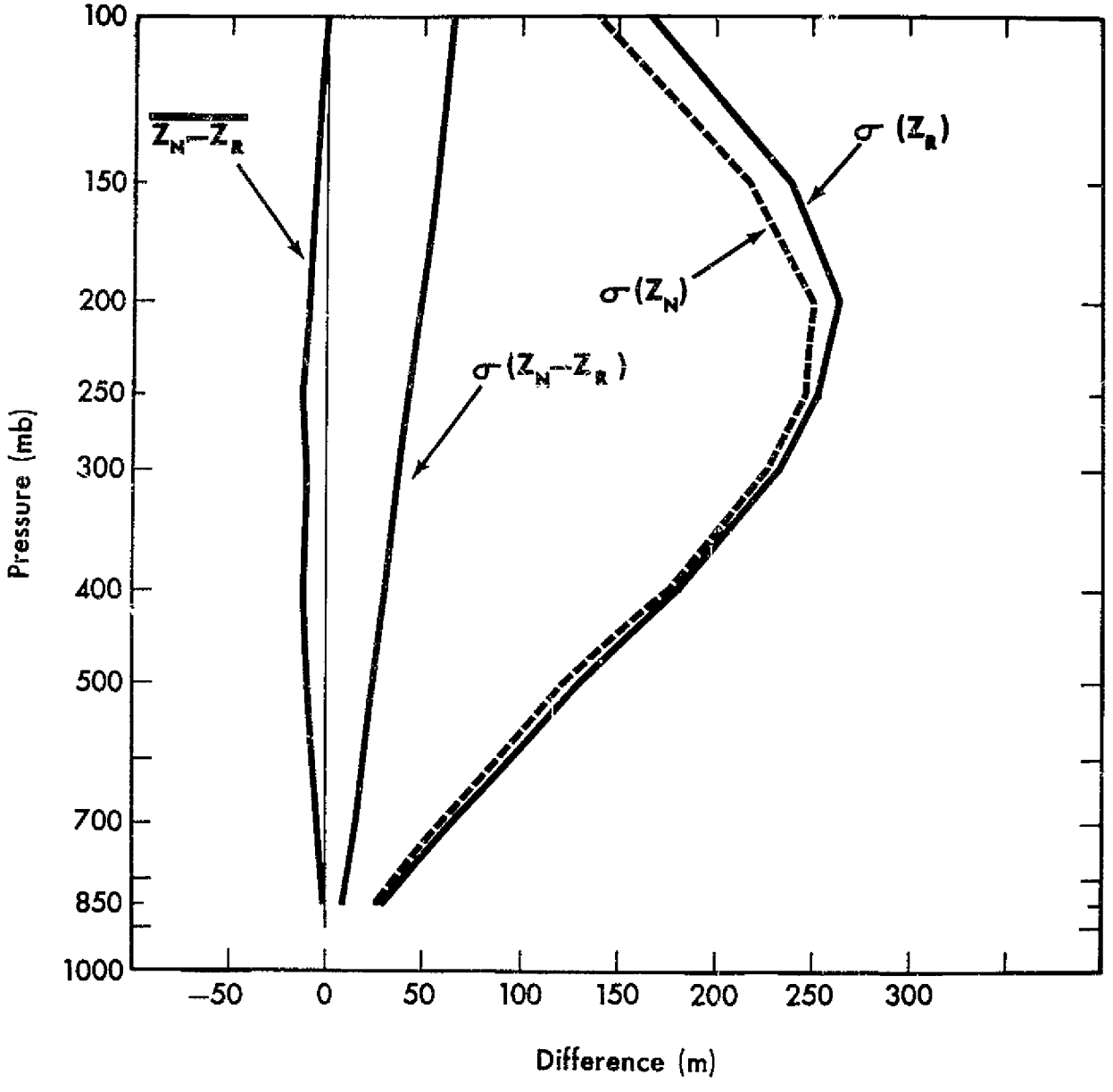

Figure 49--Same as Figure 48 except this is for geopotential heights.

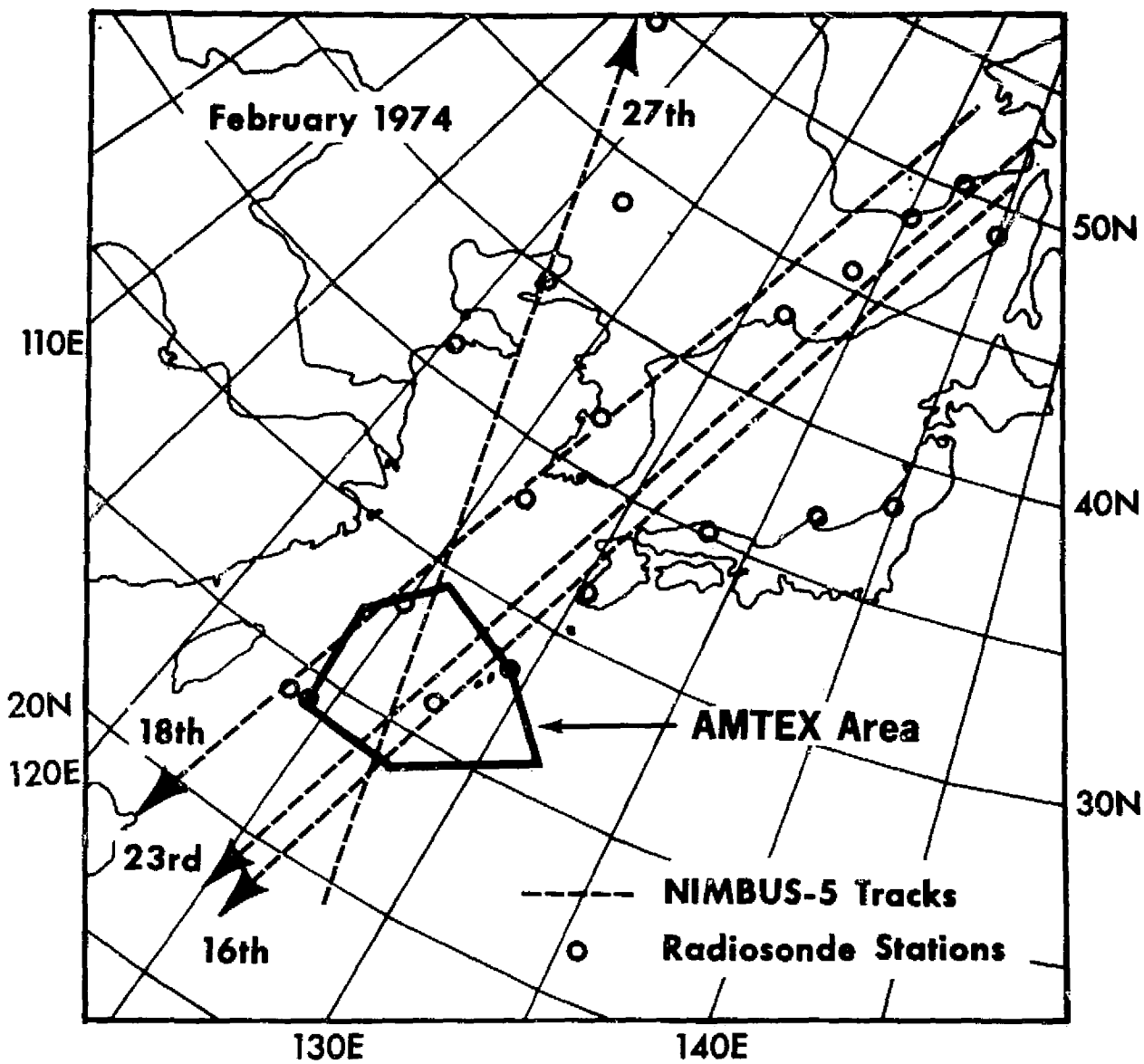

Figure 50--Geographical locations of radiosonde and Nimbus-5 soundings

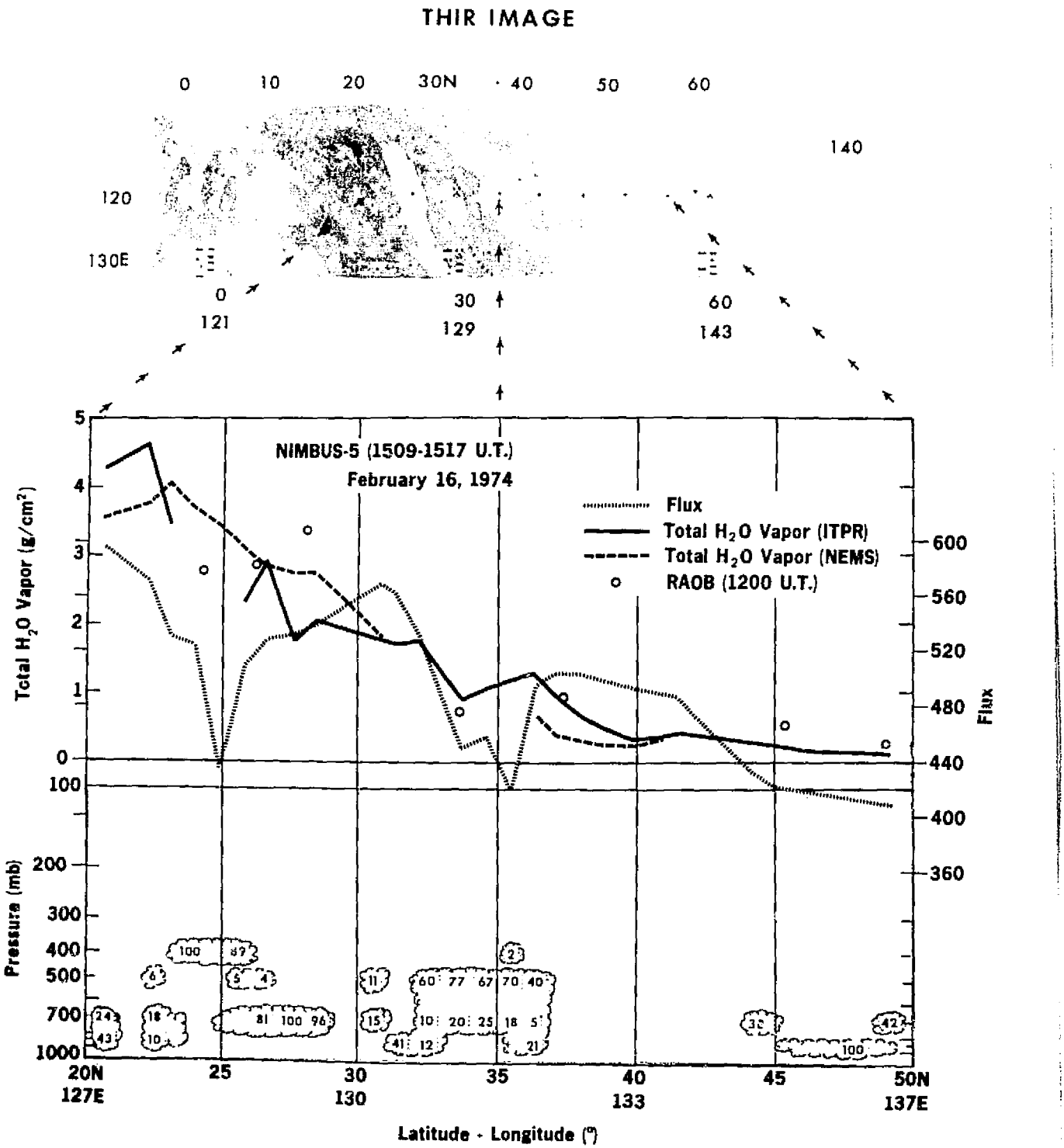

Figure 51--Distribution of cloud amount, cloud height, water vapor content (g/cm^2) and outgoing long-wave flux (langley/day) derived from the Nimbus-5 radiance measurements along the orbital track for February 16, 1974.

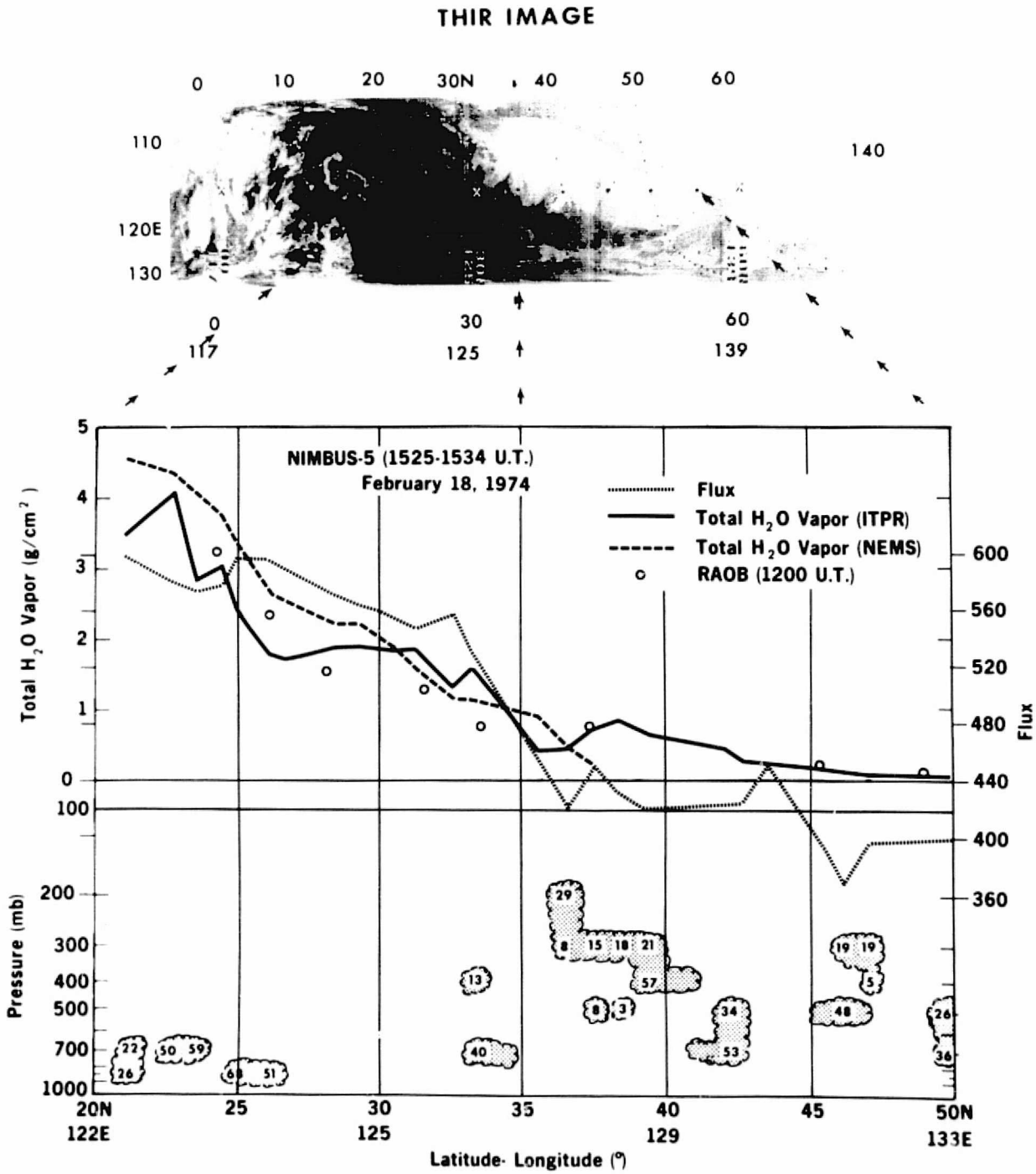

Figure 52--Same as Figure 51 for February 18, 1974.

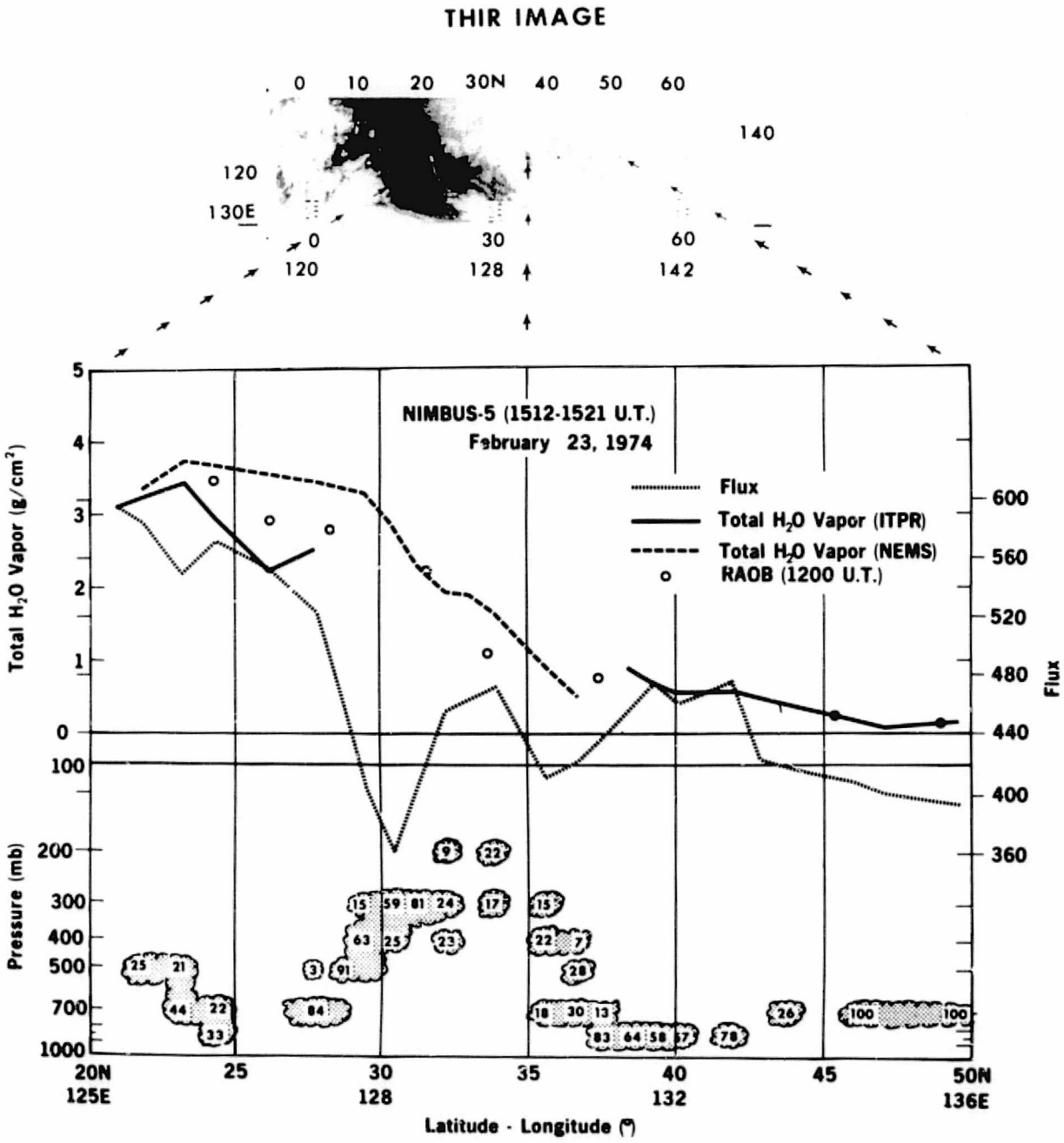

Figure 53--Same as Figure 51 for February 23, 1974.

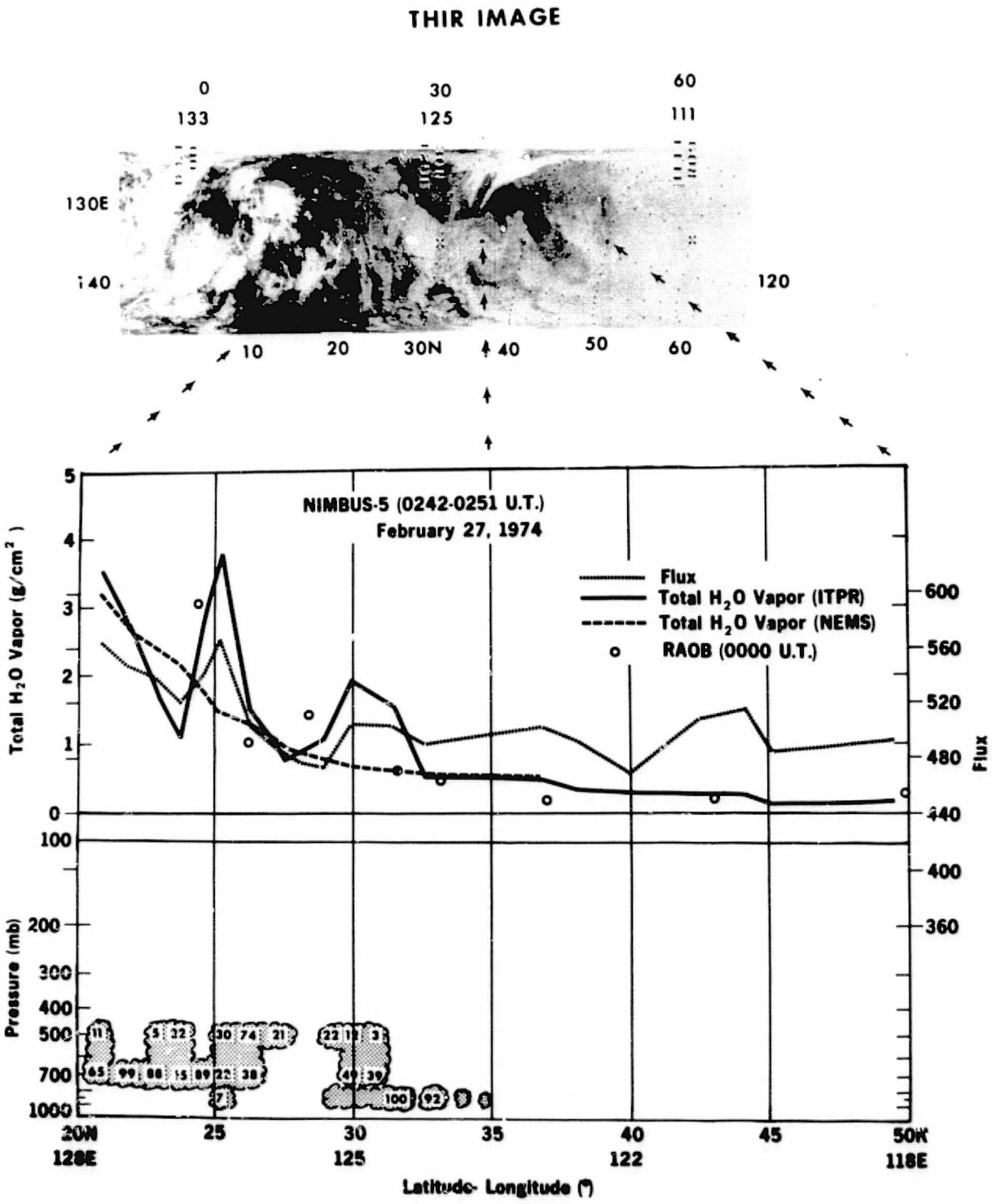

Figure 54--Same as Figure 51 for February 27, 1974.

Temperature Cross Sections, °C

February 16, 1974

Ⓐ **RAOB, 1200 U.T.**

Ⓑ **NIMBUS-5 , 1509-1517 U.T.**

Ⓒ **NIMBUS-5, with Mean Error Removed**

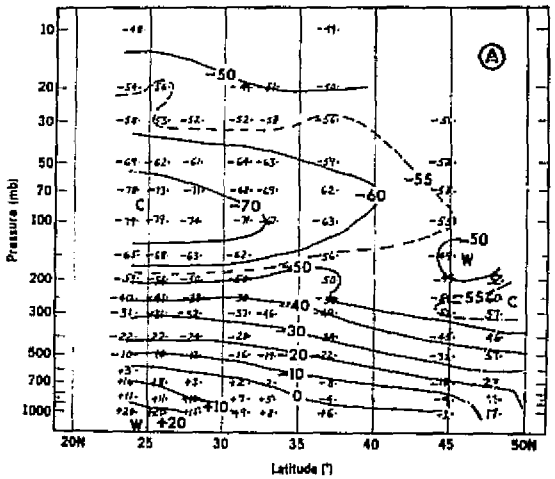

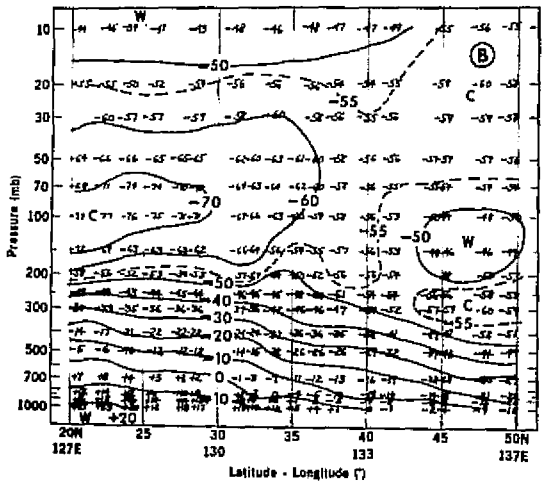

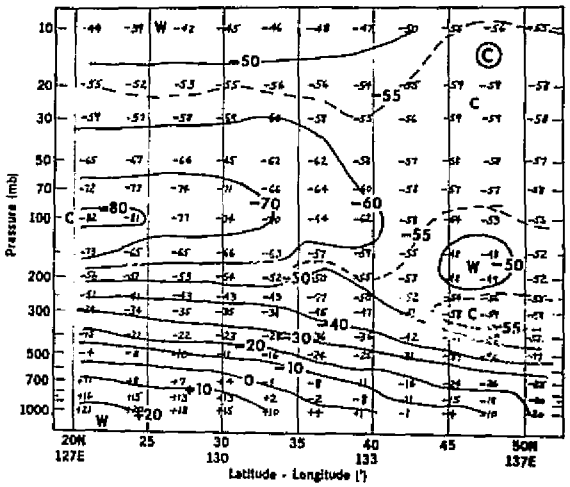

Figure 55--Cross sections of temperatures for February 16, 1974.
(A) Radiosonde temperature
(B) Nimbus-5 temperatures
(C) Mean-error-removed temperatures

Temperature Cross Sections, °C

February 18, 1974

Ⓐ **RAOB, 1200 U.T.**

Ⓑ **NIMBUS-5, 1525-1534 U.T.**

Ⓒ **NIMBUS-5, with Mean Error Removed**

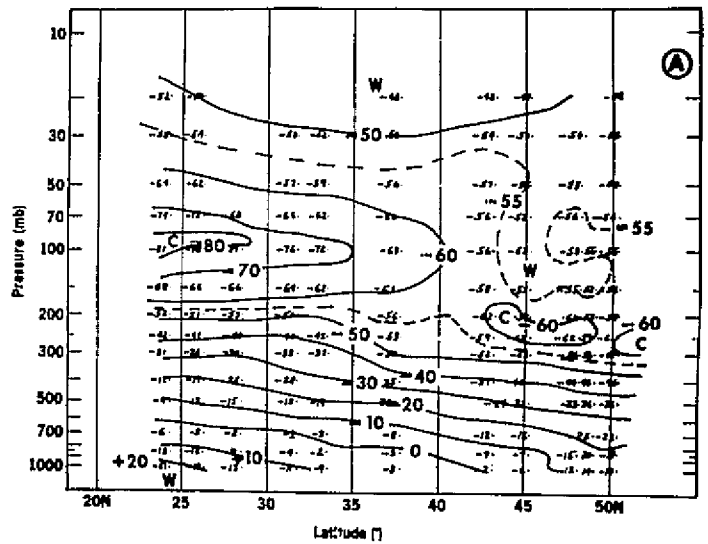

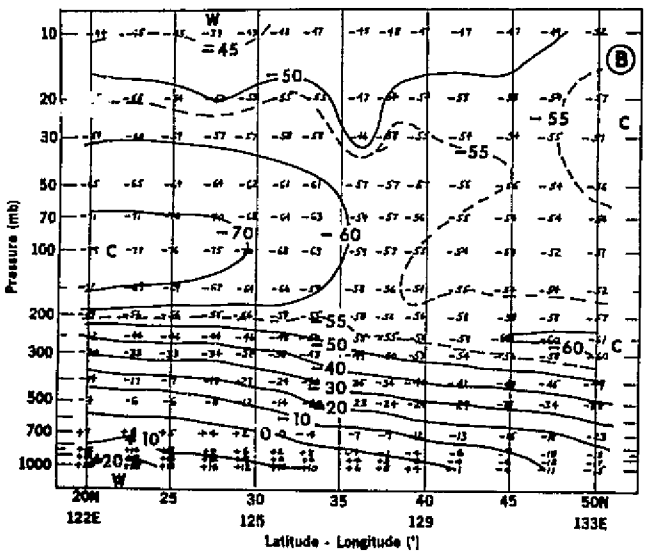

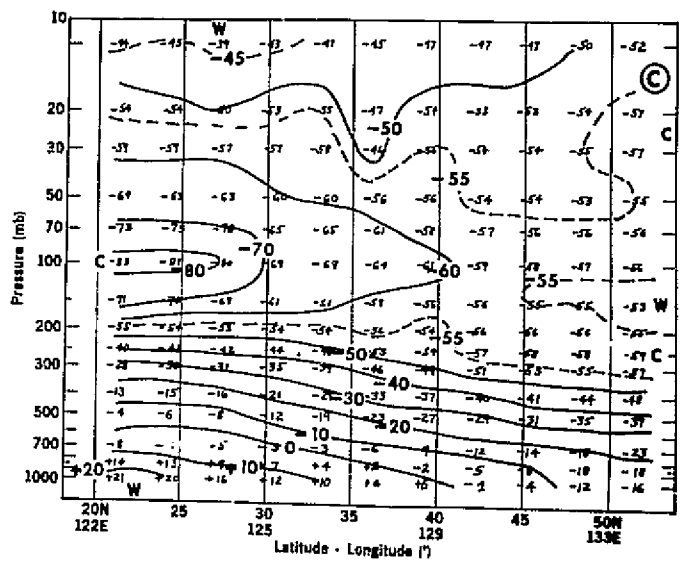

Figure 56--Same as Figure 55 for February 18, 1974.

Temperature Cross Sections, °C

February 23, 1974

Ⓐ **RAOB, 1200 U.T.**

Ⓑ **NIMBUS-5, 1512-1521 U.T.**

Ⓒ **NIMBUS-5, with Mean Error Removed**

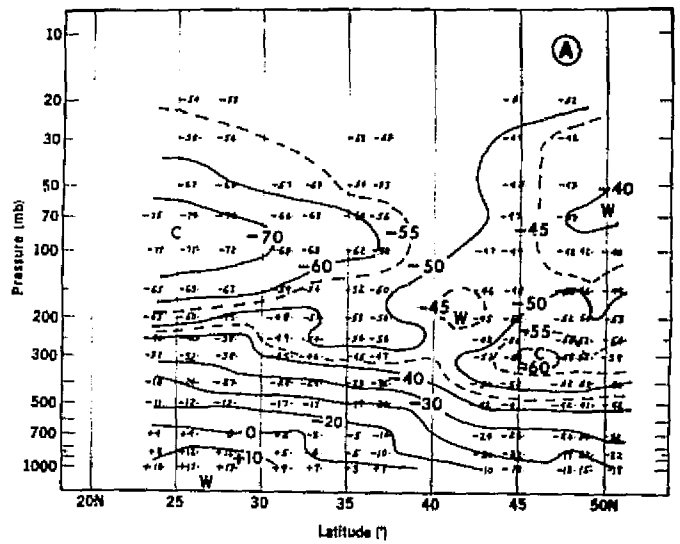

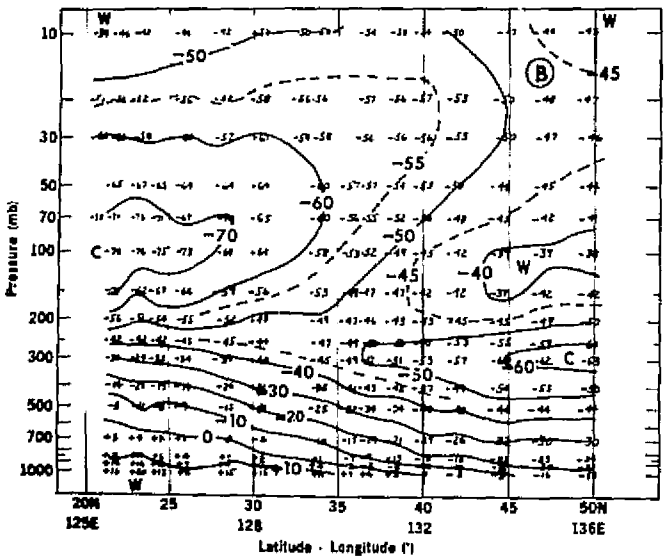

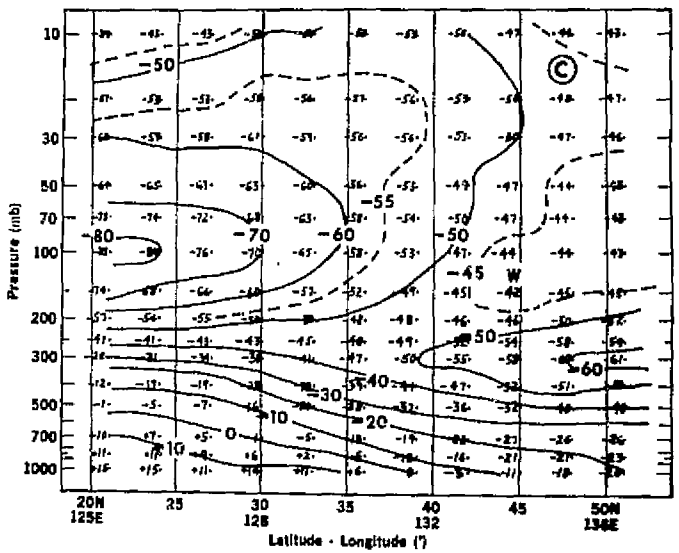

Figure 57--Same as Figure 55 for February 23, 1974.

Temperature Cross Sections, °C

February 27, 1974

Ⓐ **RAOB, 0000 U.T.**

Ⓑ **NIMBUS-5, 0242-0251 U.T.**

Ⓒ **NIMBUS-5, with Mean Error Removed**

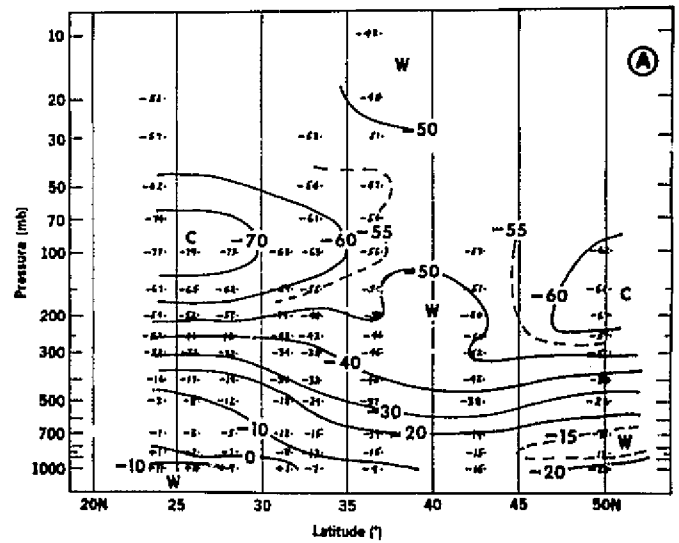

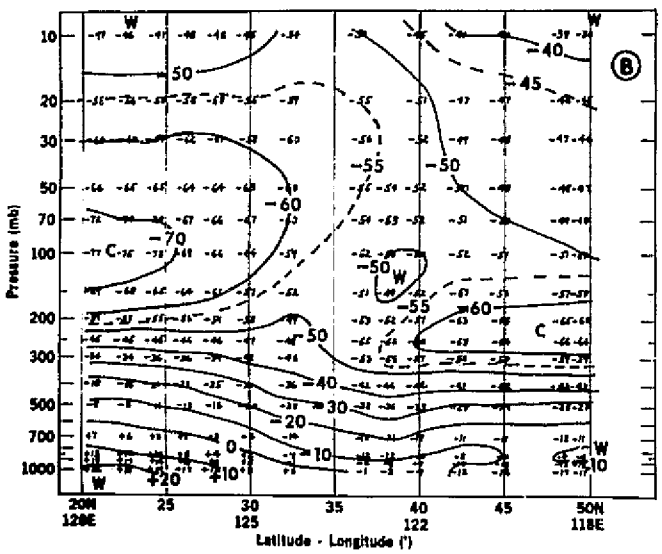

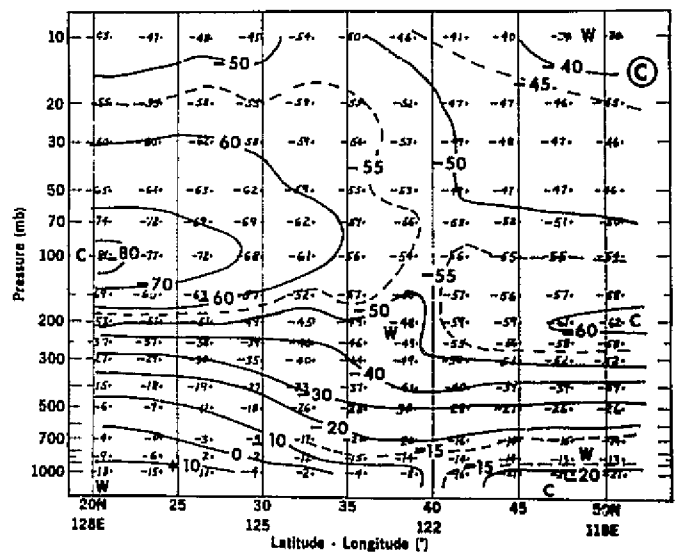

Figure 58--Same as Figure 55 for February 27, 1974.

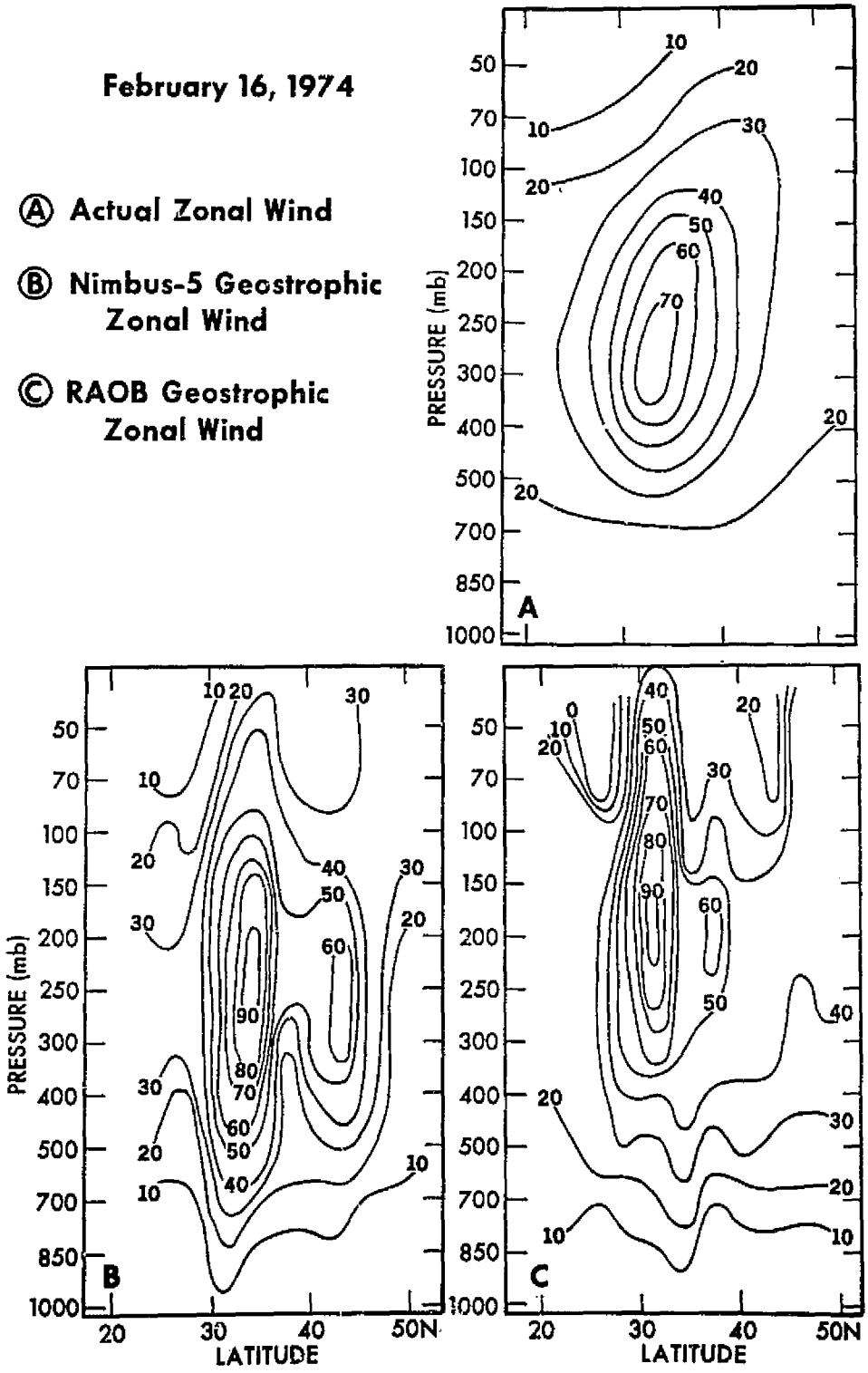

Figure 59--Geostrophic zonal winds calculated from the radiosonde and Nimbus-5 temperatures and the zonal component of the true wind for February 16, 1974.

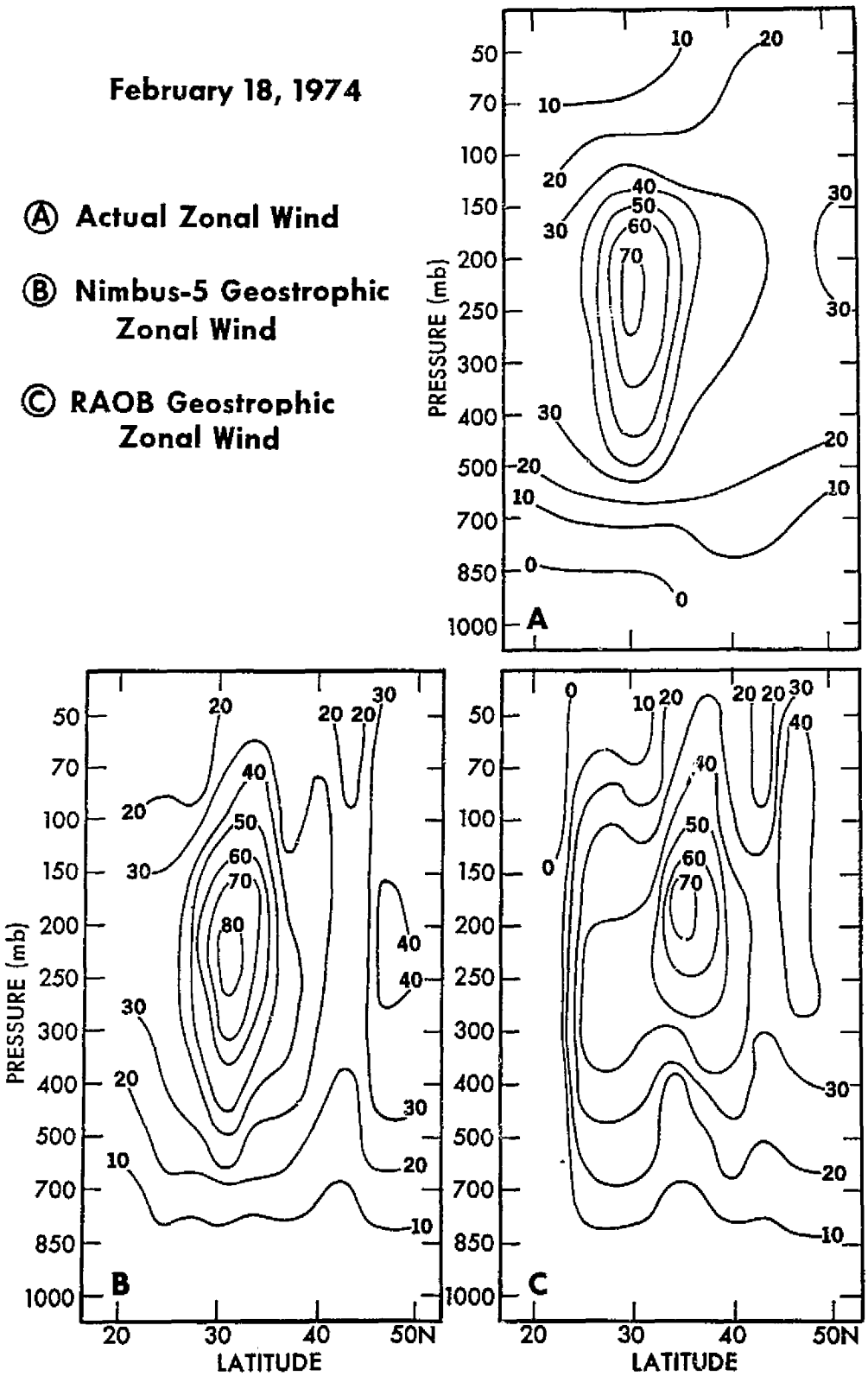

Figure 60--Same as Figure 59 for February 18, 1974.

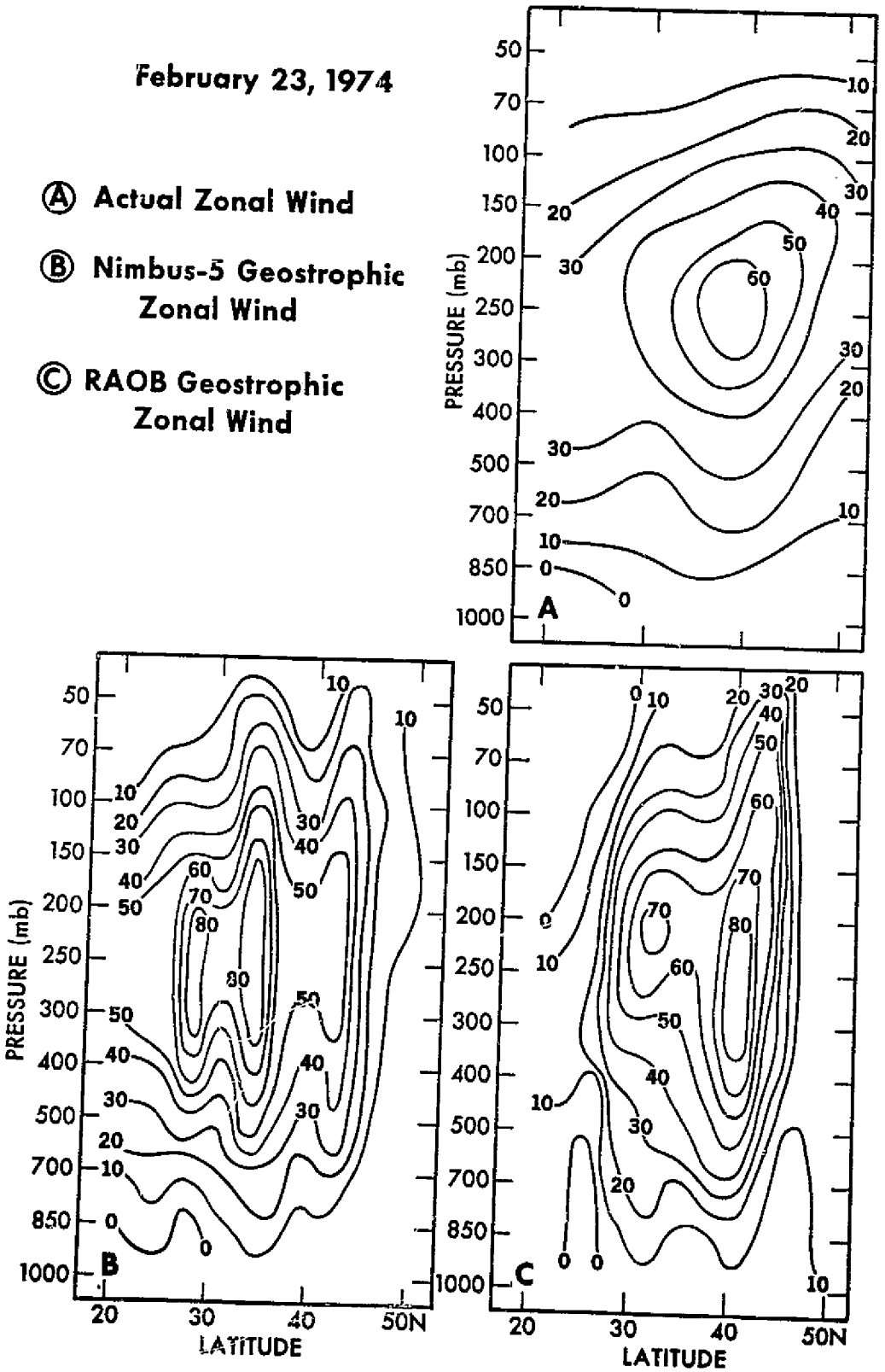

Figure 61--Same as Figure 59 for February 23, 1974.

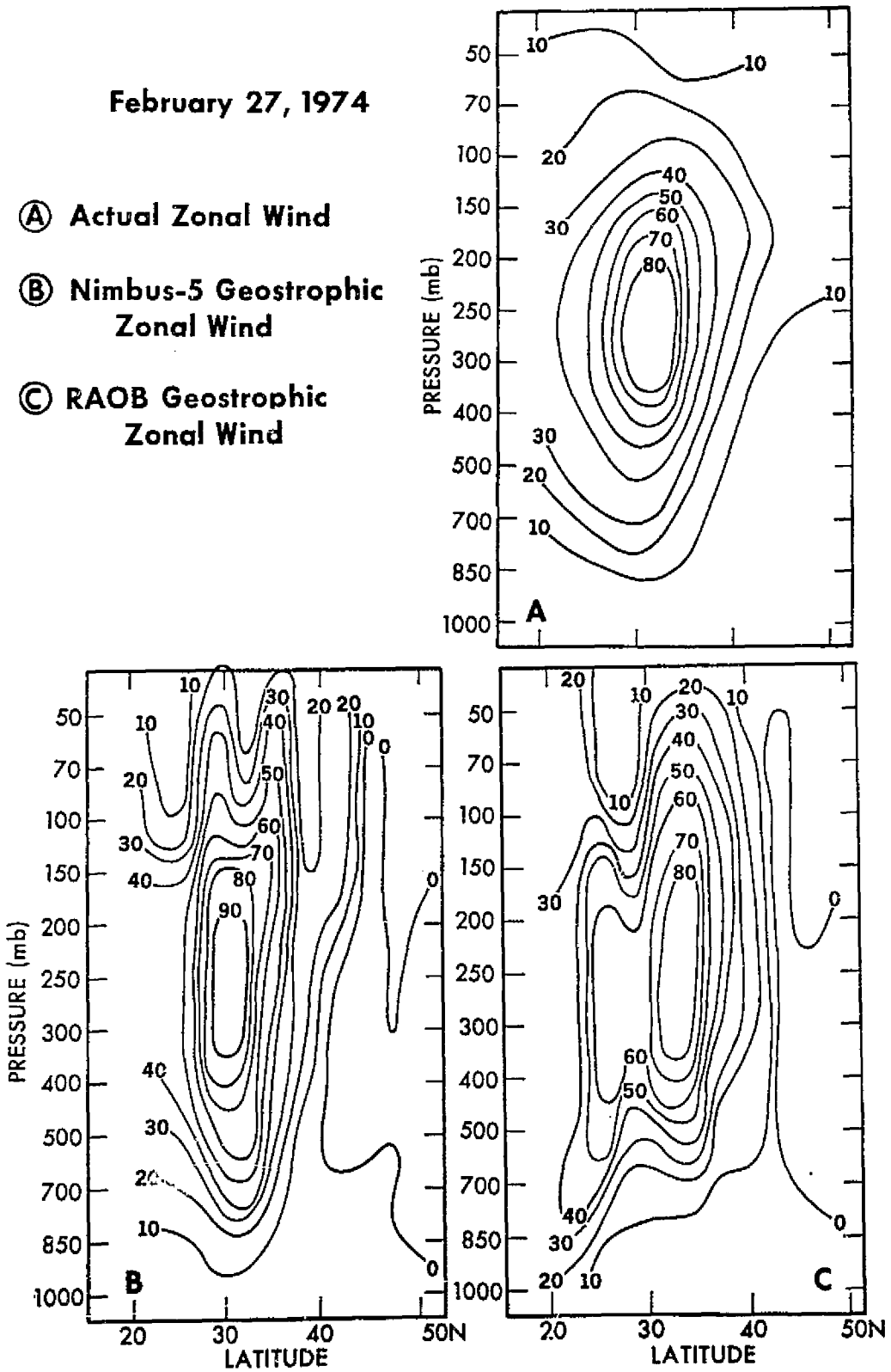

Figure 62--Same as Figure 59 for February 27, 1974.

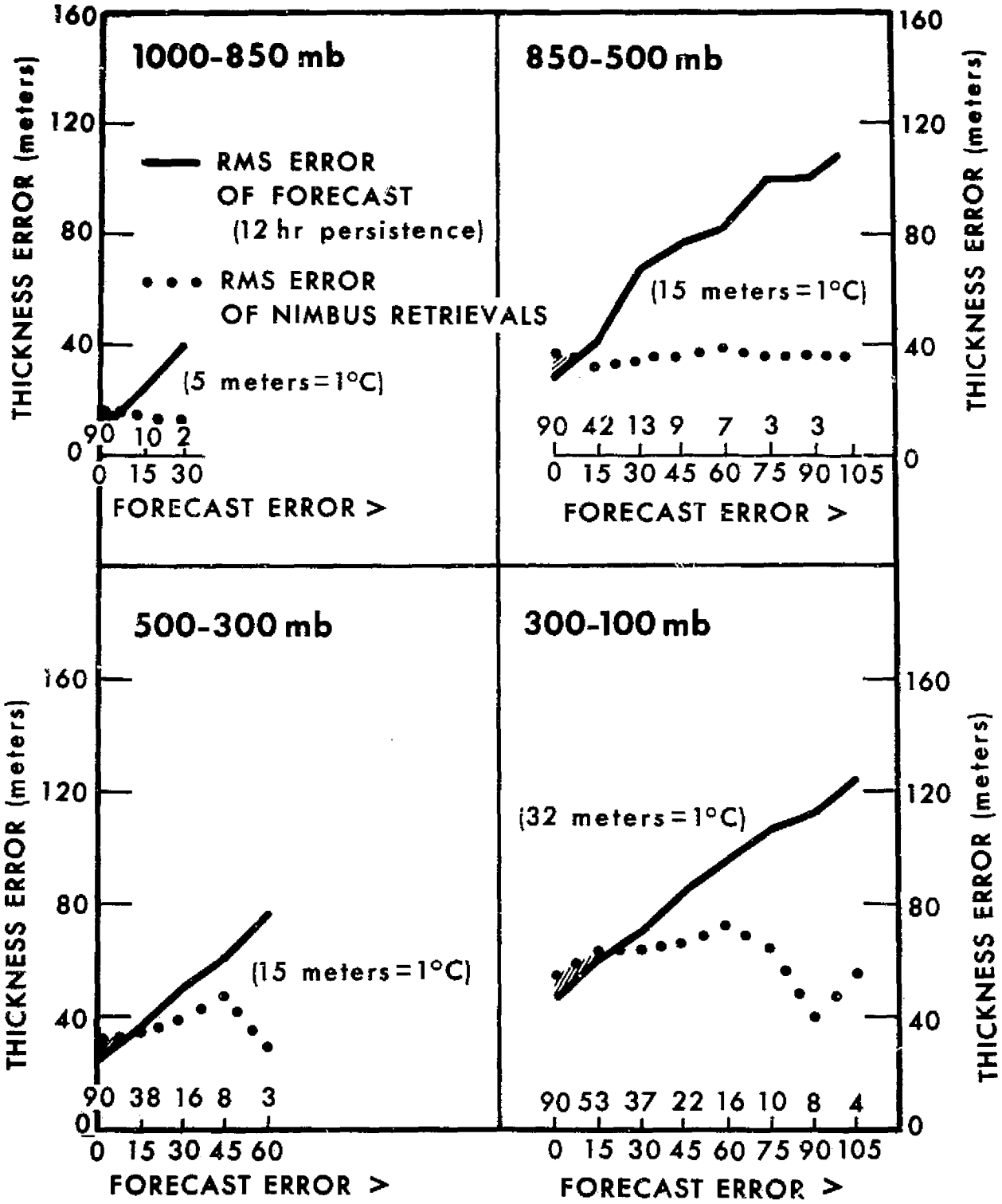

Figure 63--RMS error of the Nimbus-5 and forecast thickness values for various pressure layers as a function of sample sets stratified by the range of forecast errors.

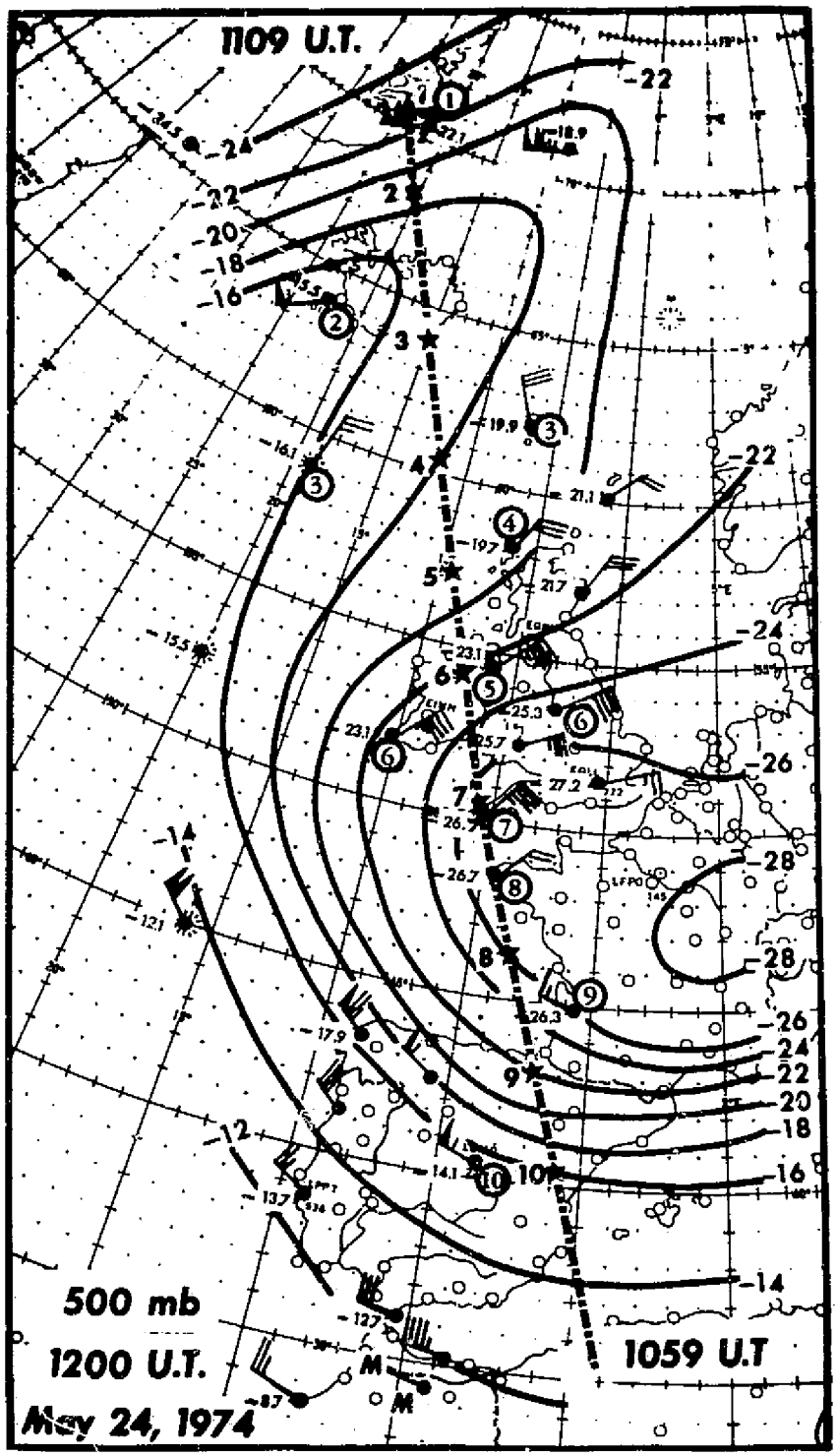

Figure 64--500-mb analysis of radiosonde temperatures data for 1200 UT 24 May 1974 in vicinity of Nimbus-5 overpass. Nimbus-5 temperature retrieval locations are indicated by stars with large numerals 1-10. Radiosondes used for cross section analysis are indicated with small numerals 1-10. The wind bar denote knots.

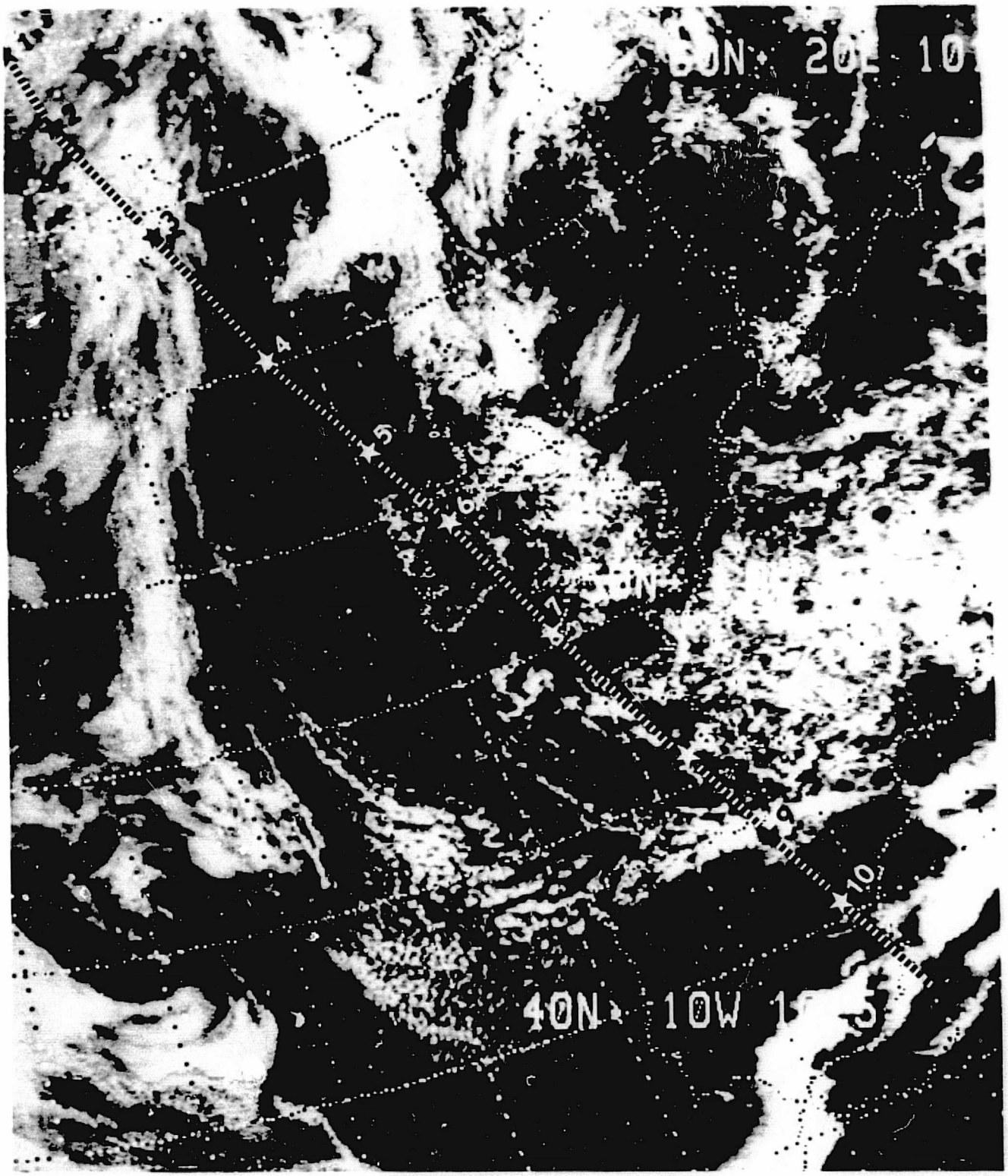

Figure 65--NOAA-3 SR visible image showing clouds in vicinity of Nimbus-5 overpass of 24 May 1974, 1017Z-1025Z. Nimbus-5 orbital track (dashed line). Location of Nimbus-5 temperatures shown by stars.

May 24, 1974
Temperature Cross-Sections (°C)

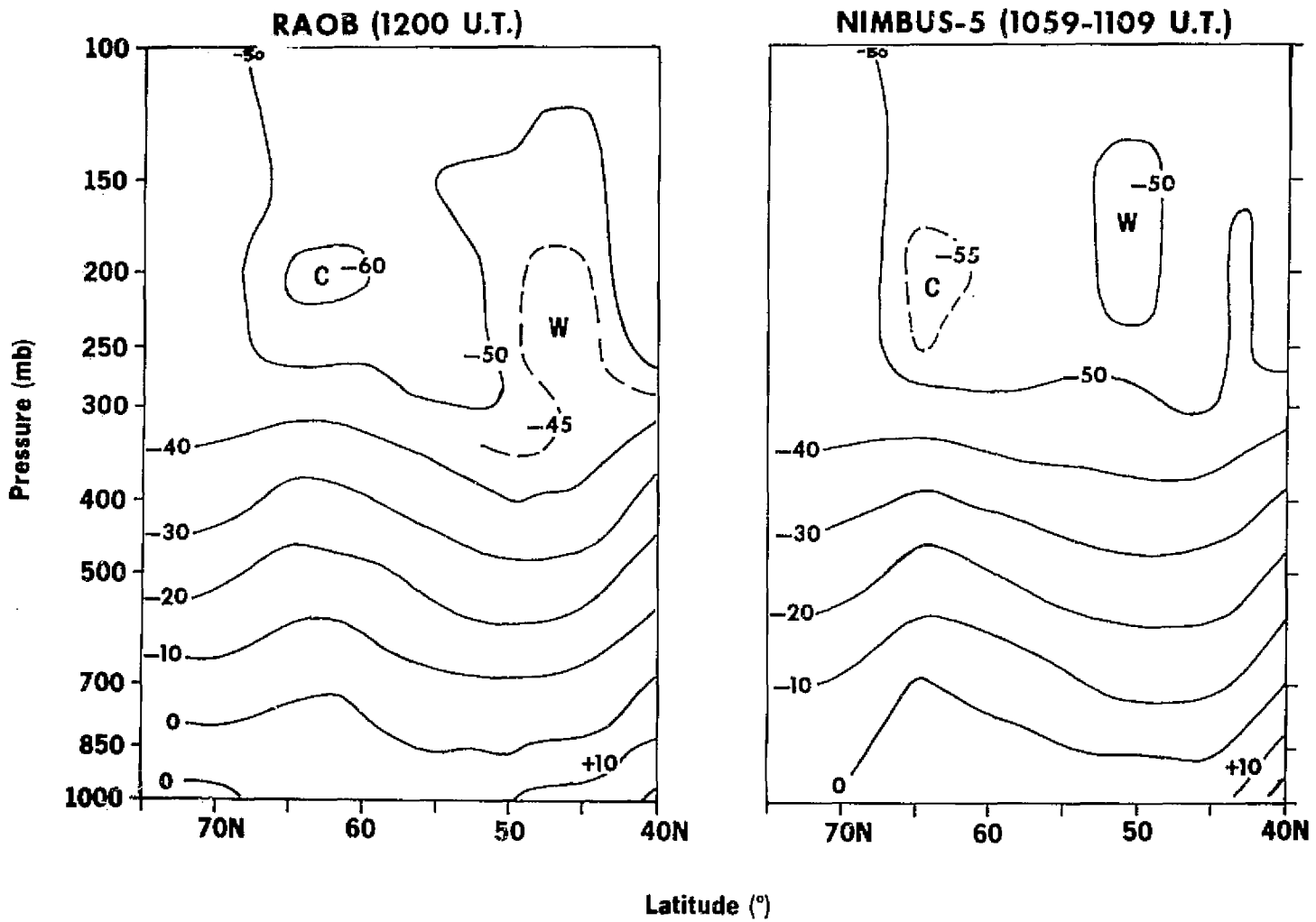

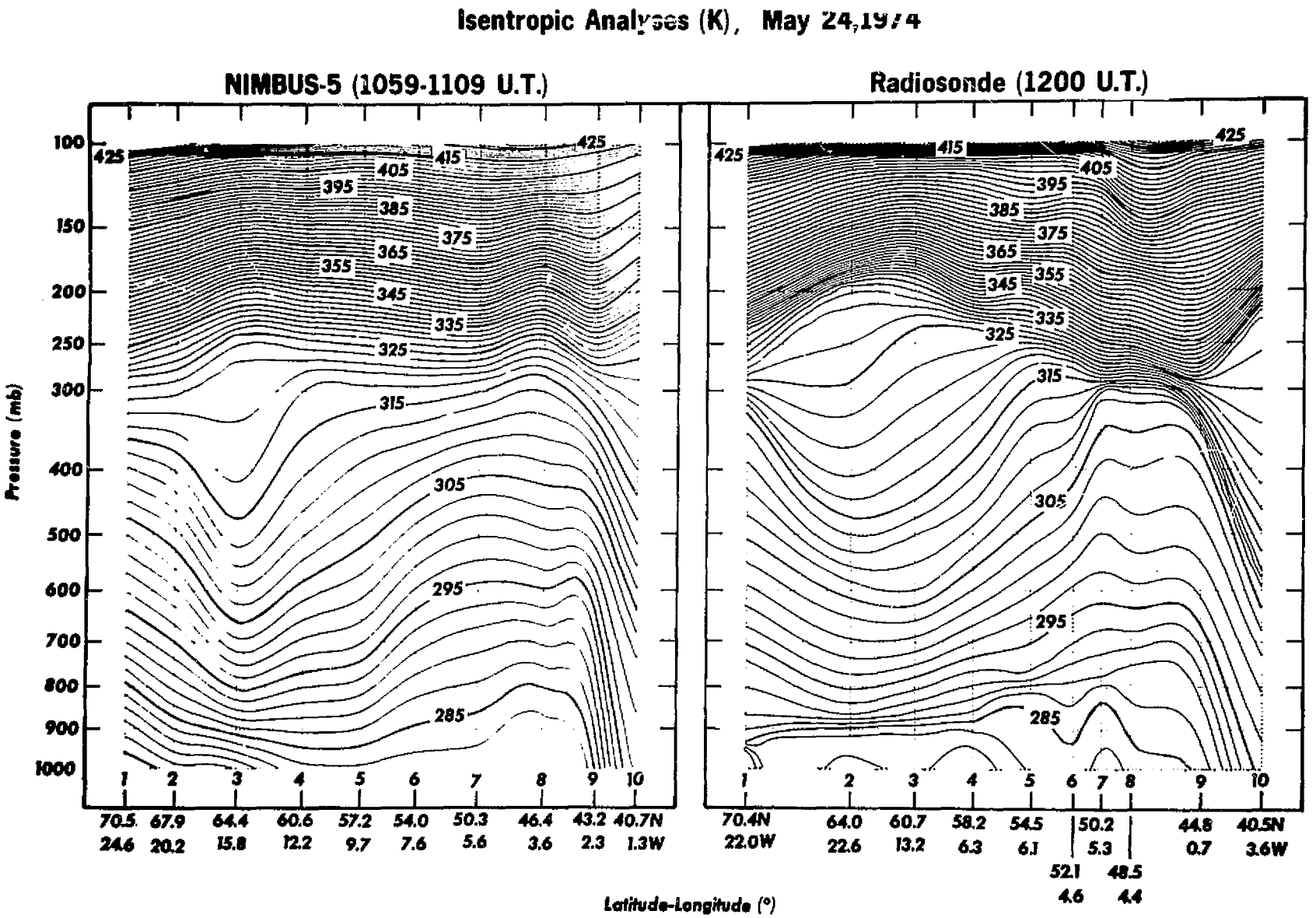

Figure 67--Isentropic cross section analyses prepared from radiosonde and Nimbus-5 temperature data at locations indicated by the numerals and stars, respectively.

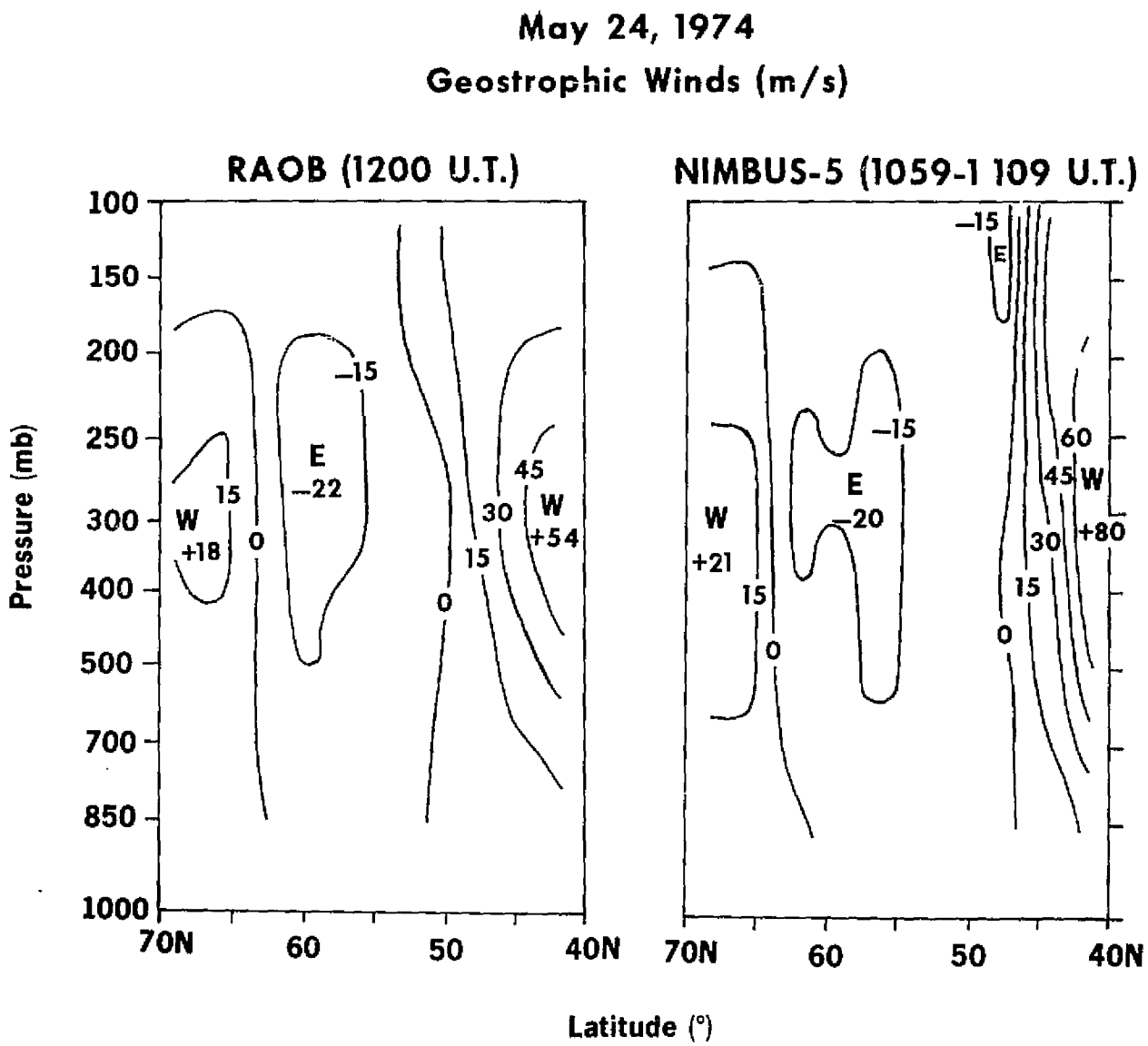

Figure 68--Analyses of geostrophic winds (m/s) calculated from the Nimbus and radiosonde temperature cross section data.

U.S. GOVERNMENT PRINTING OFFICE 1975—210-080

(Continued from inside front cover)

NESS 49 Operational Processing of Solar Proton Monitor Data. Louis Rubin, Henry L. Phillips, and Stanley R. Brown, August 1973, 17 pp. (COM-73-11647/AS)

NESS 50 An Examination of Tropical Cloud Clusters Using Simultaneously Observed Brightness and High Resolution Infrared Data From Satellites. Arnold Gruber, September 1973, 22 pp. (COM-73-11941/AS)

NESS 51 SKYLAB Earth Resources Experiment Package Experiments in Oceanography and Marine Science. A. L. Graham and John W. Sherman, III, September 1973, 72 pp. (COM 74-11740/AS)

NESS 52 Operational Products From ITOS Scanning Radiometer Data. Edward F. Conlan, October 1973, 57 pp. (COM-74-10040)

NESS 53 Catalog of Operational Satellite Products. Eugene R. Hoppe and Abraham L. Ruiz (Editors), March 1974, 91 pp. (COM-74-11339/AS)

NESS 54 A Method of Converting the SMS/GOES VHRR Frequency (1691 MHz) to the Existing APT/MEFAX Frequency (137 MHz). John J. Nagle, April 1974, 18 pp. (COM-74-11294/AS)

NESS 55 Publications and Final Reports on Contracts and Grants, 1973. NESS, April 1974, 8 pp. (COM-74-11102/AS)

NESS 56 What Are You Looking at When You Say This Area Is a Suspect Area for Severe Weather? Arthur H. Smith, Jr., February 1974, 15 pp. (COM-74-11333/AS)

NESS 57 Nimbus-5 Sounder Data Processing System, Part II: Measurement Characteristics and Data Reduction Procedures. W.L. Smith, H. M. Woolf, P. G. Abel, C. M. Hayden, M. Chalfant, and N. Grody, June 1974, 99 pp. (COM-74-11436/AS)

NESS 58 The Role of Satellites in Snow and Ice Measurements. Donald R. Wiesnet, August 1974, 17 pp. (COM-74-11747/AS)

NESS 59 Use of Geostationary-Satellite Cloud Vectors to Estimate Tropical Cyclone Intensity. Carl O. Erickson, September 1974, 57 pp. (COM-74-11762/AS)

NESS 60 The Operation of the NOAA Polar Satellite System. Joseph J. Fortuna and Larry H. Hombrick, November 1974, 127 pp. (COM-75-10390/AS)

NESS 61 Potential Value of Earth Satellite Measurements to Oceanographic Research in the Southern Ocean. E. Paul McClain, January 1975, 18 pp.

NESS 62 A Comparison of Infrared Imagery and Video Pictures in the Estimation of Daily Rainfall From Satellite Data. Walton A. Follansbee and Vincent J. Oliver, January 1975, 14 pp.

NESS 63 Snow Depth and Snow Extent Using VHRR Data From the NOAA-2 Satellite. David F. McGinnis, Jr., John A. Pritchard, and Donald R. Wiesnet, February 1975, 10 pp.

NESS 64 Central Processing and Analysis of Geostationary Satellite Data. Charles F. Bristor (Editor), in press, 1975.

NESS 65 Geographical Relations Between a Satellite and a Point Viewed Perpendicular to the Satellite Velocity Vector (Side Scan). Irwin S. Ruff and Arnold Gruber, March 1975. (COM-75-10678/AS)

NESS 66 A Summary of the Radiometric Technology Model of the Ocean Surface in the Microwave Region. John C. Alishouse, in press, 1975, 24 pp.

NESS 67 Data Collection System Geostationary Operational Environmental Satellite: Preliminary Report. Merle L. Nelson, March 1975. (COM-75-10679/AS)

NESS 68 Atlantic Tropical Cyclone Classifications for 1974. Donald C. Gaby, Donald R. Cochran, James B. Lushine, Samuel C. Pearce, Arthur C. Pike, and Kenneth O. Poteat, April 1975, 6 pp. (COM-75-1-676/AS)

NESS 69 Publications and Final Reports on Contracts and Grants, NESS--1974. April 1975, 7 pp.

NESS 70 Dependence of VTPR Transmittance Profiles and Observed Radiances on Spectral Line Shape Parameters. Charles Braun, July 1975, 17 pp.